

## General Disclaimer

### One or more of the Following Statements may affect this Document

- This document has been reproduced from the best copy furnished by the organizational source. It is being released in the interest of making available as much information as possible.
- This document may contain data, which exceeds the sheet parameters. It was furnished in this condition by the organizational source and is the best copy available.
- This document may contain tone-on-tone or color graphs, charts and/or pictures, which have been reproduced in black and white.
- This document is paginated as submitted by the original source.
- Portions of this document are not fully legible due to the historical nature of some of the material. However, it is the best reproduction available from the original submission.

~~NASA CR-156825~~

SPT

JANUARY 1978

# Geosynchronous Microwave Atmospheric Sounding Radiometer (MASR) Antenna Feasibility Study

## Final Report

Contract NAS 5-24087



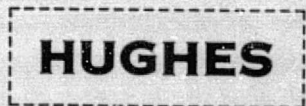
NASA Technical Officer  
L R Dod

(NASA-CR-156825) GEOSYNCHRONOUS MICROWAVE ATMOSPHERIC SOUNDING RADIOMETER (MASR) ANTENNA FEASIBILITY STUDY. VOLUME 3: ANTENNA FEASIBILITY Final Report (Hughes Aircraft Co.) 178 p HC A09/MF A01 CSCL 04A G3/46	N78-33646  Unclas 34191
---	----------------------------------

## Volume III Antenna Feasibility



ANTENNA DEPARTMENT  
RADAR SYSTEMS GROUP



HUGHES AIRCRAFT COMPANY  
CULVER CITY, CALIFORNIA

JANUARY 1978

**Geosynchronous Microwave  
Atmospheric Sounding  
Radiometer (MASR)  
Antenna Feasibility Study**

**Final Report**

Contract NAS 5-24087

NASA Technical Officer  
L R Dod

Hughes Program Manager  
A T Villeneuve

**Volume III  
Antenna Feasibility**

ANTENNA DEPARTMENT  
RADAR SYSTEMS GROUP

**HUGHES**

HUGHES AIRCRAFT COMPANY  
CULVER CITY, CALIFORNIA

Hughes Ref No. D9236 • P77-569  
DEPT. REF. NO. 2753/1265

## CONTENTS

1.0	INTRODUCTION	1
2.0	DISCUSSION	3
2.1	Antenna Requirements	3
2.2	Candidate Systems	6
2.2.1	Offset Reflector and Feed	6
2.2.2	Cassegrain Reflector and Feed	6
2.3	Comparison of Candidate Systems	10
2.3.1	Electrical Performance	10
2.3.2	Mechanical Design Studies	13
2.3.3	Summary of Initial Tradeoff Study	18
2.4	Electrical Design of Selected System	18
2.4.1	RF Design Studies	18
2.5	RF Testing	53
2.5.1	Available Techniques	54
2.5.2	Relative Merits of Techniques	58
2.6	Mechanical Design Studies	60
2.6.1	Preliminary Design Study	60
2.6.2	Baseline Design Study: Deployable Symmetrical Cassegrain Antenna System	82
2.7	MASR Gimbal Design	123
2.7.1	Gimbal Requirements	123
2.7.2	Mechanism Description	126
2.7.3	Component Selection	127
2.7.4	Gimbal Performance	134
2.8	Areas Requiring Further Study	135
3.0	SCHEDULE	139
4.0	SUMMARY AND CONCLUSIONS	141
	APPENDIX A. EFFECT OF BLOCKAGE AND SHADOWING	143
	APPENDIX B. MATERIAL SELECTION	151



## LIST OF ILLUSTRATIONS

Figure		Page
1	Reflector and Offset Focal-Point Feed . . . . .	8
2	Cassegrain Reflector System and Feed . . . . .	9
3	Geometry for Gaussian Feed Analysis . . . . .	19
4	Calculated E-Plane and H-Plane Patterns for 20 dB Taper, 0.198 Meter Diameter Subreflector . . . . .	25
5	Calculated E-Plane and H-Plane Patterns for 18 dB Taper, 0.25 Meter Diameter Subreflector . . . . .	26
6	Calculated E-Plane and H-Plane Patterns for 20 dB Taper, 0.25 Meter Diameter Subreflector . . . . .	27
7	Calculated E-Plane and H-Plane Patterns for 22 dB Taper, 0.25 Meter Diameter Subreflector . . . . .	28
8	Calculated E-Plane and H-Plane Patterns for 20 dB Taper, 0.25 Meter Diameter Subreflector . . . . .	29
9	Calculated E-Plane and H-Plane Patterns for 20 dB Taper, 0.25 Meter Diameter Subreflector . . . . .	30
10	Calculated E-Plane and H-Plane Patterns for 22 dB Taper, 0.25 Meter Diameter Subreflector . . . . .	31
11	Calculated E-Plane and H-Plane Patterns for 20 dB Taper, 0.25 Meter Diameter Subreflector . . . . .	32
12	Relationship of Subreflector and Earth Disc as seen from Feed Point . . . . .	36
13	Blockage and Shadowing Effects . . . . .	37
14	Model for Antenna Loss Temperature Calculation . . . . .	40
15	Effect of Surface Tolerance on Beam Efficiency. . . . .	48
16	Effects of Normal Surface Tolerance on Beam Efficiency. . . . .	49
17	Cassegrain Antenna Beam Pointing Error Analysis . . . . .	51

v  
 PRECEDING PAGE BLANK NOT FILMED

LIST OF ILLUSTRATIONS (Continued)

Figure		Page
18	Convair 8-Foot-Diameter Graphite Epoxy Cassegrainian Antenna on Pattern Range . . . . .	61
19	Test Program Successfully Completed on Convair 8-Foot-Diameter Graphite Antenna . . . . .	62
20	Twelve-Foot Diameter Graphite Cassegrain Antenna . . . . .	64
21	Twelve-Foot Diameter Graphite Cassegrain Antenna . . . . .	65
22	Shell Adjustor . . . . .	68
23	Large Aperture Antenna Thermal Design . . . . .	72
24	12-Foot Antenna/15-Inch Subreflector Temperature Predictions . . . . .	74
25	Structural Analysis of 12-Foot Antenna . . . . .	75
26	Concept No. 1 . . . . .	79
27	Concept No. 2 . . . . .	80
28	Concept No. 3 . . . . .	81
29	Concept No. 4 . . . . .	82
30	MASR Baseline Antenna System . . . . .	90
31	Stowed MASR Antenna . . . . .	91
32	Deploying MASR Antenna . . . . .	92
33	MASR Antenna Launch Supports . . . . .	93
34	Isometric View of MASR Antenna Dish . . . . .	103
35	Ribs, Rings, and Membrane Elements in Finite Element Model of Dish . . . . .	104
36	Mode 1 of MASR Antenna Dish . . . . .	105
37	Calculated Variation in Coefficient of Thermal Expansion as a Function of Fiber Content for Pseudoisotropic GY-70/X-30 (room temperature) . . . . .	106
38	Typical Rib and Ring Element Cross Section . . . . .	108
39	Reflector Surface Temperature versus Radius for a Sun-on-Side Condition . . . . .	109
40	Through the Depth Temperature Gradient versus Radius . . . . .	109
41	Assumed Temperature Distribution Over Antenna Structure . . . . .	110
42	Finite Element Model of Deployable Support Frame . . . . .	115

LIST OF ILLUSTRATIONS (Continued)

Figure		Page
43	Possible Bearing/Gimbal Model . . . . .	117
44	First Mode Shape of Deployable Support Frame $w_1 = 29.5$ Hz . . . . .	118
45	Launch Support Structure Finite Element Model . . . . .	119
46	PDMO for 4.4 M MASR Antenna . . . . .	122
47	Standard Frame . . . . .	125
48	Command Profiles for Line Indexing and Reversals . . . . .	126
49	Maser Gimbal Dimensions in Inches . . . . .	127
50	MASR Gimbal Detail . . . . .	131
51	MASR Estimated Schedule . . . . .	140

## LIST OF TABLES

Table		Page
I	Summary of Antenna Requirements . . . . .	7
II	Summary of Calculated Electrical Performance of Candidate Systems . . . . .	14
III	Evaluation of Mechanical Characteristics . . . . .	17
IV	Gaussian Beam Feed Characteristics . . . . .	22
V	Summary of Performance Characteristics of Cassegrain Antenna . . . . .	24
VI	Effect of Subreflector and Strut Blockage . . . . .	39
VII	Comparison of Reflection Coefficients of Layers and Uncoated Solid Aluminum . . . . .	44
VIII	Beam Deviation Factors . . . . .	52
IX	Allowable RMS Values of Various Displacements and Rotations in Cassegrain Antenna . . . . .	52
X	Far-Field Distances for 4.4 Meter Paraboloid . . . . .	55
XI	Summary of Measurement Techniques . . . . .	59
XII	Technology Antenna Mass Properties . . . . .	63
XIII	12-Foot Cassegrain Antenna Weight Summary . . . . .	66
XIV	Mass Property Comparison . . . . .	70
XV	Weight Summary . . . . .	71
XVI	Natural Frequencies and Mode Shapes . . . . .	111
XVII	Results of Surface RMS Analysis . . . . .	112
XVIII	Subreflector Displacements for Thermal Condition . . . . .	113
XIX	Natural Frequencies of the Deployable Support Frame . . . . .	119
XX	Basic Gimbal Requirements . . . . .	124
XXI	Components . . . . .	128
XXII	MASR - STORMSAT Gimbal Weight Estimate . . . . .	129
XXIII	MASR Gimbal Performance . . . . .	135

**PRECEDING PAGE BLANK NOT FILMED**

## ACKNOWLEDGEMENT

The following personnel were the main contributors to this study:

Hughes Aircraft Company:

A. T. Villeneuve (Program Manager)  
W. H. Kummer  
S. A. Milliken  
G. Z. Thomas  
W. V. T. Rusch (Consultant)

General Dynamics Convair Division:

G. C. Krumweide  
D. R. Laue  
E. T. Lipscomb  
D. H. Vaughn

**PRECEDING PAGE BLANK NOT FILMED**

## 1.0 INTRODUCTION

This report contains the results of a study of antenna systems capable of operating with a multichannel microwave radiometer for the 1984-85 time period. The radiometer is intended for mapping severe storm activity over patches on the surface of the earth 750 km square. Two main antenna system candidates were compared. These candidates were a paraboloidal reflector with an offset focal point feed, and a symmetrical Cassegrain reflector system. Both candidates appear to be acceptable from the point of view of beam efficiency, provided stringent mechanical tolerances can be met on feed position and reflector surface tolerances. However, from the point of view of maintaining the required positional accuracies and surface tolerances, as well from the point of view of manufacturability, cost effectiveness and technical risk, the symmetrical Cassegrain was selected as the preferred configuration. The main performance characteristics have been calculated, and a mechanical design study has been conducted to provide estimates of the technical risk, costs and development time required for the construction of such an antenna system. The antenna system consists of reflector, two-axis positioner, interface mounting for receiver and extendable truss for orbital deployment of the system.



PRECEDING PAGE BLANK NOT FILMED

## 2.0 DISCUSSION

### 2.1 ANTENNA REQUIREMENTS

MASR Frequency and Polarization - The MASR is a multi-channel microwave radiometer operating at the 118 GHz oxygen absorption line for temperature sounding and at the 183 GHz water line for water vapor sounding. Two atmospheric window channels at 104 and 140 GHz will also be observed by the MASR. The radiometer will receive double sideband energy about an absorption line. The 118 GHz line will have 8-10 channels spreading  $\pm 5$  GHz away from the line center. The 183 GHz line will have 6-8 channels spreading  $\pm 10-15$  GHz away from the line center. Each of these channels will receive a single linear polarization from the atmosphere and earth. All channels will operate simultaneously from the same resolution area using coincidental beams. Beamwidths of different channels need not be the same.

MASR Antenna Diameter - The MASR antenna will be a reflector antenna of aperture diameter 4.4 meters. The upper bound on the aperture diameter is determined by the requirement that the antenna be carried aboard the Space Shuttle cargo bay without folding or deployment. Spatial resolution requires the largest aperture obtainable but cost, mechanical, and thermal tolerances may dictate a smaller aperture than 4.4 meters. The antenna for MASR was designed in this study. Candidate systems included symmetrical reflectors of the Cassegrain type and offset parabolic reflectors.

MASR Antenna Pointing and Scanning - The MASR antenna must be capable of pointing at any location on the earth's surface as seen from the Stormsat synchronous orbit with an accuracy ( $1\sigma$ ) of three tenths of one antenna beamwidth. The antenna will be mechanically scanned about the observation point on earth to cover an area of  $(750 \text{ km})^2$  completely and contiguously in 30 minutes time. Calibration of the MASR requires that the antenna be pointed at cold space 10 degrees from the center of the earth's disc.

A method of scanning the MASR antenna is to use a raster scan pattern for the antenna beam. A line is scanned in the east-west (E-W) direction. At the end of the E-W line, the antenna beam is stepped by one beamwidth in the north-south (N-S) direction and the E-W line scan is repeated in the opposite direction. (Beamwidth is defined here as antenna half-power beamwidth.) A complete raster frame is scanned by this method with 1 minute allotted for one line of scan and 10 seconds allotted for beam stepping and turn-around at the end of a scanned line. The time for scanning a given frame is determined primarily by two factors. The integration time per resolution cell, or dwell time, shall be one second or longer. The shortest dwell time is determined by the highest measurement frequency for the MASR. Dwell time is defined as the time for the antenna to move one beamwidth during continuous motion scanning. Larger and smaller frames than  $(750 \text{ km})^2$  may be observed by MASR with dwell time and scanning parameters maintained constant. Line-to-line scan stability ( $1\sigma$ ) shall be one-tenth of the antenna beamwidth during a one-minute time period. The frame-to-frame stability ( $1\sigma$ ) shall be three-tenths of the antenna beamwidth.

MASR Calibration - The MASR requires two types of calibration. Primary calibration is achieved by pointing the antenna at cold space two degrees from the edge of the earth's disc. This primary calibration will be performed every 2-3 hours depending upon the stability of the radiometer system. The antenna near-in sidelobes and/or feed spillover lobes must not view earth during the primary cold-space calibration. The uncertainty in the cold-space calibration due to antenna sidelobes seeing earth and/or the Stormsat body shall be less than 1 percent.

Secondary calibration is required at the end of each scan line discussed in the preceding section. This secondary calibration is achieved by redirecting the antenna feed beam at two temperature extremes: (1) cold sky, and (2) a known ambient target. A possible method for achieving secondary calibration is a small rotating subreflector that redirects the feed beam at the two temperature references during the stepping/turn-around period at the end of line scanning. The linear dynamic range of the radiometer is a 0-350 degrees brightness temperature. Dicke switching will be achieved by a chopper wheel in front of the feed horn.

MASR RF Performance - The weighted beam efficiency,  $\eta^W_B$ , shall be greater than 85 percent including degradation due to surface roughness of the reflector, feed efficiency, thermal distortion, spillover losses and blockage (if applicable).

The noise power contribution from the antenna sidelobes viewing the spacecraft body should be small. Since the spacecraft temperature may be variable with time, the uncertainty in noise temperatures caused by the variable energy from the spacecraft should be less than 1 percent. High spatial resolution is inversely related to the main lobe beamwidth of the MASR antenna. It is desirable to optimize spatial resolution and weighted beam efficiency. A figure of merit, M, may be defined as

$$M = \eta^W_B \eta_A$$

where

$\eta^W_B$  = weighted beam efficiency

$\eta_A$  = aperture efficiency

The combined weighted beam efficiency and aperture efficiency must be optimized for  $\eta^W_B \geq 85$  percent. However, further improvement in  $\eta^W_B$  must be weighed against loss in spatial resolution.

MASR Mechanical Requirements - The moment of inertia of the two-axis scanning MASR antenna should be minimized. The torque requirements for scanning and control of the antenna are directly proportional to the moment of inertia of the antenna. The residual perturbation to the spacecraft attitude is also proportional to the antenna moment of inertia. Maximum allowable weight for the MASR antenna is 200 pounds.\* The radiometer electronics weight will be on the order of 50 pounds. Surface contour errors are contributed by: (1) fabrication tooling tolerances, (2) thermal distortion of the structure, and (3) misalignment of the feed/reflector structures. Surface roughness may be the limiting factor in determining the weighted beam efficiency and figure of merit for MASR. The reflector surface tolerance shall be less than 2 mils RMS under orbital operating conditions. The requirements are summarized in Table I.

## 2.2 CANDIDATE SYSTEMS

During the preliminary design portion of the study two candidate systems have been compared. These candidates are the paraboloidal reflector with offset focal-point feed, and the Cassegrain reflector and feed system. These two configurations are described next.

### 2.2.1 Offset Reflector and Feed

The geometry of the reflector with offset feed is shown in Figure 1.

### 2.2.2 Cassegrain Reflector and Feed

The geometry of the Cassegrain reflector system and feed considered for the preliminary design study is shown in Figure 2.

These configurations have been compared for both electrical performance characteristics and mechanical performance characteristics. These comparisons are summarized in the following sections. The details are presented in the Interim Feasibility Study Report (No. P77-327).

---

\*This requirement may be relaxed if necessary to obtain the desired performance.

PRECEDING PAGE BLANK NOT FILLED

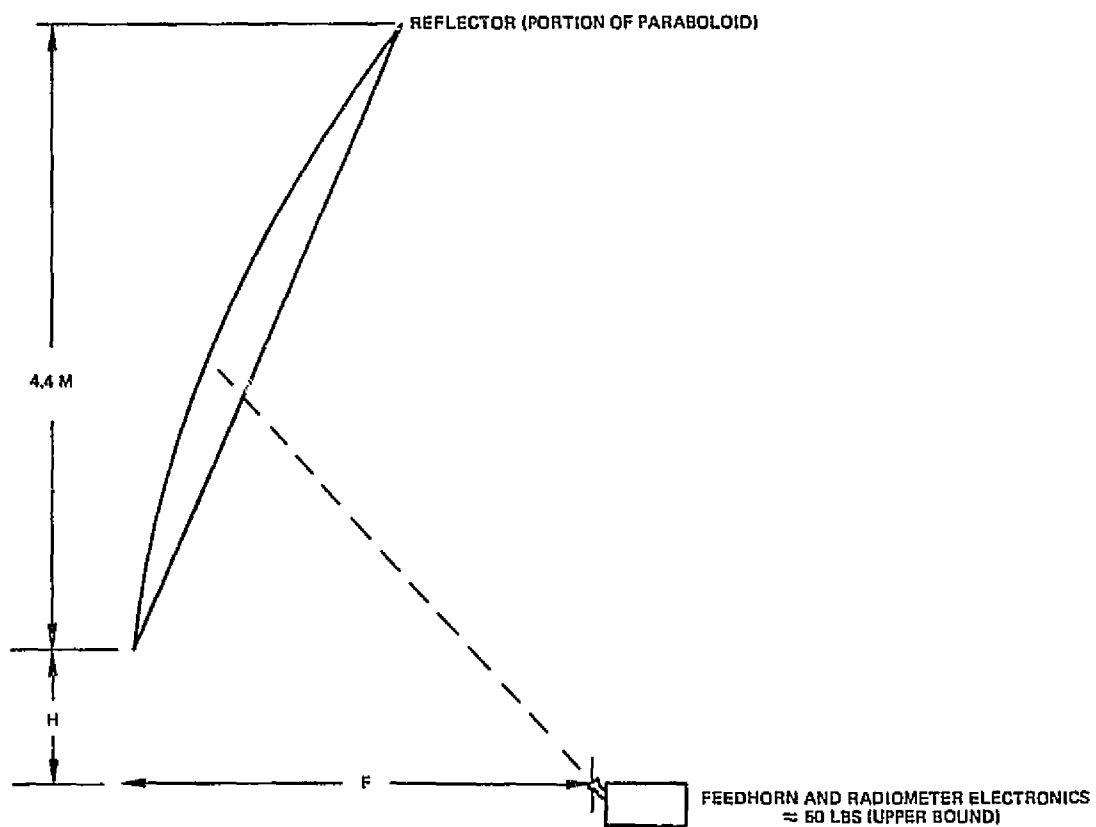


Figure 1. Reflector and offset focal-point feed.

ORIGINAL PAGE IS  
OF POOR QUALITY

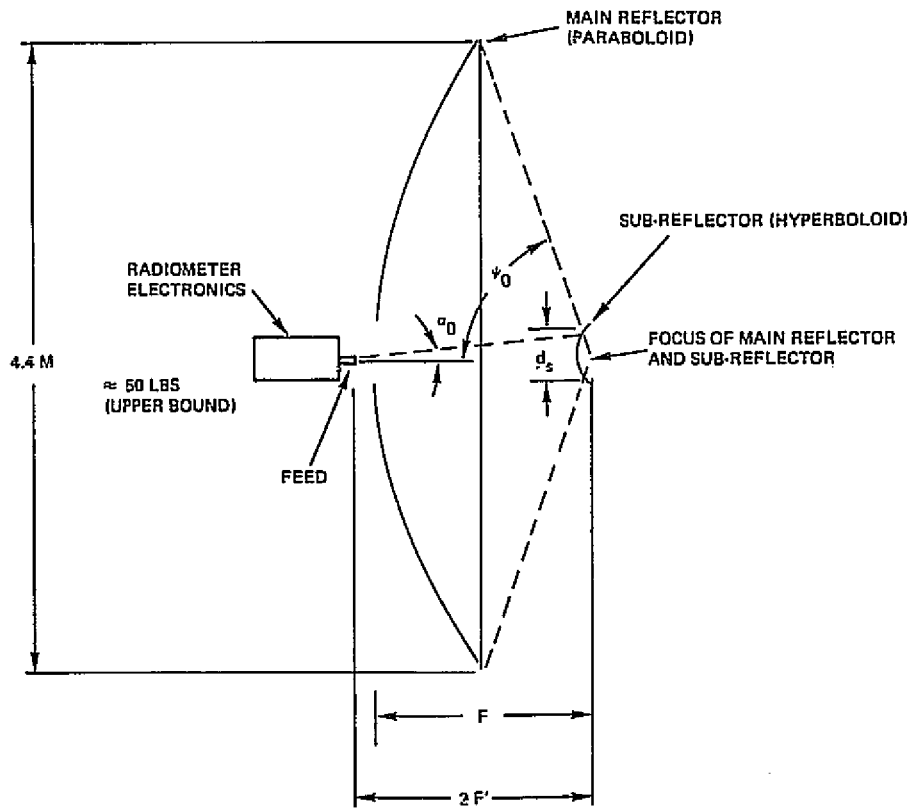


Figure 2. Cassegrain reflector system and feed.



## 2.3 COMPARISON OF CANDIDATE SYSTEMS

### 2.3.1 Electrical Performance

#### Offset Paraboloidal Configuration

Calculations of electrical performance were performed on the configuration of Figure 1 for a focal length of 3.32 meters and a bottom offset of 0.627 meter. A single corrugated conical horn was used for a feed.

Ideally, the feed horn should be positioned so that its phase center is at the reflector focus. However, it does not have a precise phase center, and in fact, E-plane patterns may have somewhat different phase centers than H-plane patterns. Thus, only an approximate phase center can be determined, and its position varies as a function of frequency. When the horn is used at several frequencies, as was initially anticipated in this study, it must thus be positioned at some compromise location. A selection technique used was location of the horn at a weighted mean between the approximate phase centers of the highest and lowest frequency. This position was selected so that the electrical shift from the correct phase center was equal at those two frequencies. The position of the horn is established by specification of the location of the point in the center of the horn aperture.

#### Secondary Patterns

Radiation patterns of the reflector feed combination were computed for vertical polarization at the frequencies of interest. The patterns were computed with a vector physical optics program. The effect of positioning the feed horns at some point other than the phase center was evident in null filling and skewing of the skirts of the beams, but the major portions of the main beams were preserved down to nearly the -20 dB level. Nearly all remaining sidelobes were more than 30 dB below the peak. The cross-polarization level was negligible in the elevation cuts. In the azimuth

cuts it rose to a peak value slightly off the beam axis, but still within the main beam. All cross-polarized principal maxima were greater than about 24 dB below the peak of the main beam and appeared to fall off rapidly beyond the maximum.

### Beam Efficiency

Beam efficiency,  $\eta_B$ , is a fraction of total power supplied by the horn that is contained within the main beam and has the correct polarization. The gain,  $G_d$ , is defined relative to the total power radiated by the feed horn and thus includes the effects of cross polarization and spillover. Losses due to dissipation, fabrication tolerances, and other errors in the feed horn are not included.

Calculations of the conventional beam efficiency were performed for the offset paraboloid with the corrugated conical feed horn by integrating the power in the main beam and comparing this power to the power radiated by the feed horn. The resulting estimates, not accounting for effects of tolerances, are 90 percent at 114.66 GHz and 92 percent at 193.3 GHz.

In a real antenna use of rigid supporting struts might be necessary if the proper position between the feed and the reflector is to be maintained. These struts will introduce some blockage and scattering within the aperture that will affect the peak gain slightly and will also have some effect on side-lobe levels, and, consequently, on beam efficiency. Because the wavelengths are very small compared with the sizes of the structures, the effects can be predicted primarily by optical methods.

Subsequent to the electrical performance analysis of the offset paraboloidal reflector, it became apparent that quasi-optical feeding techniques may be desirable to minimize feeding losses. Such techniques would use separate feeds at each frequency so that broadband feed horns would no longer be required. In that case some improvement could be expected in performance of the offset paraboloidal configuration, since the feeds could be designed to operate over narrower bandwidths. However, due to the results obtained in the mechanical studies, the calculations were not performed for the narrowband horn configuration.

### Cassegrain Configuration

Electrical performance calculations were performed for the Cassegrain antenna using subreflector diameters of 19.8 cm and 37.0 centimeters. The calculations were done for a value of  $2F' = 1.70$  meters and  $F = 1.54$  meters. (See Figure 2.) The taper over the subreflector was varied by adjusting the beamwidth of the idealized feed pattern of the form:

$$|E| = \cos^2(\beta\theta) \quad \theta < \frac{\pi}{2\beta}$$

$$|E| = 0 \quad \theta > \frac{\pi}{2\beta}$$

The taper is adjusted by adjusting  $\beta$ .

The computer program can be used to calculate patterns, gain, efficiency, and beam efficiency. It is arranged to allow the use of an oversize subreflector (one that extends beyond the geometric optics line of sight from the focal point of the main reflector to its edge). Scattering effects usually result in such an oversize subreflector being optimum in the sense of achieving maximum gain from a Cassegrain. Such an oversized subreflector was also required to reduce forward spillover while maintaining high beam efficiency.

It should be emphasized here that use of the term oversized does not necessarily mean that the subreflector will be large in comparison to the main reflector. A particular geometric optics solution to the feed and subreflector problem may call for a very small subreflector and a correspondingly large feed. In this case a subreflector that extends beyond the line-of-sight as mentioned above (oversized), would still be quite small in relation to the main reflector.

The initial computations used a subreflector that was in the neighborhood of 0.4 m in diameter. This subreflector was larger than called for in an optimum design for gain efficiency, and deliberately so, in an effort to keep the feed assembly from becoming too large. However, gain and beam

efficiency calculations with this size subreflector showed that it was too large to allow meeting the performance requirement of at least 85 percent beam efficiency on a real antenna (i. e., taking into account surface tolerances, etc.). Hence, a design was worked out using a diameter of about 0.2 m for the subreflector. For this case the beam efficiency improved considerably over the other cases to 97.7 percent, with an antenna efficiency of 70.4 percent. These calculations neglected dissipation and strut blockage, forward spillover and subreflector scattering effects.

The various electrical characteristics of the two configurations are summarized in Table II.

### 2.3.2 Mechanical Design Studies

#### Geometrical Considerations

The Cassegrain system will have the stiffest shell or skin for a given shell thickness because the main reflector in the Cassegrain system has greater curvature than the offset reflector. Consequently, it may be possible to construct the Cassegrain main reflector from larger panel bays.

For a given aperture diameter the symmetrical Cassegrain configuration will be lighter than the offset paraboloidal configuration because the actual length of the major axis of the offset reflector is approximately 8 percent greater than that of the Cassegrain configuration, thereby requiring fewer structural members in the backup structure and possibly resulting in higher natural frequencies of the reflector.

#### Dynamic Balance and Characteristics

In order to estimate the center of gravity of the various antenna systems, to determine suitable locations for gimbal joints, and to determine hardware required to support antenna components, two viable candidate configurations were sketched for each antenna type. It was found that the center of gravity (C.G.) for the Cassegrain system is behind the main reflector, whereas the offset paraboloidal reflector system has its C.G.

TABLE II. SUMMARY OF CALCULATED ELECTRICAL PERFORMANCE OF CANDIDATE SYSTEMS

Antenna Type	Freq. GHz	Aperture Diam. Met	Subrefl. Diam. cm.	Peak Sidelobe dB**	Gain dB	Effic. %	Beam Efficiency %	3 dB Beamwidth Deg.	2.5 Times 3 dB Beamwidth Deg.	Value Used in Beam Efficiency Calc. Deg.	Aperture Taper dB
Offset* Ref.	114.66	4.40	--	25.8 az. 20.0 el.	72.87	69.3	90.1	0.0423 az. 0.0419 el.	0.108 0.105	0.106 0.106	18
	193.3	4.40	--	25.2 az. 21.0 el.	77.20	66.1	92.4	0.0270 az. 0.0252 el.	0.0675 0.0641	0.0664 0.0664	18
Cassegrain†	a 104	4.40	37.0	27.1	71.2	57.3	92.9	0.0526	0.132	0.132	38
	b 104	4.40	37.0	26.4	71.52	61.7	93.0	0.0509	0.127	0.127	34
	c 104	4.40	37.0	25.6	71.76	65.2	92.8	0.0495	0.124	0.124	31
	d 104	4.40	19.8	29.1	72.1	70.4	97.7	0.0487	0.122	0.122	26

\*For the offset reflector a single corrugated horn feed was used over the whole band from 114 to 193.3 GHz.

\*\*For the offset reflector using a single feed, the first sidelobes are not well defined. They appear as shoulders on the main beam.

†An idealized horn feed pattern was used in the Cassegrain configuration.

- a Subreflector subtends half-angle of  $6.5^\circ$  at feed. Illumination down 10 dB at  $4.75^\circ$ .
- b Subreflector subtends half-angle of  $6.5^\circ$  at feed. Illumination down 10 dB at  $5.00^\circ$ .
- c Subreflector subtends half-angle of  $6.5^\circ$  at feed. Illumination down 10 dB at  $5.25^\circ$ .
- d Subreflector subtends half-angle of  $3.4^\circ$  at feed. Illumination down 10 dB at  $2.60^\circ$ .

in front of the reflector. An important implication here is that the structure necessary to support the reflector can be more directly attached to the spacecraft. An increased natural frequency at a reduced weight is also a possibility.

With the location of feed and radiometer behind the dish for the symmetrical Cassegrain design, and the fact that an attaching structure is essentially provided for mounting these components, the support structure for the feed and radiometer for the offset paraboloid provides a major weight penalty.

With respect to possible gimbal points, initial consideration was given to one approach where the backup is integrated with the reflector support structure and all gimbaling is then accomplished at the base of the system. A second approach in which the reflector and feed are supported by a carriage and gimballed at two widely separated locations was also considered.

Surface Contour - It is quite evident that because of the larger diameter and nonsymmetric design of an offset configuration, it would be considerably more difficult to achieve the overall 2 mil surface tolerance requirement with that configuration. It also appears that because the feed support for the offset has to be designed to withstand relatively high loads in contrast to the supports for the secondary reflector on the Cassegrain configuration, that thermal distortion effects may be difficult to design out of the offset paraboloid configuration without large weight penalties. Meeting the 2 mil requirement for positioning the feed transverse to the optical axis would be more difficult in the offset design because of structural considerations in the support of the feed system.

Structural Characteristics - Structural considerations would suggest that the Cassegrain configuration is the best choice because of its lighter weight, lower inertia, and high natural frequency, but of a more subtle nature is the simplicity of the design that allows for a more predictable analysis of the final structure.



Cost and Technical Risk - Relative to cost and technical risk for the offset configuration, the larger diameter and its asymmetry make it the more costly. Design and analysis cost would be greater because of the complexity of joints (e.g., all different, angularity of loads, etc.). The need for a homogeneous structure to satisfy thermal distortion requirements would unnecessarily complicate the analysis. Tools to fabricate a symmetrical Cassegrain would be fewer because of the many duplicated parts. The basic production mold for the offset configuration (PDMO) could not be made in one piece because of existing machine bed limitations. Therefore, a more expensive, multiple piece tool is expected to be necessary for the offset paraboloid configuration.

The symmetrical Cassegrain will require fewer parts and somewhat simpler parts because of its compactness. Most parts are expected to be identical and lend themselves to rate tools.

The repetition of joints and fewer pieces will make the assembly cost of the symmetrical Cassegrain less than that of the offset paraboloid.

It is not readily apparent, but adjustment of contour to meet the 2 mil requirement will be extremely difficult for the offset configuration because of the behavior of a nonsymmetrical shell when stressed.

The design risk is reduced for the Cassegrain configuration because of the experience gained on an 8-foot technology antenna produced by GD/C four years ago. In most respects the 4.4 meter reflector is just a simple scale up of the 2.44 meter design developed by Convair. In contrast, the 0.8 meter Nimbus-G offset reflector offers very little to reduce the technical risks associated with the 4.4 meter offset reflector.

Structural and Mechanical Tradeoff Study Summary - Provided in Table III is a summary of this evaluation of the various tradeoff parameters between the symmetrical Cassegrain and the offset paraboloid relative to the structural and mechanical consideration.

TABLE III. EVALUATION OF MECHANICAL CHARACTERISTICS

Parameter	Best Choice	Reason
Weight	Sym. Cassegrain	<ul style="list-style-type: none"> <li>a) Lighter Reflector for a given Aperture Diameter</li> <li>b) Lighter Support Structure with C.G. Behind Reflector.</li> <li>c) Lighter Feed Support.</li> </ul>
Dynamic Char.	Sym. Cassegrain	<ul style="list-style-type: none"> <li>a) Higher Natural Frequency with a Deeper Shell.</li> <li>b) Higher Natural Frequency with Lighter System.</li> </ul>
Surface Tolerance	Sym. Cassegrain	<ul style="list-style-type: none"> <li>a) Easier Achievement of Surface Accuracy with Smaller Diameter and Symmetrical Design.</li> </ul>
Structural Char.	Sym. Cassegrain	<ul style="list-style-type: none"> <li>a) Simpler and More Predictable by Analysis.</li> </ul>
Thermal Distortion	Sym. Cassegrain	<ul style="list-style-type: none"> <li>a) Reduced Distortion with Smaller Diameter and Symmetrical Design.</li> <li>b) Reduced Distortion with Closer and Symmetrically Supported Feed.</li> </ul>
Technical Risk	Sym. Cassegrain	<ul style="list-style-type: none"> <li>a) Less Risk with Experience Gained from 8-Foot Technology Program.</li> </ul>
Cost	Sym. Cassegrain	<ul style="list-style-type: none"> <li>a) Least Cost to Design and Analyze with Symmetrical and Compact Structure.</li> <li>b) Least Cost for Tooling with Fewer Parts and Symmetrical Structure. Also a Smaller PDMO Required.*</li> <li>c) Least Cost for Fabrication with Fewer Parts and Symmetrical Structure. Also, Most parts Identical.</li> <li>d) Least Cost for Contour Measurement with Symmetrical Structure.</li> </ul>

\*No facilities presently have been found that could manufacture the required single piece PDMO for the offset paraboloid.

### 2.3.3 Summary of Initial Tradeoff Study

The initial rf performance calculations indicate that with careful design both candidate configurations could probably be acceptable even though the comparisons were made under somewhat different conditions for each candidate system. However, the mechanical studies showed that at the present time it is doubtful if the required tolerance could be met in the offset configuration, so that no additional comparison of electrical characteristics was deemed necessary. The Cassegrain configuration was selected as the preferred configuration and further design studies were conducted.

## 2.4 ELECTRICAL DESIGN OF SELECTED SYSTEM

Subsequent to the selection of the Cassegrain configuration, additional electrical design studies were performed to provide information to be used in assessing anticipated performance, technical risk, costs, and development time required for the construction of such an antenna. These design studies are discussed in this section.

### 2.4.1 RF Design Studies

The rf design studies were conducted using a Gaussian beam feed model since it lends itself to quasi-optical multiplexing techniques that provide low loss channel separation. The configuration is illustrated in Figure 3. The effective position of the feed, as seen by the subreflector is  $z_h$ . The radiation from the feed must therefore appear to have its center of curvature located at  $z_h$  when viewed from the subreflector and must provide a desired taper over the aperture. The relation of these requirements to the Gaussian beam characteristics is considered next.

#### 2.4.1.1 Gaussian Beam Feed System

The radiometer electronics package incorporates within it a quasi-optical feed system that produces a feed pattern approximating a Gaussian beam. In this section the Gaussian beam feed characteristics are discussed and the beam parameters are related to the antenna parameters.

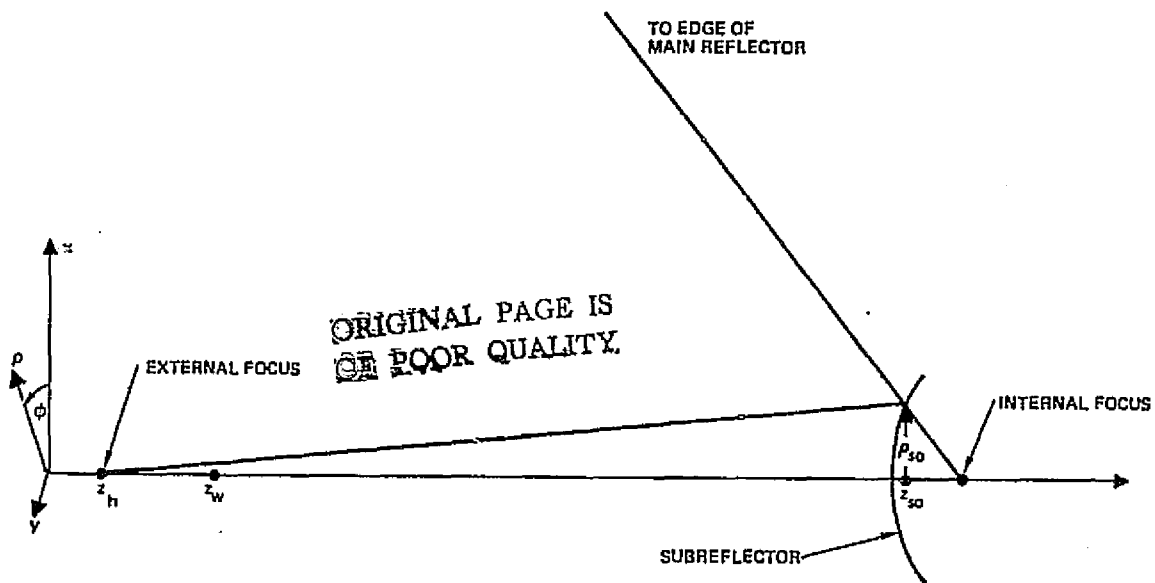


Figure 3. Geometry for Gaussian feed analysis.

The subreflector and its foci are shown in Figure 3. The Gaussian beam parameters must be adjusted to make  $z_h$  the center of curvature of the wave front at the subreflector, and to make the taper a specified value at the optical edge of the subreflector. The optical edge is here defined as lying on the line of sight from the focus of the main reflector to its edge. The actual subreflector extends beyond the optical edge to control diffraction and forward spillover.

The Gaussian beam may be described in terms of  $R(z)$ , the radius of curvature of the wavefront, and  $w(z)$ , the distance from the beam axis to the point where its amplitude decreases to  $1/e$  of its value on the axis. The variable  $z$  represents distance along the beam axis. The minimum value of  $w$ , denoted by  $w_0$ , is called the beam waist and occurs where the radius of curvature is infinite; that is, there the beam is a plane wave. On referring

to Figure 3, it may be seen that to make the wave appear to emanate from  $z_h$ , the external focus of the hyperboloid, it is appropriate to set the radius of curvature  $R(z_{so})$  equal to the distance from  $z_h$  to  $z_{so}$ . Thus  $R(z_{so})$  is given by the following expression:

$$R(z_{so}) = z_{so} - z_h \quad (1)$$

Also, the value of  $w(z_{so})$  may be selected to give a specified taper,  $B$ , in dB at the optical edge of the subreflector. In terms of this taper and of  $d_{so}$ , the diameter of the subreflector at its optical edge,  $w(z_{so})$  may be written as follows:

$$w(z_{so}) = 1.473 \frac{d_{so}}{\sqrt{B}} \quad (2)$$

This same taper will be approximately obtained over the main reflector. From these dimensions the beam waist is given by the following expression:

$$w_o^2 = w(z_{so})^2 / \left[ 1 + \left( \frac{\pi w(z_{so})^2}{\lambda R(z_{so})} \right)^2 \right] \quad (3)$$

The position of the beam waist is given as follows:

$$z_w = z_{so} - R(z_{so}) / \left[ 1 + \left( \frac{\lambda R(z_{so})}{\pi w(z_{so})^2} \right)^2 \right] \quad (4)$$

At arbitrary points along the beam axis  $w(z)$  and  $R(z)$  may then be written as follows:

$$w(z)^2 = w_o^2 \left[ 1 + \left( \frac{\lambda (z - z_w)}{\pi w_o^2} \right)^2 \right] \quad (5)$$

#### 2.4.1.2 Performance Calculations

Pattern and beam efficiency calculations were performed for the Cassegrain reflector with the Gaussian beam feed. The diameter of the main reflector was held constant at 4.40 meters, with an F/D ratio of 0.35. Two subreflector diameters were used and three different Gaussian aperture tapers were used. A subreflector diameter of 19.8 centimeters put the physical edge of the subreflector on the line-of-sight from the focus to the edge of the main reflector. This dimension permitted a fairly significant amount of forward spillover (1 percent) and also could result in diffraction effects at the edge of the subreflector that could degrade the illumination of the main reflector. Extending the subreflector diameter to 25 centimeters resulted in a reduction of forward spillover and reduced the illuminating function at the edge of the subreflector by an additional 11.9 dB, thereby reducing diffraction effects at that edge. The increased diameter also increases aperture blockage slightly, on the order of 0.6 percent. The results of the computation are summarized in Table V. The corresponding patterns are shown in Figures 4 through 11. The calculations include the effect of subreflector blockage, forward spillover (assuming the ideal Gaussian beam feed) and diffraction effects caused by the subreflector. Blockage by the subreflector support struts is not included. Strut blockage effects are included in Section 2.4.1.4. Calculations at 104 GHz indicate that increasing the subreflector size results in increased antenna efficiency although the beam efficiency decreased 1.5 percent. It is also evident that increasing the illumination taper increases beam efficiency at the expense of overall efficiency. An illumination taper of 20 dB has been used as a reasonable compromise value for the baseline design. The effects of tolerances are considered separately in Section 2.4.1.6.



TABLE V. SUMMARY OF PERFORMANCE  
CHARACTERISTICS OF CASSEGRAIN  
ANTENNA

(Strut blockage effects and tolerance effects not included)

Freq. GHz	D <sub>main</sub> Met.	D <sub>sub</sub> Met.	Subrefl. Taper dB*	Gain dB	1st Side Lobe dB	2nd Side Lobe dB	3rd Side Lobe dB	3dB BW Deg.	Ant. Eff. $\eta_A$	Beam Eff. $\eta_B$	$\eta_A \eta_B$
104	4.40	0.198	20	72.03	39.5	35.5	41.5	0.048	0.694	0.992	0.688
104	4.40	0.250	18	72.24	34.0	37.0	37.2	0.047	0.729	0.967	0.705
104	4.40	0.250	20	72.05	39.0	38.5	38.8	0.048	0.697	0.977	0.681
104	4.40	0.250	22	71.83	47.0	39.5	40.6	0.048	0.663	0.983	0.652
118.75	4.40	0.250	20	73.22	36.5	40.5	36.5	0.042	0.700	0.971	0.680
140	4.40	0.250	20	74.59	33.5	33.5	35.9	0.036	0.690	0.946	0.653
140	4.40	0.250	22	74.35	36.2	33.6	35.7	0.036	0.654	0.946	0.619
183	4.40	0.250	20	76.97	36.0	42.5	36.0	0.028	0.698	0.969	0.676

\* Because of the large effective f/D ratio of the Cassegrain antenna, the taper on the main reflector is approximately the same as that on the subreflector.

ORIGINAL PAGE IS  
OF POOR QUALITY

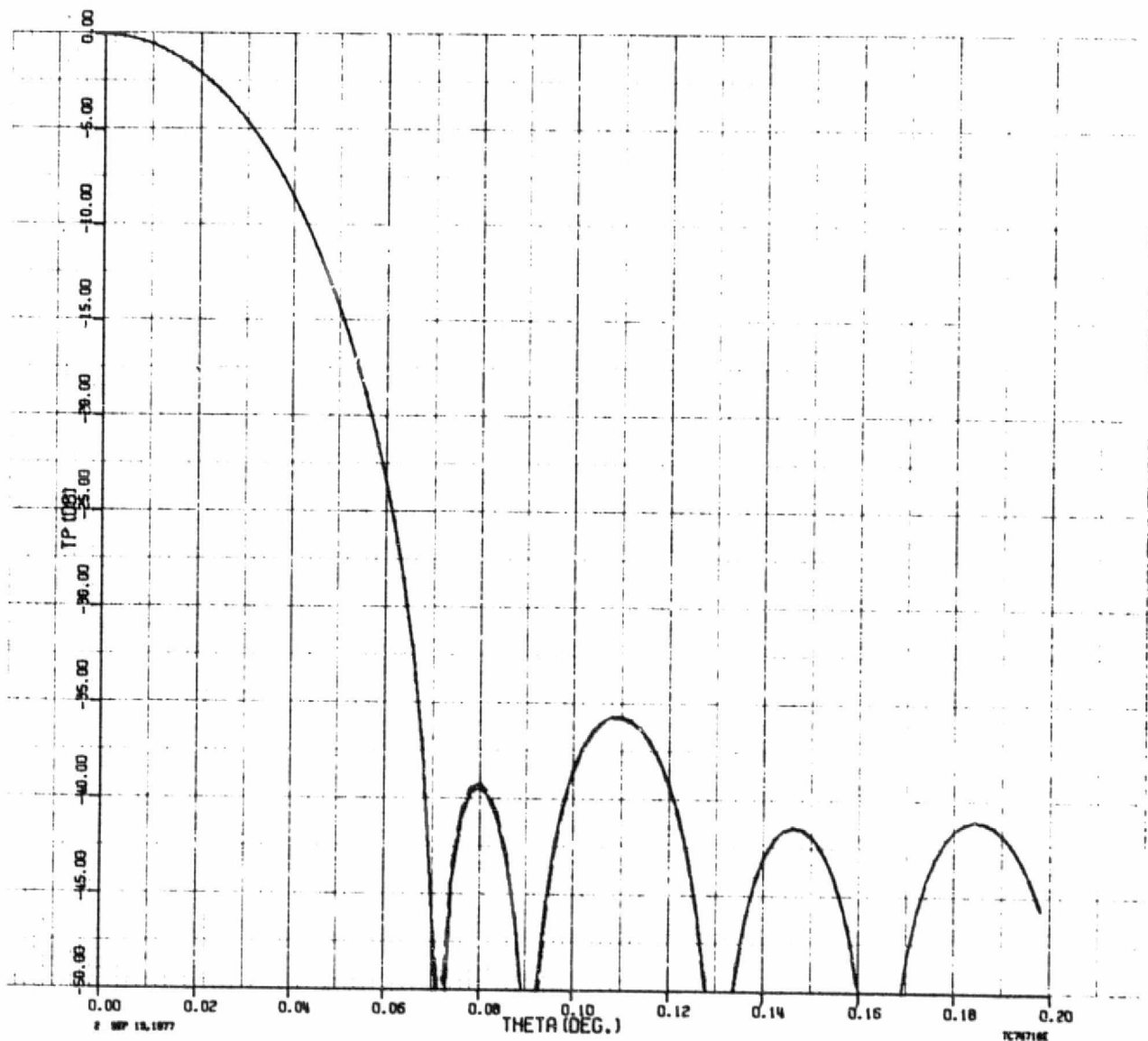


Figure 4. Calculated E-plane and H-plane patterns for 20 dB taper, 0.198 meter diameter subreflector. Frequency 104 GHz.

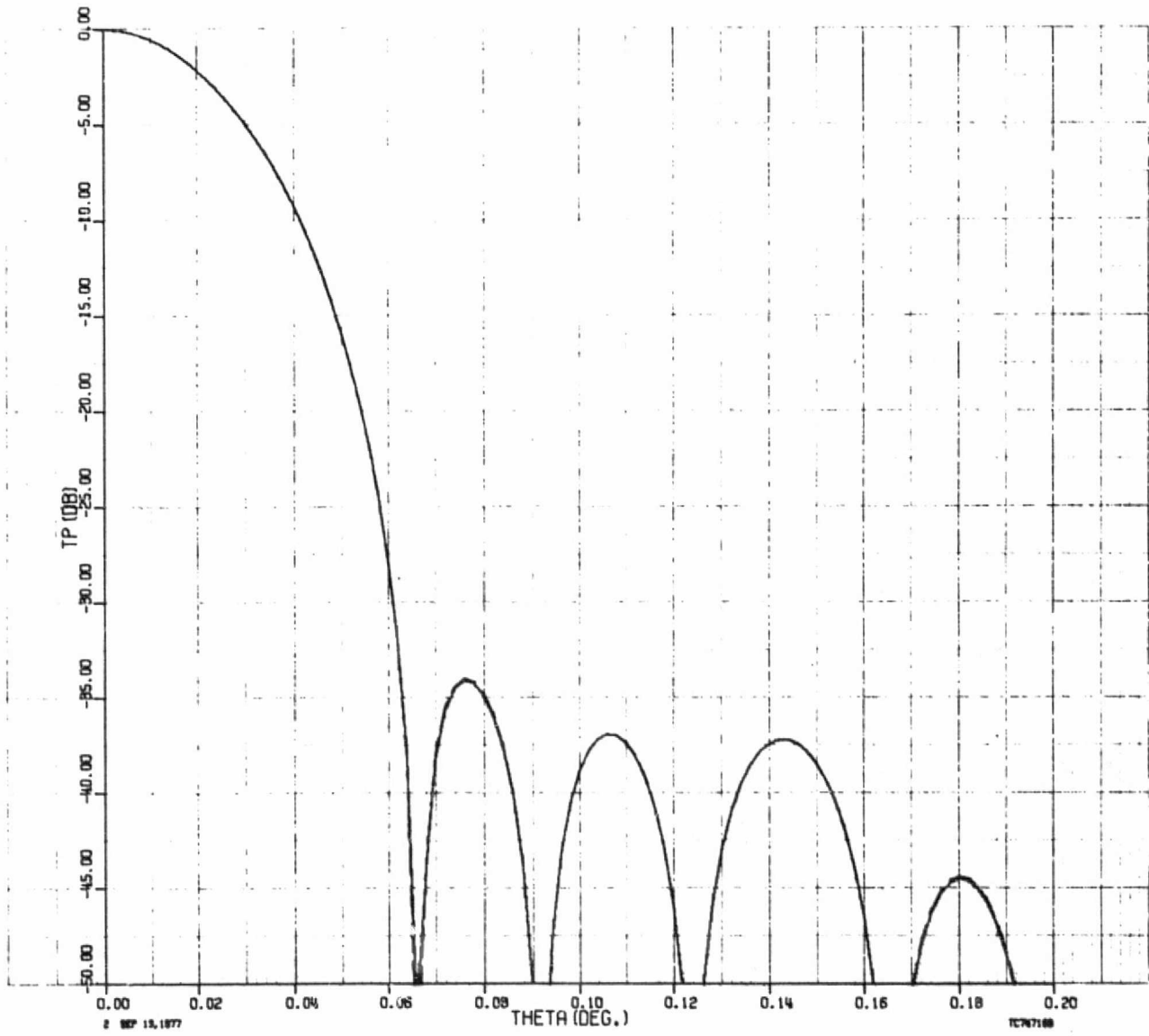


Figure 5. Calculated E-plane and H-plane patterns for 18 dB taper, 0.25 meter diameter subreflector. Frequency 104 GHz.

ORIGINAL PAGE IS  
OF POOR QUALITY

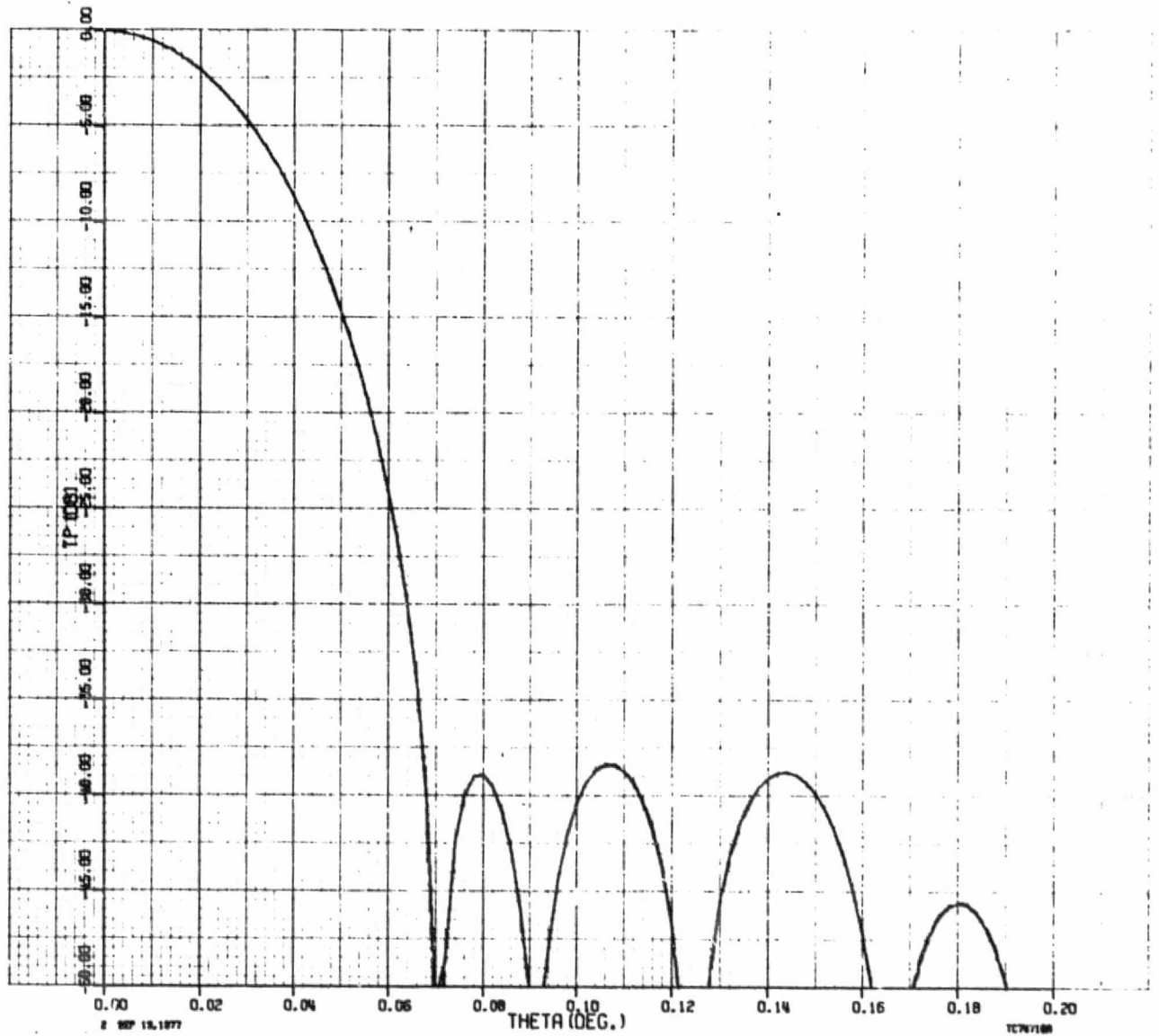


Figure 6. Calculated E-plane and H-plane patterns for 20 dB taper, 0.25 meter diameter subreflector. Frequency 104 GHz.

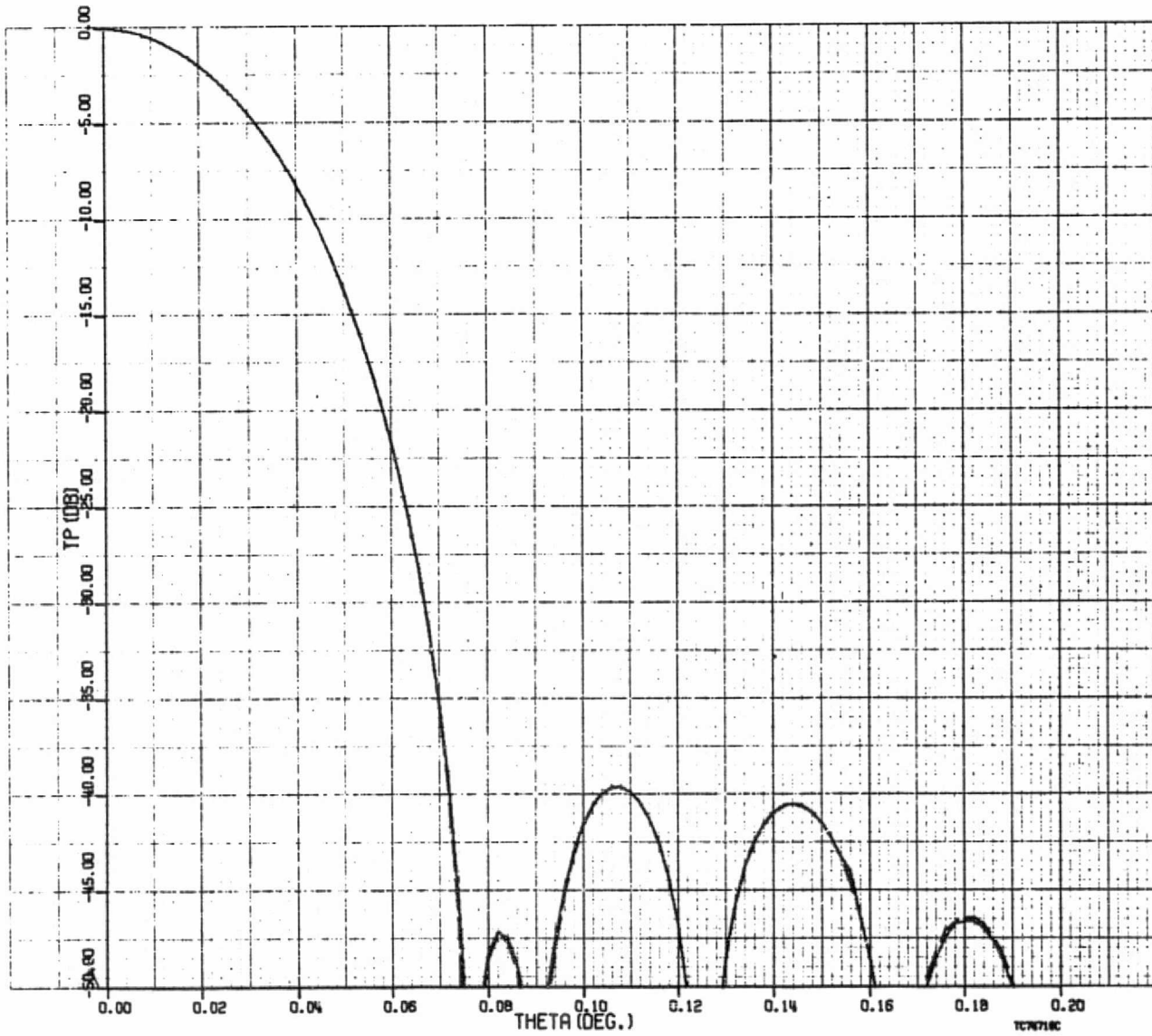


Figure 7. Calculated E-plane and H-plane patterns for 22 dB taper, 0.25 meter diameter subreflector. Frequency 104 GHz.

ORIGINAL PAGE IS  
OF POOR QUALITY

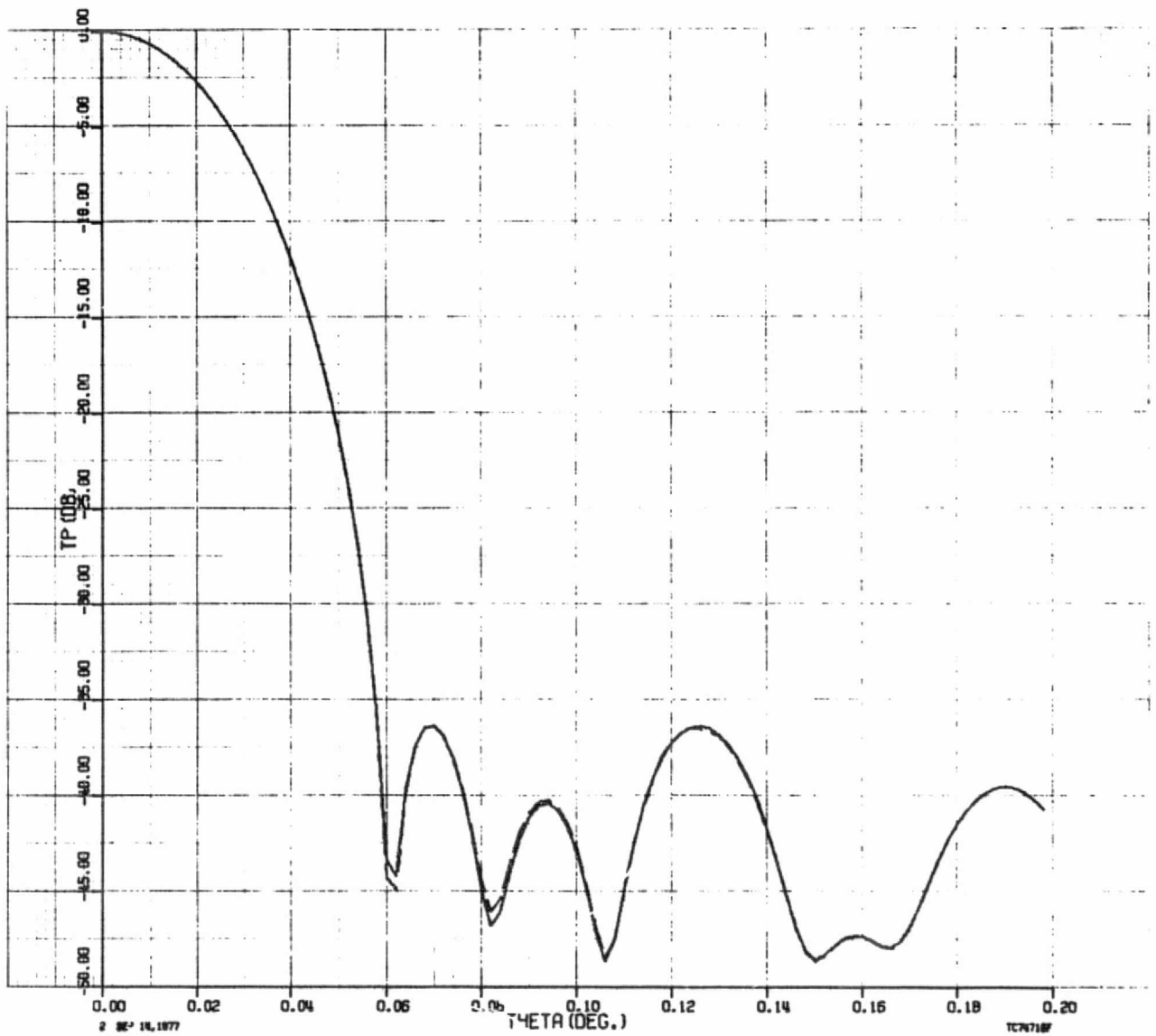


Figure 8. Calculated E-plane and H-plane patterns for 20 dB taper, 0.25 meter diameter subreflector. Frequency 118.75 GHz.

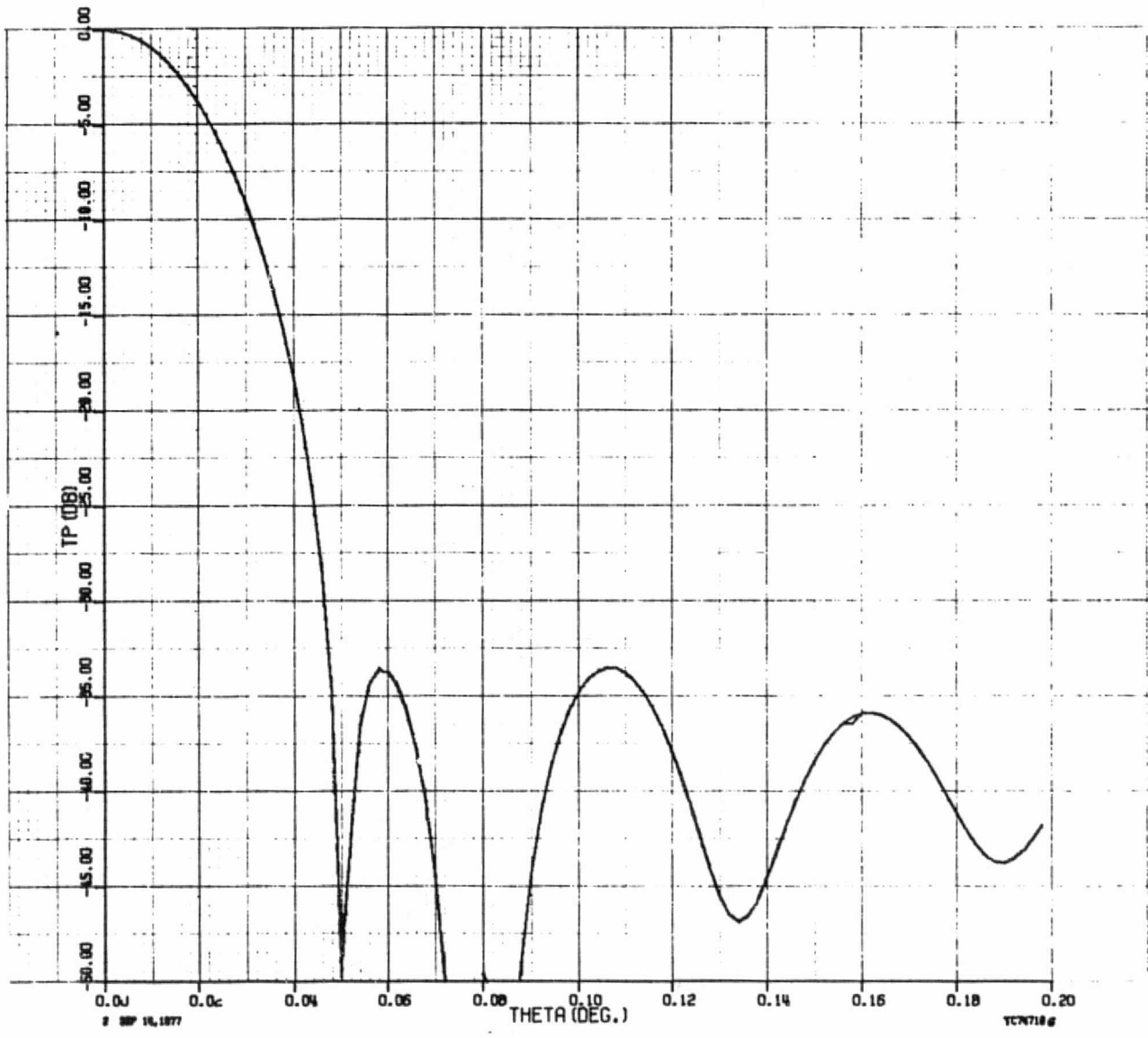


Figure 9. Calculated E-plane and H-plane patterns for 20 dB taper, 0.25 meter diameter subreflector. Frequency 140 GHz.

ORIGINAL PAGE IS  
OF POOR QUALITY

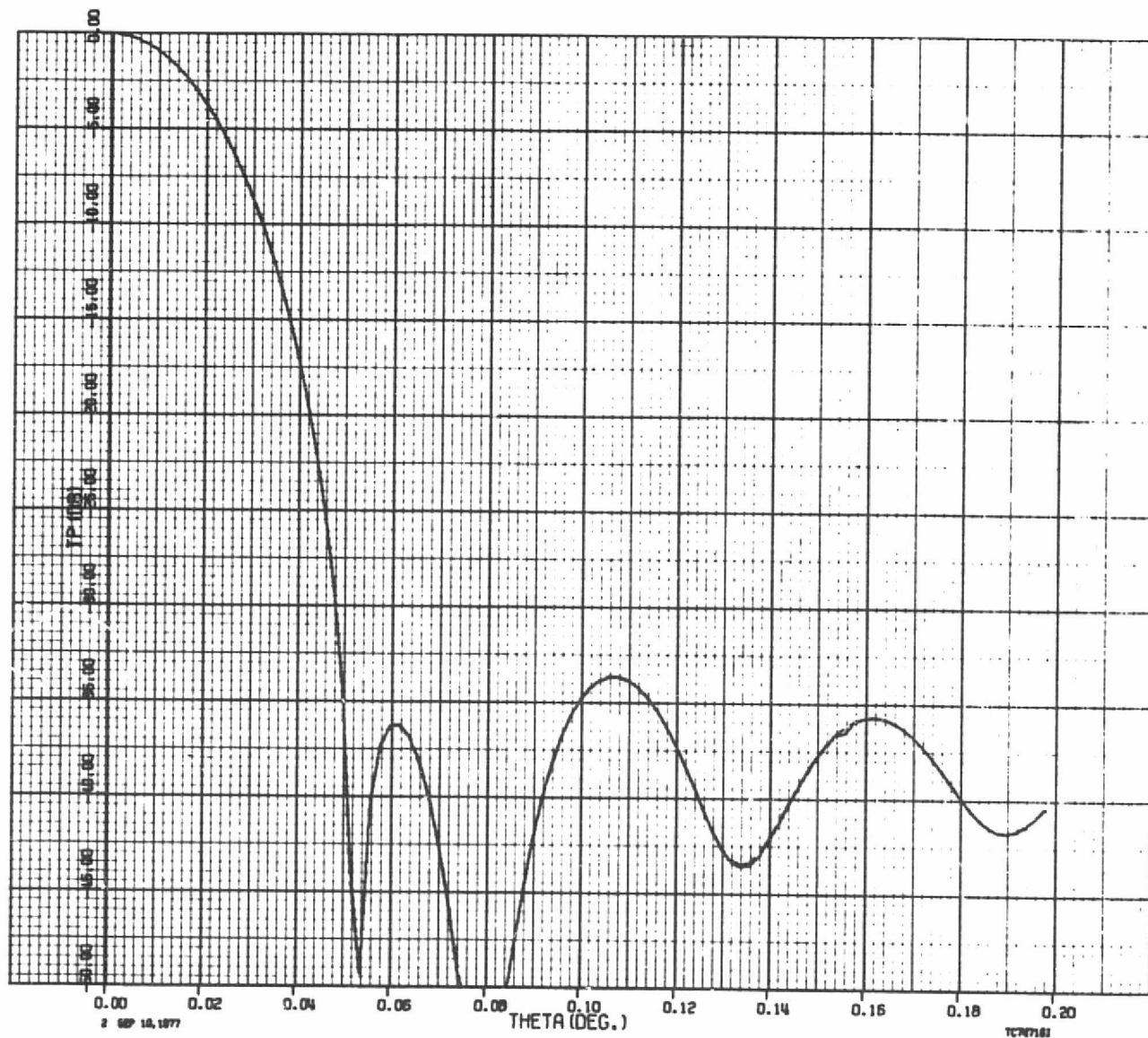


Figure 10. Calculated E-plane and H-plane patterns for 22 dB taper, 0.25 meter diameter subreflector. Frequency 140 GHz.



ORIGINAL PAGE IS  
OF POOR QUALITY

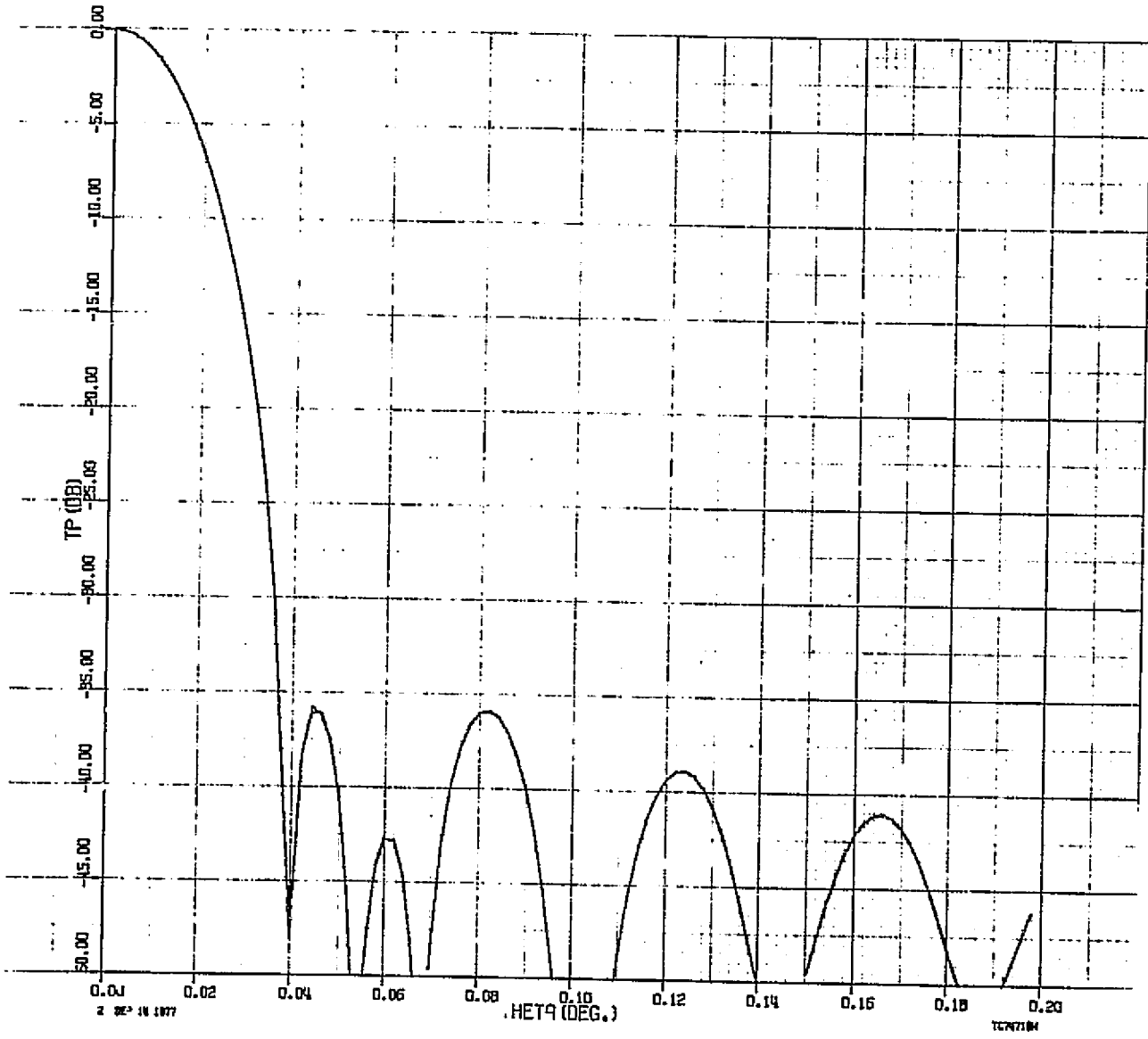


Figure 11. Calculated E-plane and H-plane patterns for 20 dB taper, 0.25 meter diameter subreflector. Frequency 183 GHz.

### 2.4.1.3 Forward Spillover

In the Cassegrain antenna configuration forward spillover results when the subreflector is illuminated by the feed. This forward spillover lies in a region within a few degrees of the main beam and views the earth during the mapping process. As long as the conventional beam efficiency is above the minimum value of 85 percent, the fact that the forward spillover views the earth does not invalidate antenna performance characteristics. However, during primary calibration, the main beam of the antenna looks at the cold sky 10 degrees from the earth center, while a portion of the forward spillover still views the earth and could provide a significant contribution to the calibration temperature.

The effect of forward spillover on the antenna temperature may be considered as follows. The antenna pattern,  $E(\theta, \phi)$ , may be written as the sum of two patterns,  $E_o(\theta, \phi)$ , the pattern without forward spillover, plus  $E_{sp}(\theta, \phi)$ , that due to forward spillover. The directive gain function may then be written as follows:

$$G(\theta, \phi) = \frac{4\pi |E(\theta, \phi)|^2}{\iint_{4\pi} |E(\theta, \phi)|^2 d\Omega} \quad (12a)$$

$$G(\theta, \phi) = \frac{4\pi \left[ |E_o|^2 + E_o E_{sp}^* + E_o^* E_{sp} + |E_{sp}|^2 \right]}{\iint_{4\pi} \left[ |E_o|^2 + E_o E_{sp}^* + E_o^* E_{sp} + |E_o|^2 \right] d\Omega} \quad (12b)$$

where the asterisk denotes complex conjugate and  $d\Omega$  is the element of solid angle.

The antenna temperature, neglecting the effect of dissipation losses is given by the following expression:

$$T_A = \frac{1}{4\pi} \iint_{4\pi} G(\theta, \phi) T(\theta, \phi) d\Omega \quad (13)$$

On substituting (12) into (13) the following expression is obtained:

$$T_A = \frac{\iint_{4\pi} [ |E_o|^2 + E_o E_{sp}^* + E_o^* E_{sp} + |E_{sp}|^2 ] T(\theta, \phi) d\Omega}{\iint_{4\pi} [ |E_o|^2 + E_o E_{sp}^* + E_o^* E_{sp} + |E_{sp}|^2 ] d\Omega} \quad (14)$$

The integrals of the cross products of  $E_o$  and  $E_{sp}$  will be small because  $E_o$  will oscillate rapidly since it comes from a much larger aperture than  $E_{sp}$ . Equation (14) may then be approximated as follows:

$$T_A = \frac{\iint [ |E_o|^2 + |E_{sp}|^2 ] T(\theta, \phi) d\Omega}{\iint [ |E_o|^2 + |E_{sp}|^2 ] d\Omega} \quad (15a)$$

$$T_A = \frac{\iint T |E_o|^2 d\Omega}{\iint [ |E_o|^2 + |E_{sp}|^2 ] d\Omega} + \frac{\iint T |E_{sp}|^2 d\Omega}{\iint [ |E_o|^2 + |E_{sp}|^2 ] d\Omega} \quad (15b)$$

The integral over  $|E_o|^2$  can be separated into the portion over the main beam and the portion over the sidelobes. Let  $I_D$  be the integral in the denominator in Eqs. 15. Then the integral over the main beam is  $\eta_B I_D$  and the integral over the spillover is  $\eta_S I_D$  where  $\eta_B$  is the beam efficiency and  $\eta_S$  is the fraction of energy in spillover. The fraction of energy in sidelobes other than spillover is  $1 - \eta_B - \eta_S$ . The antenna temperature may now be written as follows:

$$T_A = \frac{\iint_{\text{main beam}} T |E_o|^2 d\Omega}{I_D} + \frac{\iint_{\text{sidelobes}} T |E_o|^2 d\Omega}{I_D} + \frac{\iint T |E_{sp}|^2 d\Omega}{I_D} \quad (16a)$$

$$= \eta_B \bar{T}_B + (1 - \eta_B - \eta_S) \bar{T}_S + \eta_S \bar{T}_{sp} \quad (16b)$$

where

$\bar{T}_B$  is the average temperature in the main beam

$\bar{T}_S$  is the average temperature over the sidelobe region

$\bar{T}_{sp}$  is the average temperature seen by the spillover.

Thus the contribution of the forward spillover is  $\eta_S \bar{T}_{sp}$ . During operation essentially all the forward spillover will look at the earth, which has an average temperature of  $\bar{T}_e$  degrees. Thus the forward spillover will cause a contribution  $\eta_S \bar{T}_e$  to the antenna temperature.

When the antenna beam is pointed to 10 degrees from the center of the earth, the earth will intercept a fraction,  $\eta_e$ , of the forward spillover. The remaining forward spillover will see essentially cold sky at temperature  $T_{sky}$ . The contribution of the forward spillover to the antenna temperature at calibration is then

$$\eta_S \left[ \eta_e \bar{T}_e + (1 - \eta_e) T_{sky} \right]$$

The excess caused by the earth is then given by the following expression:

$$\eta_S \eta_e \bar{T}_e$$

For the earth viewed from synchronous orbit  $\eta_e$  is approximately 0.34 (Figure 12).

For the case of a true Gaussian-beam feed providing a 20 dB taper at the edge of a 0.198 meter diameter subreflector,  $\eta_S = 0.01$ , i.e., 1 percent of the total energy is contained in forward spillover. Of this amount about 34 percent views the earth during primary calibration, resulting in a contribution of  $\bar{T}_e$  (0.0034). For an assumed  $\bar{T}_e$  of 259.5°K the contribution of forward spillover to the calibration temperature is 0.88°K. However, if the subreflector diameter is increased to 0.25 meter the forward spillover is only 0.065 percent ( $\eta_S = 0.00065$ ) resulting in a contribution of 0.06°K to the calibration temperature.

ORIGINAL PAGE IS  
OF POOR QUALITY

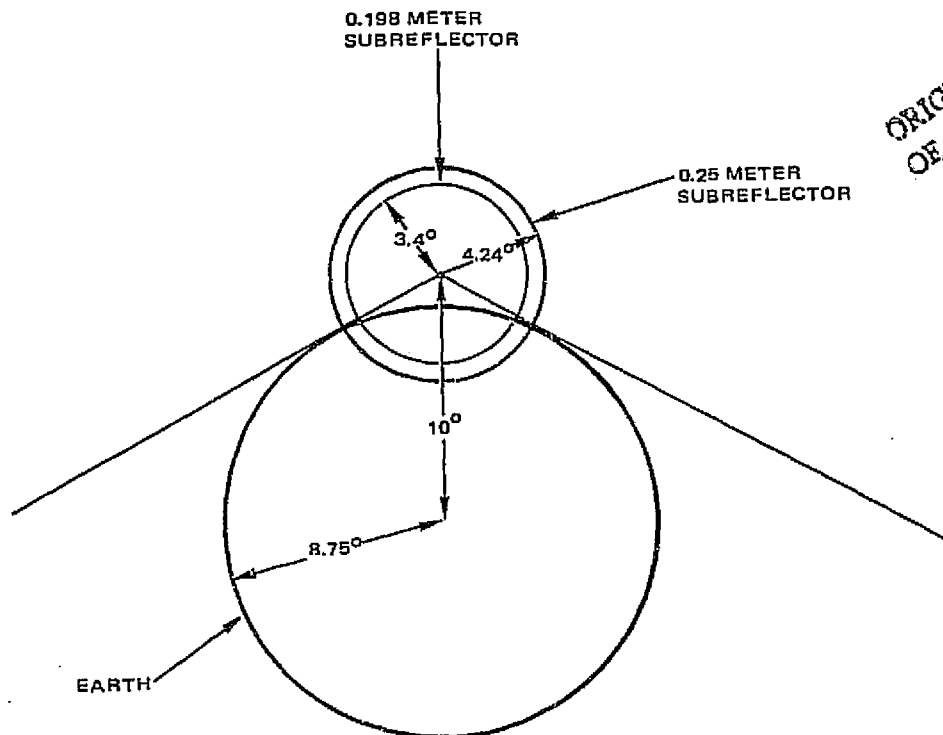


Figure 12. Relationship of subreflector and earth disc as seen from feed point.

As stated in Section 2.4.1.1 the assumption that the feed is exactly Gaussian is an approximation so that the values cited here are subject to change when a more detailed design study is undertaken, but they indicate the trends to be expected.

#### 2.4.1.4 Aperture Blockage and Shadowing

The effects of subreflector and strut blockage and shadowing have been estimated for the general case of tapered struts that join the main reflector at some radius  $\rho_0$ . The configuration is illustrated in Figure 13. In the region  $\rho < \rho_0$ , the subreflector and struts block the waves traveling outward from the main reflector, while in the region  $\rho_0 < \rho < D/2$  the struts intercept rays traveling from the subreflector to the main reflector, casting a shadow on the main reflector. Since in this application the

ORIGINAL PAGE IS  
OF POOR QUALITY

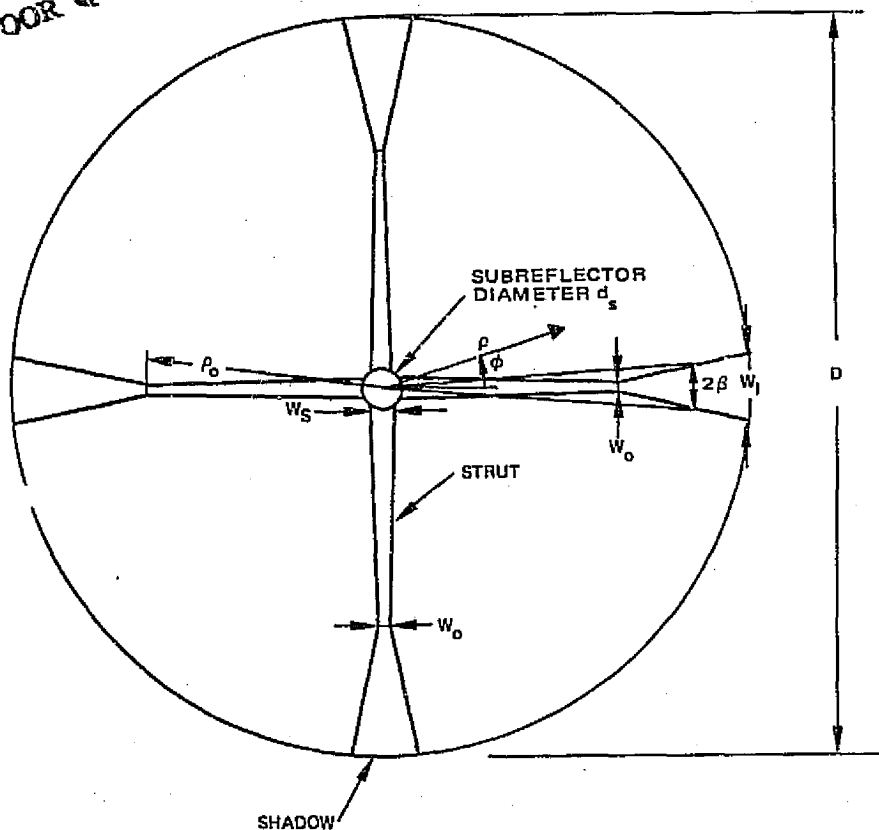


Figure 13. Blockage and shadowing effects.

transverse dimensions of the struts will be large in terms of wavelength, the blockage and shadowing will be essentially optical in nature. With this approximation, the effective width of the struts may be written as follows:

$$w(\rho) = w_s + \frac{(w_o - w_s)}{\left(\rho_o - \frac{d_s}{2}\right)} \left(\rho - \frac{d_s}{2}\right) \quad \frac{d_s}{2} < \rho < \rho_o \quad (17)$$

where  $w_s$  is the strut width at the edge of the subreflector and  $w_o$  is the strut width at  $\rho_o$ , and  $d_s$  is the diameter of the subreflector.

The shadow region  $\rho_0 < \rho < D/2$  covers an angle  $2\beta$ , where  $\beta$  may be approximated by the following expression:

$$\beta(\rho) \approx \frac{w_0}{2\rho_0} + \frac{\left(\frac{w_1}{D} - \frac{w_0}{2\rho_0}\right)}{\left(\frac{D}{2} - \rho_0\right)}(\rho - \rho_0) \quad \rho_0 < \rho < \frac{D}{2} \quad (18)$$

where  $w_1$  is the width of the shadow at the reflector edge. The width,  $w_1$ , is determined by the position at which the struts join the main reflector, the F/D ratio of the main reflector, the diameter and eccentricity of the sub-reflector, and the strut diameter.

Equation 18 is derived in Appendix A.

The aperture field strength,  $E_a$ , in the absence of blockage and shadowing is approximated by a Gaussian distribution given by the following expression.

$$E_a(\rho) = E_0 e^{-\alpha^2 \rho^2} \quad (19)$$

where  $E_0$  is the field strength at the aperture center and  $\alpha$  is a measure of the aperture taper. It is given by

$$\alpha^2 = \frac{N}{5 D^2 \log_{10} e} \quad (20)$$

where  $N$  is the aperture taper in dB. Let  $R$  denote the field strength on axis including blockage and shadowing relative to the field strength on axis in the absence of blockage and shadowing. An expression for  $R$  is given in Appendix A.

The relative power on axis is given by  $R^2$ . The power that is removed from the main beam by blockage and shadowing is scattered elsewhere in space. The blockage and shadowing have been evaluated for various strut diameters, tapers, and  $\rho_0$ , and the results are tabulated in Table VI for a 20 dB taper.

TABLE VI. EFFECT OF SUBREFLECTOR AND STRUT BLOCKAGE

Strut Diameter, cm		Radius Where Fastened to Main Ref	$R^2$ Subreflector Blockage Only	$R^2$ Subreflector and Strut Blockage and Shadowing
At Subref	At Main Ref			
2.54	2.54	2.199	0.984	0.946
2.54	2.54	1.467	0.984	0.929
5.08	5.08	1.467	0.984	0.880
5.08	5.08	2.199	0.984	0.909
7.62	2.54	1.467	0.984	0.870
7.62	2.54	1.150	0.984	0.836
5.08	5.08	1.150	0.984	0.851

It is apparent that if care is not taken to design for minimum strut size the loss can be significant. Minimizing strut size will be a portion of the design phase on the next program.

#### 2.4.1.5 Contribution of Reflector Losses to Antenna Temperature

The dissipation losses in the reflectors will contribute to the antenna noise temperature. Their contribution may be computed as follows. Let  $T_a$  represent the antenna temperature without dissipation and  $T_{r1}$  and  $T_{r2}$  the temperatures of the first and second reflector, respectively. The reflection coefficients of the reflectors are denoted by  $\Gamma_1$  and  $\Gamma_2$ , where  $\Gamma$  is the voltage reflection coefficient given by the following expression:

$$\Gamma = \frac{\sqrt{j\omega\mu_0/\sigma} - \eta_0}{\sqrt{j\omega\mu_0/\sigma} + \eta_0}$$

where  $\omega$  is the angular frequency,  $\sigma$  is the effective conductivity of the metal,  $\eta_0$  is the impedance of free space, and  $\mu_0$  is the permeability of free space.



Then, the system may be represented by Figure 14. The noise power generated by a reflector is  $T_r (1 - |\Gamma|^2)$ . Thus, by following the noise powers through the system the temperature out is given by

$$\begin{aligned}
 T_{\text{out}} = & T_a + (T_{r_1} - T_a) (1 - |\Gamma_1|^2) \\
 & + (T_{r_2} - T_a) (1 - |\Gamma_2|^2) \\
 & - (T_{r_1} - T_a) (1 - |\Gamma_1|^2) (1 - |\Gamma_2|^2)
 \end{aligned}
 \tag{22}$$

For aluminum at 193 GHz, the upper edge of the frequency range,  $\Gamma = 0.99924/179.956^{\circ}$  where the reflection coefficient was calculated for a smooth conductor with surface resistance  $3.26 \times 10^{-7} \sqrt{f^*}$ . Then

$$1 - |\Gamma|^2 = 0.00152
 \tag{23}$$

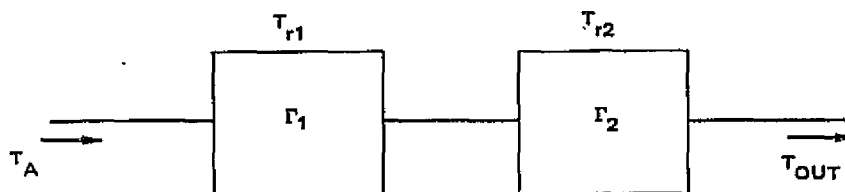


Figure 14. Model for antenna loss temperature calculation.

---

\*The value of surface resistance is based on the d.c. conductivity of  $3.72 \times 10^7$  mhos/meter. (Ramo, S. and J.R. Whinnery Fields and Waves in Modern Radio, John Wiley & Sons, Inc., New York, 1953, p. 240.)

The antenna temperature will then be given by the following expression:

$$T_{\text{out}} = T_a + (T_{r_1} + T_{r_2} - 2T_a) (0.00152) + (T_{r_1} - T_a) (0.00152)^2 \quad (24)$$

If we assume that the antenna is at a physical temperature of 300°K and the lossless antenna temperature,  $T_a$ , is say, 5°K, then the losses contribute an additional 0.90 degree to the 5 degree temperature. Since the antenna temperature will fluctuate, this contribution will also fluctuate.

In actuality, the reflector surfaces will have a layered coating for environmental protection that could influence the noise temperature contribution by modifying  $\Gamma$ . Though the details of the coating are proprietary with General Dynamics, the following general analysis of layered media has been provided by General Dynamics.

Coating Performance 104-193 GHz. The theoretical performance (reflectivity and absorption) of the coating design may be analyzed in the following manner. Each layer may be represented by a 2-by-2 matrix,  $M_\ell$ . The stack of  $m$  layers may be represented as a product of the matrices. The equations are as follows:

$$\begin{bmatrix} A & B \\ C & D \end{bmatrix} = \prod_{\ell=1}^m M_\ell \quad (25a)$$

$$Y = \frac{C + D}{B + A} \quad (25b)$$

$$R = \left\{ \frac{1 - Y}{1 + Y} \right\} \cdot \left\{ \frac{1 - Y}{1 + Y} \right\}^* \quad (25c)$$

Y = normalized input admittance of the stack

R = power reflection coefficient of the stack

$$M_{\ell} = \text{characteristic matrix of layer} = \begin{bmatrix} \cos \delta_{\ell} & \frac{j \sin \delta_{\ell}}{n} \\ j n_{\ell} \sin \delta_{\ell} & \cos \delta_{\ell} \end{bmatrix} \quad (25d)$$

$n_{\ell}$  = (complex) index of refraction of layer

$\delta_{\ell}$  = optical thickness of the layer

The following value was used for the index of refraction of the dielectric layers,

$$n_d = 2.2 - j 7.7 \times 10^{-3}$$

which is based on available handbook data. The index of refraction and extinction coefficients\* for aluminum were obtained in the following manner. We have, in general:

$$n^2 - k^2 = 1 - \frac{\omega_p^2}{\omega^2 + \tau^{-2}} \quad (25a)$$

$$nk = \frac{\omega_p^2}{2\omega\tau(\omega^2 + \tau^{-2})} \quad (25b)$$

where

$\omega_p$  = plasma frequency of metal considered

$\tau$  = relaxation time of electrons

$\omega$  = angular frequency of radiation

---

\*M. Born and E. Wolf, Principles of Optics. Pergamon Press, New York, Fifth Edition, 1975, p. 613.

n = real part of index of refraction  
k = imaginary part of index of refraction.

For aluminum we have\*

$$\omega_p = 2.2 \times 10^{16} \text{ sec}^{-1}$$

$$\tau = 8.0 \times 10^{-15} \text{ sec.}$$

Using Equation (26), we find for aluminum:

105 GHz	n = 1710
	<u>k = 1720</u>
150 GHz	n = 1430
	<u>k = 1440</u>
190 GHz	n = 1270
	<u>k = 1280</u>

As expected, the metal becomes more transparent as the radiation frequency increases toward the plasma frequency. Using these constants the reflection coefficient of the layered coating at 150 GHz has been calculated to be  $|\Gamma| = 0.9993$ , so that  $R \equiv |\Gamma|^2 = 0.9986$ . This is essentially the same result obtained for thick uncoated aluminum and agrees well with the value obtained using the dc conductivity. The reflections at various frequencies are compared in Table VII. It is concluded from these calculations that the coating will have a negligible effect on electrical performance. Measurement of the actual surface reflection coefficients would be necessary to arrive at better estimates of the reflector dissipative losses over the frequency band. No such measurements are presently available at the frequencies of interest.

---

\*H. E. Bennet and J. M. Bennet, "Validity of the Drude Theory for Silver, Gold, and Aluminum in the Infrared." Optical Properties and Electronic Structure of Metals and Alloys, Proceedings of International Colloquium, Paris, Dept. 1965.

TABLE VII. COMPARISON OF REFLECTION COEFFICIENTS OF LAYERS AND UNCOATED SOLID ALUMINUM

Frequency	R	R	R
GHz	Layered Medium*	Uncoated Solid Aluminum*	Uncoated Solid Aluminum**
105	-	0.9988	0.9989
150	0.9986	0.9986	0.9987
190	-	0.9984	0.9985

\*Using Index of Refraction from Equations 26.  
 \*\*Using dc conductivity,  $3.72 \times 10^7$  mhos/meter.

#### 2.4.1.6 Effects of Tolerances

In order to evaluate analytically the effect of path length errors on a specific antenna it is first necessary to measure the errors over the aperture and to use these errors in computing the performance characteristics of the antenna. For example, the directive gain function,  $G(\theta, \phi)$ , of an aperture antenna (neglecting spillover and cross polarization effects) may be computed by using the following scalar formula.

$$G(\theta, \phi) = \frac{4\pi}{\lambda^2} \frac{\left| \iint_{ap} f(\bar{\rho}) e^{j\bar{k} \cdot \bar{\rho}} e^{j\zeta(\bar{\rho})} \rho \, d\rho d\phi' \right|^2}{\iint_{ap} |f(\bar{\rho})|^2 \rho \, d\rho d\phi'} \quad (27)$$

This is the same formula used by Ruze\* in his statistical analysis where

$f(\bar{\rho})$  is the aperture amplitude distribution,

$\bar{k}$  is the propagation vector which is directed from the aperture point  $\rho, \phi'$ , to the observation point,

$\zeta(\bar{\rho})$  is the phase error over the aperture,

$\bar{\rho}$  is the positional vector in the aperture.

$\lambda$  is wavelength.

When specific data on a particular antenna are used the characteristics of that antenna can then be calculated approximately. If the phase errors are

\*J. Ruze, "Antenna Tolerance Theory," Proc. IEEE, 54, 633-640, 1966.

small, the first few terms of  $e^{j\zeta}$  may be used to approximate the performance as in the following expression:

$$G(\theta, \phi) = \frac{-j\pi}{\lambda^2} \frac{\left| \iint f(\bar{\rho}) e^{j\bar{k} \cdot \bar{\rho}} \rho d\rho d\phi' + j \iint f(\bar{\rho}) e^{j\bar{k} \cdot \bar{\rho}} \zeta(\bar{\rho}) \rho d\rho d\phi' - \iint f(\bar{\rho}) e^{j\bar{k} \cdot \bar{\rho}} \zeta^2(\bar{\rho}) \rho d\rho d\phi' \right|^2}{\iint |f(\bar{\rho})|^2 \rho d\rho d\phi'} \quad (28)$$

For on-axis gain,  $\bar{k} \cdot \bar{\rho} = 0$ , and the numerator takes the following form:

$$\text{Num} = \left| \iint f(\bar{\rho}) \rho d\rho d\phi' + j \iint f(\bar{\rho}) \zeta(\bar{\rho}) \rho d\rho d\phi' - \iint f(\bar{\rho}) \zeta^2(\bar{\rho}) \rho d\rho d\phi' \right|^2 \quad (29)$$

It is possible to choose the phase reference so that, for a specified aperture taper function,  $f(\bar{\rho})$ , the middle term vanishes. In that case the third term is sometimes called a weighted square phase error and when normalized to the first term is called the mean squared phase error over the aperture. It has meaning only if  $\zeta$  is sufficiently small to justify the series expansion and it provides information only about on-axis gain. For points off axis equation (27) or (28) must still be used. The quantity  $\zeta$  is a particular function of  $\bar{\rho}$  and is not a statistical quantity. In order to obtain an estimate of what to expect on the average from a number of antennas, the quantity  $\zeta$  must be viewed as a typical member of an ensemble of functions that describe the phase errors of the various antennas. In that case statistical averages may be computed. However, a knowledge of how the statistics of the phase errors vary with radius is necessary to perform the computations. This is the approach taken by Ruze\*. However, to make the mathematics tractable he makes the additional assumption that the statistics of the phase errors are independent of the radius, which is equivalent to saying that the path length errors are likely to be as great near the reflector center as they will be near its edge, which may not be the case in practice. However, his approach does appear to yield useful results and is used in this study to estimate the effects of surface tolerances on antenna performance.

---

\*J. Ruze, "Antenna Tolerance Theory," Proc. IEEE, 54, 633-640, 1966.

The effects of surface irregularities in reflectors are increased sidelobe levels and reduced beam efficiencies. These effects have been discussed for large pencil beam antennas and the results are pertinent to the radiometer study. In terms of an rms effective surface error,  $\epsilon$ , the mean gain pattern is given by the following equation:

$$G(\theta, \phi) = G_0(\theta, \phi) e^{-\delta^2} + \left(\frac{2\pi c}{\lambda}\right)^2 e^{-\delta^2} \sum_{n=1}^{\infty} \frac{\delta^{2n}}{n \cdot n!} e^{-(\pi c u / \lambda)^2 / n} \quad (30)$$

where

$$u = \sin \theta$$

$c$  = correlation distance of the surface ( $c \ll$  diameter)

$$\delta = 4\pi \epsilon / \lambda$$

The first term on the right-hand side is the unperturbed pattern multiplied by a factor  $e^{-\delta^2}$  that reduces the gain. The second term is a rather broad pattern that affects the peak gain somewhat but affects mainly the sidelobe level. For a given design peak sidelobe level, this term must be sufficiently below the design level that the latter is not changed significantly.

As an example of the magnitude of this term relative to the beam peak, the expression was evaluated for a  $2840\text{-}\lambda$  aperture for two values of  $\epsilon / \lambda$ ,  $1/16$  and  $1/32$ , which at 193 GHz represents rms errors of approximately 2 and 1 mils, respectively, over a 4.4-meter aperture. A correlation distance of  $50\epsilon$  was assumed in the calculations. For the case of  $\epsilon / \lambda = 1/32$ , the term near the beam axis is down about -60 dB from the peak or about 35 dB below a -25 dB sidelobe level. This value has a negligible effect on the near-in sidelobe levels. An rms error of  $1/16$  results in an error term of about -53 dB below the beam peak, still well below a -25 dB sidelobe level.

The beam efficiency may be obtained by integration of Equation (30) over the main beam and comparison of the result with an integration over all angles. The resulting expression is as follows.

$$E(\theta_1) = e^{-\delta^2} \left[ E_0(\theta_1) + \sum_{n=1}^{\infty} \frac{\delta^{2n}}{n!} \left( 1 - e^{-\frac{(\pi c \sin \theta_1 / \lambda)^2}{n}} \right) \right] \quad (31)$$

where  $\theta_1$  represents the beam edge and the term  $E_0(\theta_1)$  is the beam efficiency without any errors. The summation represents power in the main beam due to scattering by surface irregularities and is generally much smaller than  $E_0$ . It is seen that the beam efficiency is essentially reduced by the factor  $e^{-\delta^2}$ ; therefore, for a high beam efficiency, the rms phase error  $\delta$  must be kept small.

For the narrow beamwidths obtained with the 4.40 meter antenna the summation contributes a negligible amount so that the beam efficiency is given essentially by the following expression:

$$E(\theta_1) = E_0(\theta_1) e^{-\delta^2} \quad (32)$$

The beam efficiency in the presence of random errors is the zero-error efficiency multiplied by a factor involving the effective surface tolerance. This factor is plotted in Figure 15.

For deep reflectors, the surface error is not exactly equal to the effective error,  $\epsilon$ , because the rays do not all strike the surface normally, but at varying angles across the reflector. The parameter has been related to the actual surface errors, but in actuality it is somewhat less than the rms surface error. For example, if  $\Delta n$  represents the surface error



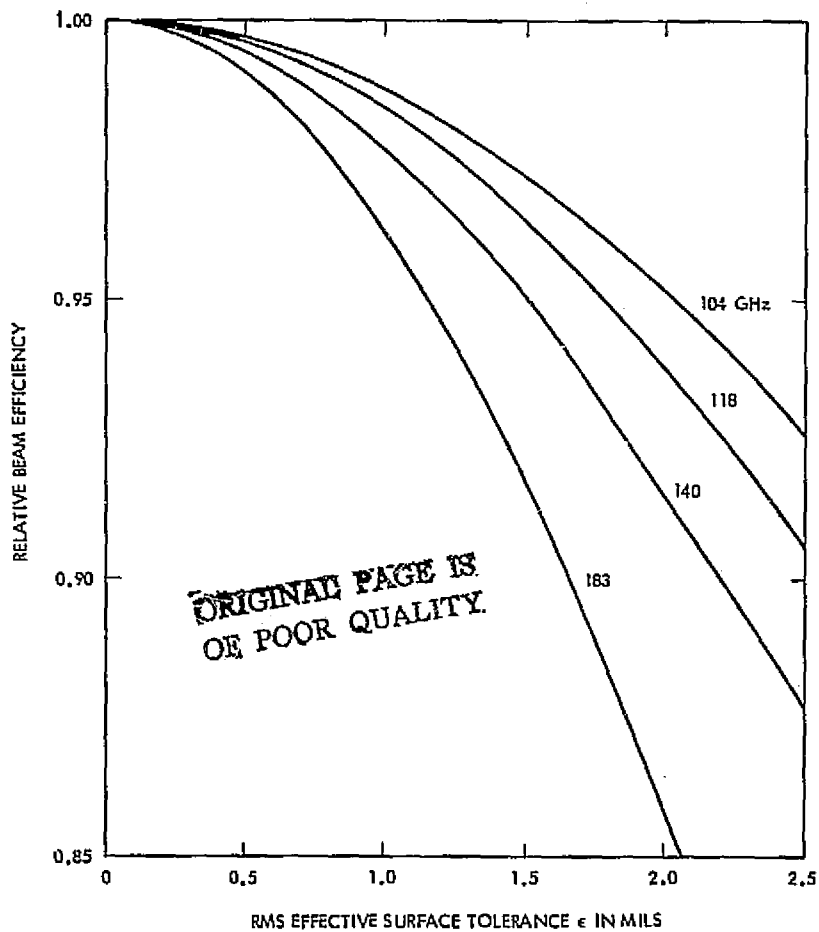


Figure 15. Effect of surface tolerance on beam efficiency.

measured normal to a paraboloidal surface at a radius  $\rho$  from the paraboloidal axis, then the effective error  $\epsilon(\rho)$  at that radius is

$$\epsilon(\rho) = \frac{\Delta n}{\sqrt{1 + (\rho/2f)^2}} \quad (33)$$

If this effective error is averaged over the aperture, the resulting value is given by

$$\epsilon = \Delta n \cdot 32 \left(\frac{f}{D}\right)^2 \left[ \sqrt{1 + \left(\frac{D}{4f}\right)^2} - 1 \right] \quad (34)$$

For an  $f/D$  of 0.35, this expression gives  $\epsilon = 0.897 \Delta n$  or  $\Delta n = 1.114 \epsilon$ .

The beam efficiency relative to the zero-error beam efficiency is plotted as a function of  $\Delta n$  in Figure 16. It is evident that at 183 GHz the rms surface tolerance must be kept very small. For example, the relative beam efficiency for a 1.7 mil rms tolerance is 0.916. Therefore, the zero-error beam efficiency must be at least 92.8 percent if the 85 percent overall beam efficiency is to be met.

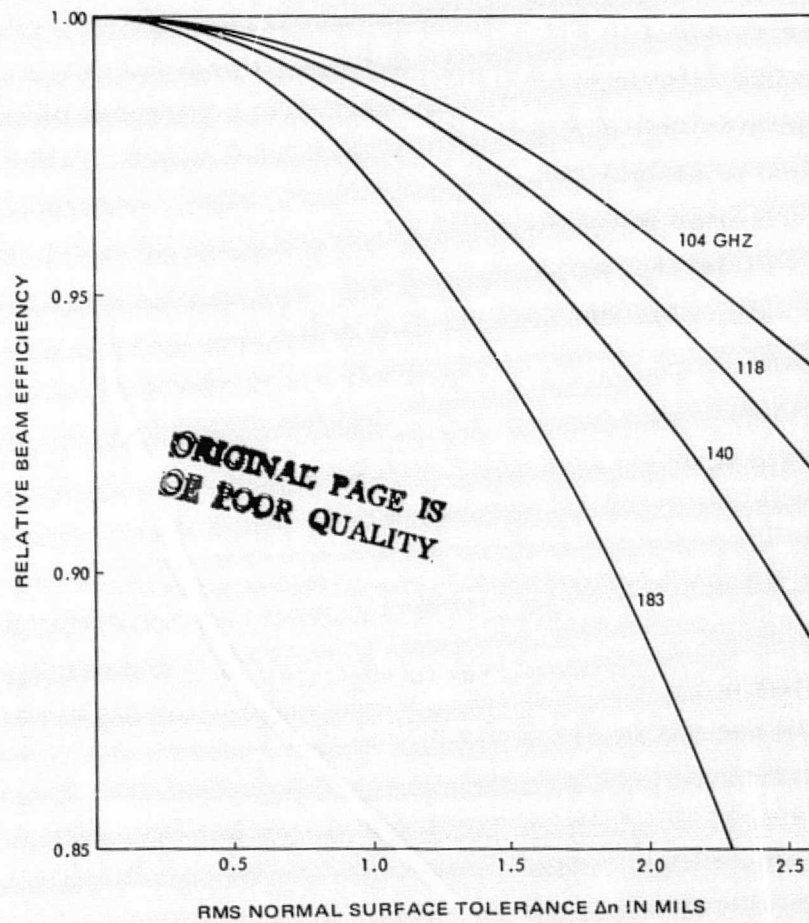


Figure 16. Effects of normal surface tolerance on beam efficiency.

#### 2.4.1.7 Effects of Positional Errors

In addition to the tolerance on the reflective surface, the tolerances of the structural members that support the feed and the subreflector are of extreme importance as well. Displacement of the feed or reflectors along the optical axis will contribute to antenna defocusing with resultant beam broadening and increased sidelobe levels. Of more serious consequence is any lateral displacement of the subreflector that would result from unequal length changes of the struts. Even a slight displacement can result in a significant beam shift. In addition, the orientation of the best fit paraboloidal reflector surface relative to the reference best fit paraboloidal surface must be considered. The effects of various positional errors on the beam pointing direction are summarized in Figure 17. The various values of  $k$  used in calculating allowable deflections and rotations are given in Table VIII.\*

For the baseline antenna, dimensions  $f$  and  $F$  of Figure 17 are 1.70 meter and 1.54 meter, respectively. The magnification,  $M$ , is 24.062. Thus, the expressions for the various pointing errors take the following approximate forms.

$$\begin{aligned}\theta_R &\approx 0.0798 \\ \theta_T &\approx 0.4907h \\ \theta_F &\approx 0.0270 \\ \theta_P &\approx 0.875 \\ \theta_s &\approx 0.568 \quad v\end{aligned}$$

In addition to these errors there will also be an error  $\theta_M$  due to pointing error in the servo system. The total RSS pointing error  $\theta_e$  is then given by:

$$\theta_e = (\theta_M^2 + \theta_R^2 + \theta_T^2 + \theta_F^2 + \theta_P^2 + \theta_s^2)^{1/2} \quad (35)$$

The most stringent requirements come from operation at 183 GHz. At that frequency the half-power beamwidth,  $(H)_{1/2}$ , is, from Table V, 488 radians

---

\*The values were obtained for a different antenna and are taken as illustrative. More precise values would have to be determined in an actual design.

1. HYPERBOLOID ROTATION

$$\theta_R = k_1 \text{TAN}^{-1} \frac{f}{F} \frac{2\beta}{M+1}$$

2. HYPERBOLOID TRANSLATION

$$\theta_T = k_2 \text{TAN}^{-1} \frac{h}{F} \frac{M-1}{M}$$

3. FEED TRANSLATION

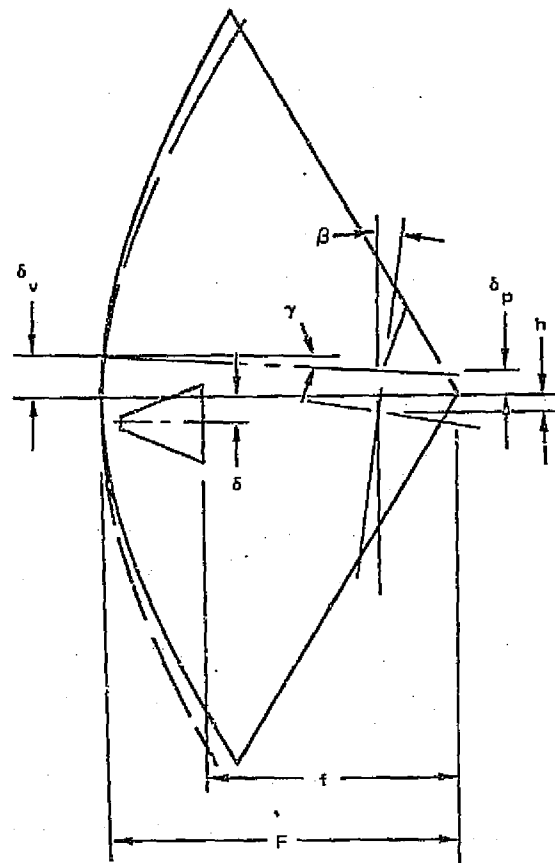
$$\theta_F = k_3 \text{TAN}^{-1} \frac{\delta}{MF}$$

4. PARABOLOID ROTATION

$$\theta_P = K\gamma$$

5. PARABOLOID TRANSLATION (VERTEX SHIFT)

$$\theta_S = K \text{TAN}^{-1} \frac{\delta_v}{F}$$



- $\theta$  = BEAM POINTING ERROR
- $F$  = PARABOLOID FOCAL POINT
- $f$  = HYPERBOLOID FOCAL POINT
- $M$  = MAGNIFICATION FACTOR
- $\beta$  = HYPERBOLOID ROTATION
- $h$  = HYPERBOLOID TRANSLATION
- $\delta$  = FEED TRANSLATION
- $K$  = BEAM DEVIATION FACTOR (PARABOLOID)
- $\gamma$  = PARABOLOID ANGULAR DEVIATION
- $\delta_v$  = BEST FIT PARABOLOID VERTEX TRANSLATION
- $\delta_p$  = BEST FIT PARABOLOID FOCAL POINT SHIFT
- $k_1$  = BEAM DEVIATION FACTOR (HYPERBOLOID ROTATION)
- $k_2$  = BEAM DEVIATION FACTOR (HYPERBOLOID TRANSLATION)
- $k_3$  = BEAM DEVIATION FACTOR (FEED TRANSLATION)

ORIGINAL PAGE IN  
OF POOR QUALITY

Figure 17. Cassegrain antenna beam pointing error analysis.

TABLE VIII. BEAM DEVIATION FACTORS

$k_1$	$k_2$	$k_3$	K
0.908	0.788	1.00	0.875

(0.028 degree). The absolute pointing accuracy should be  $0.3 \text{ (H)}_{1/2} (1\sigma)$ , which is  $146 \mu\text{radians}$ . The error is distributed among the six component errors. If it is assumed that the mechanical rms error is  $90 \mu\text{radians}$  and that the remaining individual rms errors are equal, then each one is allowed a value of  $51 \mu\text{radians}$ . The corresponding allowable rms values of the various rotations and displacements are shown in Table IX.

TABLE IX. ALLOWABLE RMS VALUES OF VARIOUS DISPLACEMENTS AND ROTATIONS IN CASSEGRAIN ANTENNA

$\sigma_\beta$	$\sigma_\gamma$	$\sigma_h$		$\sigma_\delta$		$\sigma_{\delta_v}$	
$\mu\text{rad.}$	$\mu\text{rad.}$	met. x $10^6$	mils.	met. x $10^6$	mils.	met. x $10^6$	mils.
640	59	95	4.1	1890	74.5	90	3.6

The allowable axial displacement of the subreflector with respect to the main reflector focus may be estimated by considering the depth of field of the main reflector. An amplitude distribution of the form  $1/[1 + (\rho/2F)^2]^2$  is assumed in the analysis where  $\rho$  is the radius from the axis to a point in the aperture. The relative power density variation for subreflector displacement about the focus varies approximately as follows.

$$\frac{S}{S_0} = \frac{\sin^2 \left( 2\pi \frac{\Delta z (1 + 1/M)}{\lambda} \frac{(D/4F)^2}{(1 + (D/4F)^2)} \right)}{\left( 2\pi \frac{\Delta z (1 + 1/M)}{\lambda} \frac{(D/4F)^2}{(1 + (D/4F)^2)} \right)^2} \quad (36)$$

where  $\Delta z$  is the axial displacement from the focal point,  $D$  is the diameter of the main reflector,  $F$  is its focal length, and  $\lambda$  is the wavelength. To keep the

beam peak power within 1 percent of its focussed value at 183 GHz,  $\Delta z$  must be less than 5.1 mils.

A similar analysis holds for the axial displacement of the feed, except that  $F$  should be replaced by  $MF$  and the factor  $(1 + 1/M)$  is absent.  $M$ , the magnification, equals 24.062. For this value of  $M$  the axial position of the feed is not critical and should be easily maintained within acceptable values.

## 2.5 RF TESTING

The 4.4 meter antenna system presents two challenging problems; the first one is how to construct the structure to meet the specifications of surface tolerance and beam pointing accuracy in the hostile space environment and the second one is to devise a method of testing the electrical performance of the system before launch. In this section we will address the second problem and we will further assume that the performance in orbit will be predictable once the performance in the terrestrial environment has been established. Thus, in this discussion, it will be postulated that gravity effects and thermal loads will not be significant or that means have been devised to account for them if they are.

There are three characteristics of significance to the system performance a) beam efficiency, b) sidelobe structure, and c) pointing fidelity. The first one concerns the resolution of the radiometric system. The second one must be known in order to predict the interaction between the antenna and sources of thermal radiation that may enter the sidelobe and backlobe region of the antenna. The most important characteristic, beam efficiency, will be taken up. Beam efficiency is the power radiated over the main beam of the antenna divided by the total power radiated by the antenna\* or

$$\eta_B = \frac{\int_{\Omega_0} P(\Omega) d\Omega}{\int_{4\pi} P(\Omega) d\Omega} \quad (37)$$

---

\*There are refinements of the terms beam efficiency, such as weighted beam efficiency, and beam efficiency of the wanted polarization. These terms may be used with the measurement techniques but do not affect them appreciably.

where  $P(\Omega)$  is the gain as a function of the solid angle  $\Omega$ ,  $\Omega_0$  is the angular region within which the beam efficiency is evaluated. Note that the resistive losses do not enter into the beam efficiency. The equation may be manipulated into alternate forms so as to obtain equivalent expressions. The directivity is given by\*

$$D_m = \frac{4\pi}{\int_{4\pi} P(\Omega) d\Omega} \quad (38)$$

$$\text{Max gain } G_m = \eta D_m \quad (39)$$

where  $\eta$  represent the antenna losses

We can use these equations to obtain the following expression.

$$\eta_B = \frac{G_m}{4\pi\eta} \int_{\Omega_0} P(\Omega) d\Omega \quad (40)$$

## 2.5.1 Available Techniques

### 2.5.1.1 Far Field Measurements

The gain may be obtained by an integration of the power into the feed horn illuminating the reflector: the integration can be performed over a sphere that encloses the feed horn. The losses are taken into account by obtaining the reflectivity of the surface of the reflector. The term  $\int_{\Omega_0} P(\Omega) d\Omega$  is obtained by taking sufficient patterns over the main beam so that the integration can be carried out with sufficient accuracy. The determination of the patterns and the gain will be discussed next.

---

\*W. V. T. Rusch and P. D. Potter, Analysis of Reflector Antennas, Academic Press, New York City 1970; p 61.

### Gain and Patterns

In order to accomplish the measurements of gain and patterns of the test antenna the antenna must be in the far field of the source antenna. Table X lists these parameters for several selected frequencies.

TABLE X. FAR-FIELD DISTANCES FOR  
4.4 METER PARABOLOID

Frequency GHz	3 dB Beamwidth in Degrees	Far-Field Distance km.		Zenith Attenuation dB
		$2 D^2/\lambda$	$D^2/\lambda$	
94	$5.19 \times 10^{-2}$	12.13	6.06	1
140	$3.49 \times 10^{-2}$	18.07	9.03	2
210	$2.33 \times 10^{-2}$	27.10	13.55	3

These frequencies were selected to minimize path loss due to atmospheric attenuation. The numbers given for zenith attenuation also give a relative attenuation for line of sight terrestrial losses.

The pattern measurements using a horizontal path suffer from three problems, namely multipath, path attenuation and scintillations. The attenuation will affect sensitivity but will not affect the patterns if it does not change during the time of measurement.

An attempt to evaluate beam efficiency using Eq. (37) directly would mean an integration over all sidelobes. The wavelength is so small and the antenna so large that the number of sidelobes is immense in two-dimensional space. Thus the second method using Eq. (40) must be used. The extent of the measurement is small since the length equivalent to the 3 dB beamwidth is only about  $2.5D$  at  $2D^2/\lambda$ . Thus the null-to-null extent would be less than  $10D$  or about 40 meters. The antenna could be stationary and an X-Y traverse system could be used to record the patterns over the main beam. The multipath can be minimized by locating the test range on a suitable horizontal site such as the Grand Canyon in Arizona. Another possibility is to use a nearly vertical path to a source antenna located in geostationary orbit or a radio star. A ground location at high altitude would reduce



atmospheric attenuation as well. An antenna range in orbit is being considered for the shuttle flights. Radio stars have been calibrated up to 100 GHz. Calibration at the frequencies needed here would have to be available.

The scintillations are due to the changes in the dielectric constant of the atmosphere. These scintillations increase in amplitude and rate as a function of frequency. At 40 GHz the excursions are around 1 dB with a rate of several zero crossings per second. The rate depends on the cross-wind velocity. The problem can be minimized by a proper choice of the place and time of measurement and by an integration of the received signal so as to smooth out the fluctuations. A vertical path would again minimize the problem.

The gain measurements fall into two categories: the absolute gain measurement and the gain transfer method.\* For the absolute method no a priori knowledge of the gains of any antenna is required. However, the Friis transmission formulas are assumed to be valid. These formulas are not valid at these frequencies for a terrestrial measurement because of atmospheric attenuation. The gain transfer method can be used with a calibrated low gain horn. Several succeeding larger aperture antennas may have to be used to transfer the gain within the limits of the attenuation standards. The scintillation rates are aperture dependent; a smaller aperture will integrate the fluctuations over a larger common volume of space since the antenna has a larger acceptance angle.

#### 2.5.1.2 Near-Field Measurements

The problem of atmospheric attenuation, scintillations and multipath can be circumvented by probing the near field. Since the transformation from the near-field to the far-field is a mathematical one, the near-field

---

\*The techniques and others taken up here are detailed by W.H. Kummer and E.S. Gillespie "Antenna Measurements - 1978" to appear in IEEE Proc. April 1978. A comprehensive discussion is also given in Antenna Test Procedures IEEE STD 149-1978 to be published.

measurement will give the beam efficiency. For the transformation to be made both amplitude and phase must be recorded; the characteristics of the probe antenna and its coupling to the test antenna must be known and accounted for. These problems have been studied in great detail and are state-of-the-art for planar probing measurements. This technique may well become the most accurate method for the measurement of power gain and patterns for antennas that can be accommodated by the measuring apparatus.

The present development indicates a probe position accuracy of about  $10^{-4}$  meters; an important consideration since the measurements are distance dependent. For very accurate measurements a  $0.01\lambda$  positional accuracy is desired. This would mean an improvement of over one order of magnitude over existing facilities.\* The total number of data points, spaced one wavelength apart would be  $8 \times 10^6$ . The CPU time on a CDC6600 would be about 5.23 hours to complete the data reduction for one two dimensional scan.

Further investigation is needed to determine the possibility of expanding the existing facility to handle size, frequency, and required accuracy.

Note that the complete field must be probed even if only the peak gain and main beam pattern are wanted.

### 2.5.1.3 Indirect Methods

It is also possible to measure the actual surface of the reflectors, the feed horn pattern and the surface losses. Knowing these factors the beam efficiency can also be obtained.

Photogrammetric techniques can be used to obtain accuracies of  $1/20,000$  to  $1/100,000$  of the diameter of the reflector or  $4.4 \times 10^{-2}$  mm. at best for this size antenna. This method utilizes two or more long focal-length cameras that take overlapping photographs of the surface to be measured. The surface is uniformly covered with self-adhesive photographic targets whose images appear on the photographic record. A least squares triangulation process is used in which two dimensional measurements of the images of the targets are processed simultaneously to generate a unique set of three dimensional coordinates for each discrete target.

---

\* A. C. Newell and M. L. Crawford, "Planar Near-Field Measurements on High Performance Array Antennas," Nat. Bur. Stand., Rep. NBSIR 74-380 (1974).

For large reflector antennas operating at millimeter wavelengths the photogrammetric technique may not be sufficiently accurate to predict adequately the antenna's performance. Another method that can be used is that of precise distance measurements. As an example of the accuracy demanded of such distance measurements, a 65 meter antenna designed to operate at a wavelength of 3.5 mm requires over 3000 points on the surface to be set to an accuracy of  $\pm 0.1$  mm. This accuracy may be achieved by distance measurements from two fixed points, such as the focus and vertex of the parabolic reflector. These measurements, over ranges from a few meters up to about 60 meters must be made rapidly, preferably using an automated system. A modulated laser beam is used for this purpose.\* The surface of the reflector is covered with targets (small optical corner cubes). The laser beam is directed to the targets by means of programmable mirrors. The entire measurement procedure can be controlled by a small digital computer. The phase of the returned signal is measured with respect to a reference. The phase shift is proportional to the total distance traversed. If the distance and modulation frequency are such that the phase is shifted more than one cycle, an ambiguity will occur. This can be resolved by a crude knowledge of the distance or by using a dual-frequency system. An accuracy of  $\pm 0.08$  mm at distances up to 60 meters has been achieved using this technique.

### 2.5.2 Relative Merits of Techniques

The previous sections have discussed the various possible techniques that could be used in the determination of beam efficiency. An in depth study is needed to give a definitive answer as to best technique and accuracy. This becomes evident when one notes that there are no gain standards, noise standards, radio star flux densities, attenuation standards, antenna pattern receivers, pattern range transmitters, near-field ranges, or instrumentation available at 193 GHz.

Table XI lists the techniques assuming that standard test equipment were available.

---

\*J. M. Payne, "An Optical Distance Measuring Instrument," Rev. Sci. Instrum., vol. 44, pp. 304-306, Mar. 1973.

TABLE XI. SUMMARY OF MEASUREMENT TECHNIQUES

Measurement Method	Gain	Patterns	Accuracy	Problem	Cost
Gain Comparison Main Beam Pattern (Terrestrial)	Yes	Yes	Depends on location	Multi path scintillations	Medium
Gain Comparison Main Beam Pattern (Earth-Space)	Yes	Yes	Depends on location	No space plat- form available, no radio star flux data	Medium assume plat- form available at no cost
Near-Field	Yes	Yes*	Excellent	Specialized equipment not available	Expensive for facilities and data reduction
Indirect-Photogrammetric	No	No	Marginal	Best accuracy of technique equal to surface tolerance required	Low
Indirect-Precise Distance Measurement	No	No	Excellent	None	Medium

\*Probing must be performed over full aperture.

## 2.6 MECHANICAL DESIGN STUDIES

Subsequent to the selection of the Cassegrain configuration as the preferred antenna type, General Dynamics Convair performed a preliminary mechanical and thermal design study followed by a baseline design study. These studies are reported in the following sections.

### 2.6.1 Preliminary Design Study

#### Preliminary Design Study Plan

With selection of the symmetrical Cassegrain design, the following approach was implemented to develop an initial design concept that could be defined in sufficient detail to facilitate a cost study for the complete antenna system:

1. Assess in-house experience
  - 8-foot technology antenna program
  - 12-foot symmetrical Cassegrain antenna study
2. Conceive various structural arrangements and prepare a preliminary design mount.

#### 2.6.1.1 8-Foot Technology Antenna

Convair has used the technology developed in more than \$10 million worth of similar composite experience as typified by the eight-foot technology antenna shown in Figure 18. Surface tolerances achieved from the mold were three mils, while after adjustment they were 2.5 mils. Operational tolerances were 3.1 mils, as measured on a profilometer. The extensive qualification testing (Figure 19) done on that antenna gives Convair confidence that the design philosophy selected for the MASR reflector is one that will ensure success.

The basic reflector design approach is essentially being used herein as a preliminary design for the 4.4 meter antenna. A part and weight breakdown for this reflector is given in Table XII and will be used later to project the weight of a 4.4 meter reflector.

ORIGINAL PAGE IS  
OF POOR QUALITY

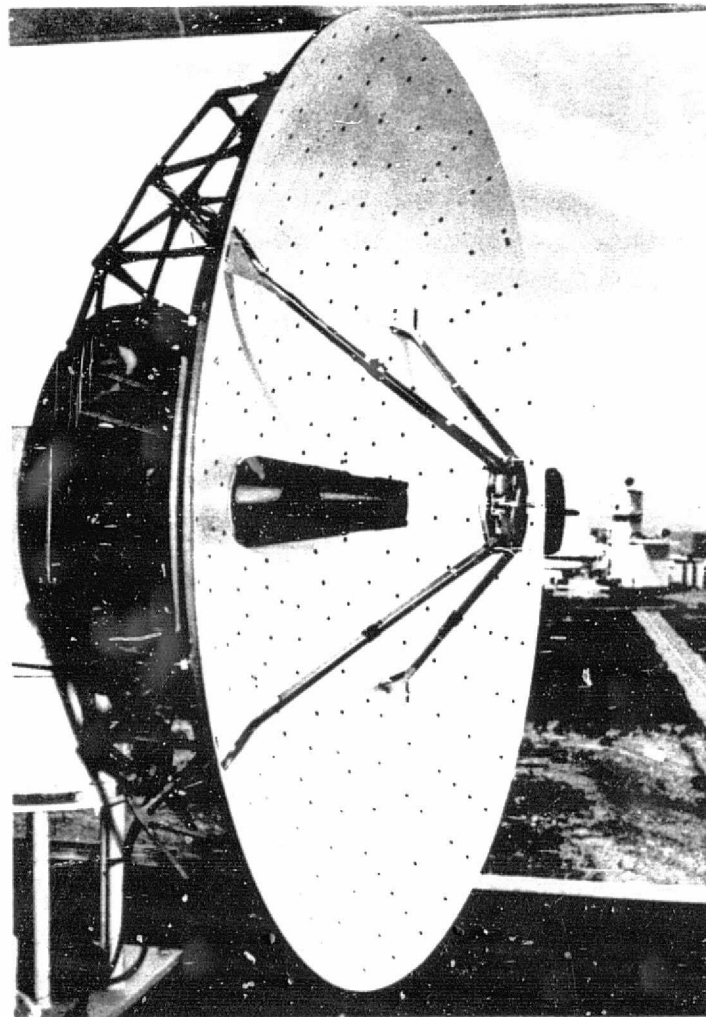


Figure 18. Convair 8-foot-diameter graphite epoxy Cassegrainian antenna on pattern range.

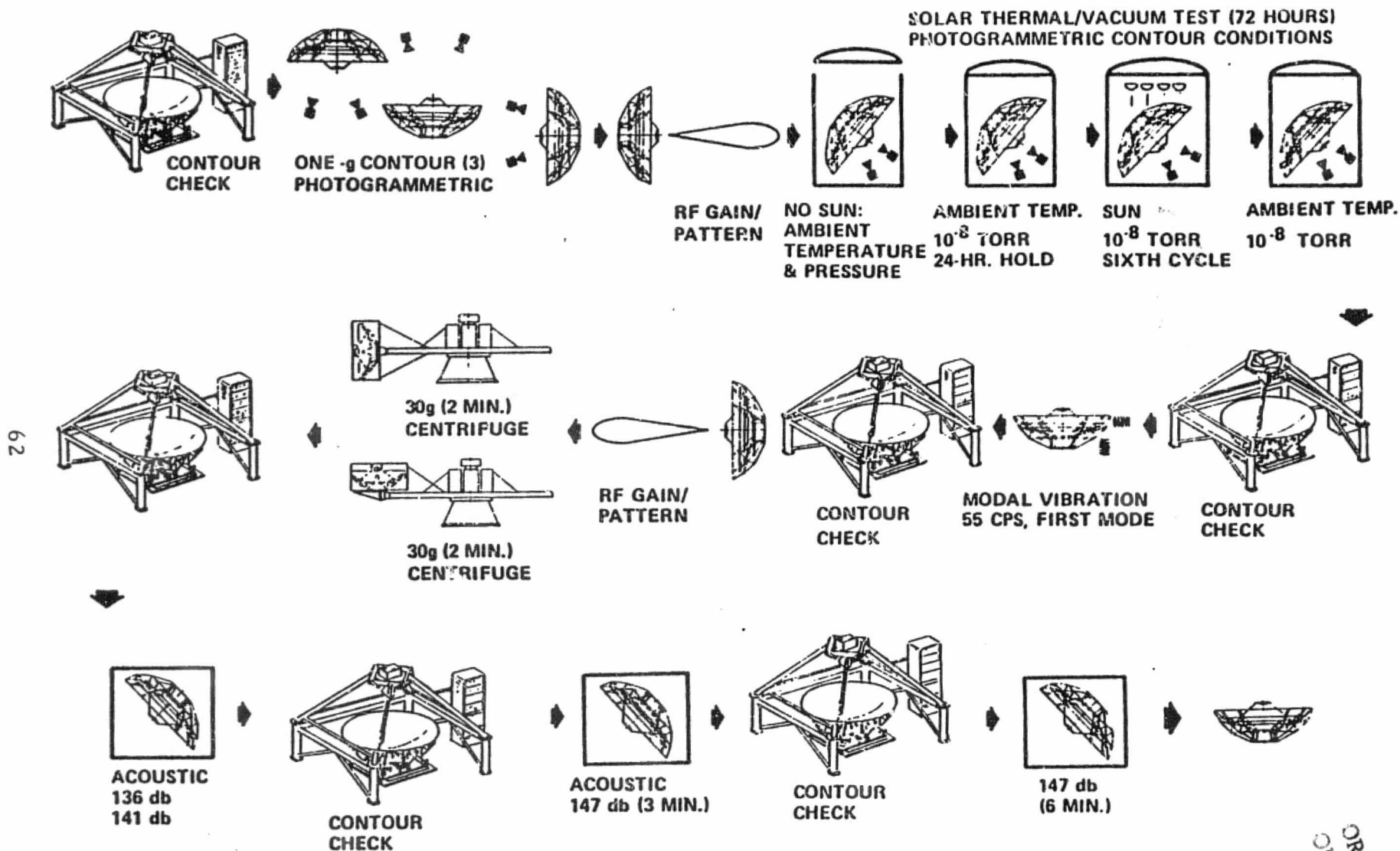


Figure 19. Test program successfully completed on Convair 8-foot-diameter graphite antenna.

ORIGINAL PAGE IS  
OF POOR QUALITY

ORIGINAL PAGE IS  
OF POOR QUALITY

TABLE XII. TECHNOLOGY ANTENNA MASS PROPERTIES

MASS PROPERTIES SUMMARY			MIPI COMPUTER PROGRAM ANALYSIS								
PROJECT= 8-FT. DIA. COMPOSITE PROTOTYPE ANTENNA			DATE=07/12/71								
ITEM	WEIGHT LBS *	XCG INCH	YCG INCH	ZCG INCH	IXX SLUG-FEET SQUARED	IYY SLUG-FEET SQUARED	IZZ SLUG-FEET SQUARED	IXY SLUG-FEET SQUARED	IXZ SLUG-FEET SQUARED	IYZ SLUG-FEET SQUARED	
REFLECTOR + GUSSETS	32.69A	0.0	0.0	9.3	2.705	2.705	7.357	.000	.000	.000	
REFLECTOR RIBS											
RIB NO. 1	.92A	0.0	35.0	3.6	.025	.009	.016	.000	.000	.011	
RIB NO. 2	.92A	-17.4	30.3	3.6	.022	.013	.016	-.006	-.005	.009	
RIB NO. 3	.92A	-30.3	17.4	3.6	.013	.022	.016	-.006	-.009	.005	
RIB NO. 4	.92A	-35.0	0.0	3.6	.009	.025	.016	.000	-.011	.000	
RIB NO. 5	.92A	-30.3	-17.4	3.6	.013	.022	.016	.006	-.009	-.005	
RIB NO. 6	.92A	-17.4	-30.3	3.6	.022	.013	.016	.006	-.005	-.009	
RIB NO. 7	.92A	0.0	-35.0	3.6	.025	.009	.016	.000	.000	-.011	
RIB NO. 8	.92A	17.4	-30.3	3.6	.022	.013	.016	-.006	.005	-.009	
RIB NO. 9	.92A	30.3	-17.4	3.6	.013	.022	.016	-.006	.009	-.005	
RIB NO. 10	.92A	35.0	0.0	3.6	.009	.025	.016	.000	.011	.000	
RIB NO. 11	.92A	30.3	17.4	3.6	.013	.022	.016	.006	.009	.005	
RIB NO. 12	.92A	17.4	30.3	3.6	.022	.013	.016	.006	.005	.009	
RIB CTR DIAGONALS	2.51A	0.0	0.0	3.6	.034	.034	.059	.000	.000	.000	
INTERIB DIAGONALS	2.61A	0.0	0.0	4.0	.028	.028	.056	.000	.000	.000	
RIB FASTENERS	.50A	0.0	0.0	3.6	.054	.054	.107	.000	.000	.000	
RIB ADHESIVE	.50A	0.0	0.0	3.6	.054	.054	.107	.000	.000	.000	
TOTAL-REFLECTR RIBS	17.16	0.0	0.0	1.0	1.654	1.655	3.446	.000	.000	.000	
PALLET ASSEMBLY											
PALLET RING	3.70A	0.0	0.0	-10.3	.162	.162	.325	.000	.000	.000	
LINKS	.41A	0.0	0.0	-10.3	.013	.013	.026	.000	.000	.000	
FITTINGS	.88A	0.0	0.3	-10.3	.039	.037	.076	.000	.000	.000	
HARDWARE	.46A	0.0	0.0	-10.3	.020	.020	.040	.000	.000	.000	
TOTAL-PALLET ASSY	5.45	0.0	0.0	-10.3	.239	.238	.477	.000	.000	.000	
SUBREFLECTOR ASSY											
SUBREFLECTOR	1.93A	0.0	0.0	27.0	.003	.003	.005	.000	.000	.000	
SUBREFLECTOR SUPTS	.99A	0.0	0.0	29.0	.002	.002	.003	.000	.000	.000	
STRUTS	.64A	0.0	0.0	19.5	.031	.031	.053	.000	.000	.000	
GUSSETS	.63A	0.0	0.0	9.2	.067	.067	.136	.000	.000	.000	
TOT-SUBREFLECTR ASY	4.19	0.0	0.0	23.7	.144	.144	.198	.000	.000	.000	
FEEDCONE ASSEMBLY											
FEED CONE	2.41A	0.0	0.0	5.6	.017	.017	.008	.000	.000	.000	
MICROMETERS	1.24A	0.0	0.0	2.0	.005	.005	.003	.000	.000	.000	
TRUSS FITTINGS	.64A	0.0	0.0	2.2	.001	.001	.001	.000	.000	.000	
TOTAL-FEEDCONE ASSY	4.89	0.0	0.0	2.3	.035	.035	.017	.000	.000	.000	



### 2.6.1.2 12-Foot Antenna Study

The following section is presented as a summary of the 12-foot antenna design study.

#### Structural Design

The structure of the 12-foot diameter, shaped Cassegrain, antenna is illustrated in Figures 20 and 21. The main reflector design is based on an  $f/D$  ratio of 0.3. The reflector shell is ring stiffened and supported by twelve, equally spaced, truss ribs that radiate outward from a central torque box. An aluminum alloy subreflector, 15 inches in diameter, is located 41.8 inches above the main reflector vertex. The subreflector is supported from the main reflector structure by four, equally spaced struts. A Kapton tent is installed over the back of the antenna to provide a thermodynamic shield for the structure. The tent extends from the rim of the main reflector to the center torque box. Three, equally spaced, interface fittings are installed at the outer web of the torque box. The overall depth of the antenna from the top

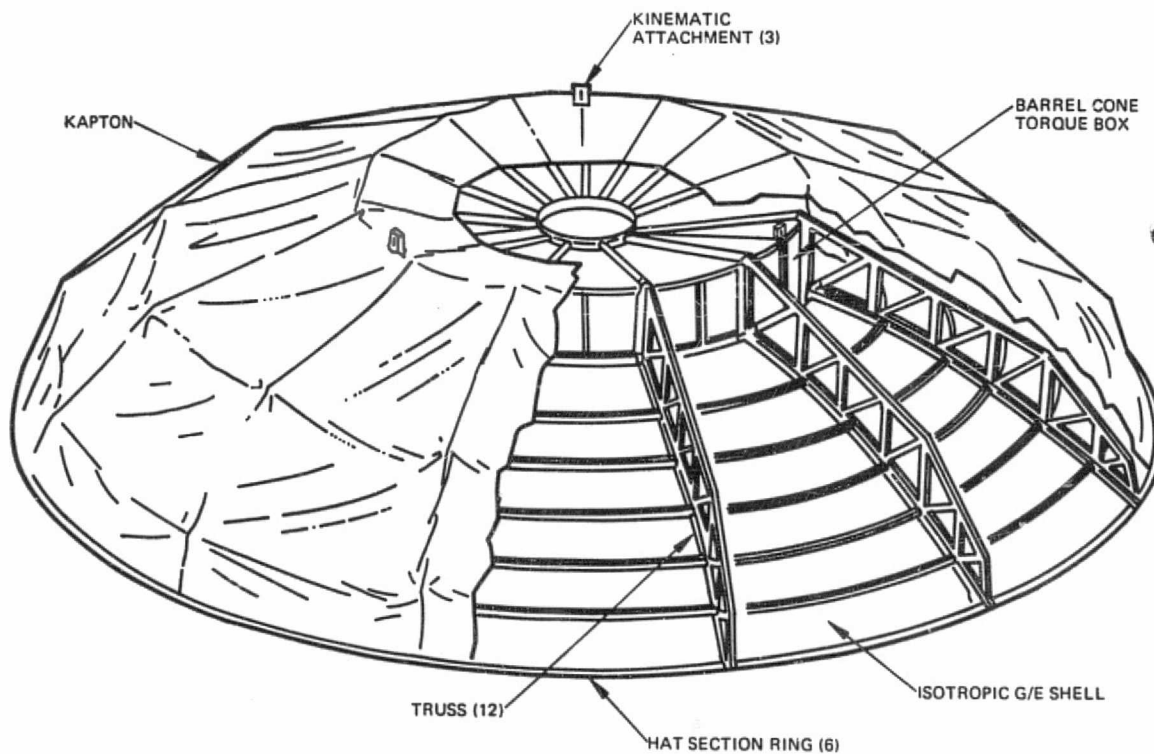


Figure 20. Twelve-foot diameter graphite Cassegrain antenna.

ORIGINAL PAGE IS  
OF POOR QUALITY

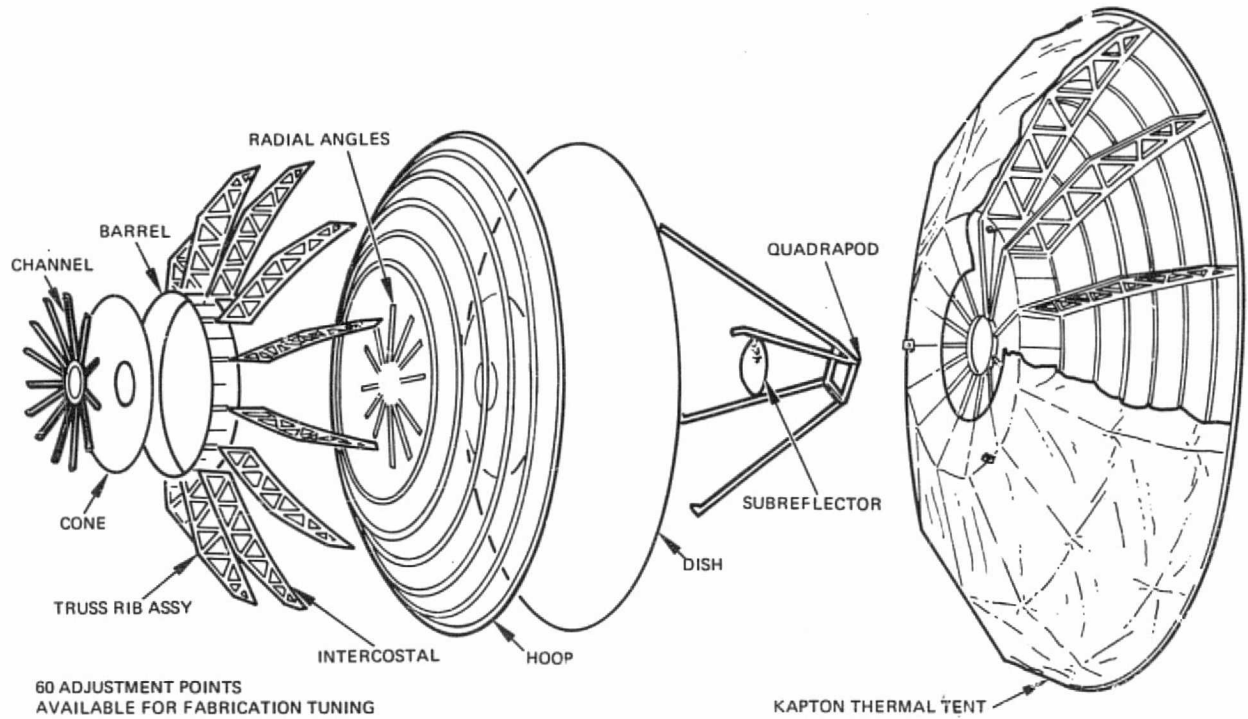


Figure 21. Twelve-foot diameter graphite Cassegrain antenna.

TABLE XIII. 12-FOOT CASSEGRAIN ANTENNA WEIGHT SUMMARY

Item	Weight, pounds
Reflector	(41.5)
Dish	39.1
Coating	1.1
Joint, Splice and Fasteners	1.3
Stiffeners	-
Ribs and Backup Structure	(32.6)
Hoops	11.5
Feed Support	0.1
Ribs	21.0
Longerons (Cross Beams)	-
Torque Box	(12.4)
Barrel Assembly	6.3
Cone Assembly	6.1
Subreflector Assembly	( 6.2)
Subreflector	1.5
Support Tubes	2.3
Gussets	0.8
Mounting and Adjustment	1.6
Thermo Tent	( 5.5)
Interface Fitting	( 1.9)
Adhesive	( 5.0)
TOTAL	105.1

of the subreflector structure to the interface attachment plane is 50 inches. All enclosed areas, such as the torque box structure and the shell stiffening rings, are vented. A weight breakdown of the various components that make up this reflector are shown in Table XIII.

#### Reflector Shell Design

The main reflector shell is a pseudoisotropic structure composed of a six-ply layup of GY-70/X-30\* graphite/epoxy material. As shown in

\*See Appendix B for Material Selection Criteria.

Figure 20, the rear surface of the shell is reinforced with six, concentric, hat section stiffening rings, fabricated from quasi-isotropic GY-70/X-30 graphite. A series of radial angles is installed adjacent to the shell vertex and within the confines of the torque box structure as shown in Figure 21. The angles are aligned with each rib and constitute an inboard extension of the rib upper chord member. The shell is radially slotted at four, equally spaced, locations to allow rib tangs to pass through the reflector and attach to the subreflector support struts. A 10-inch diameter hole, centered about the reflector vertex, has been cut to accommodate the antenna feed assembly.

#### Torque Box Design

The torque box is centered about the shell vertex and is bonded to the rear surface of the reflector. It is composed of two elements, a cylindrical barrel and a conical shell which, when assembled to the reflector, form a triangular body of revolution. The cylindrical barrel forms a "Z" in cross-section. The cone has an included angle of approximately six degrees, extends inboard from the lower flange of the barrel to pick up the shell about 5 inches from its vertex. Twelve radial channels, aligned with the rib center lines, are bonded to the concave surface of the cone shell. The channels stiffen the cone surface and also serve to react and distribute the feed cone and rib lower chord loads into the torque box.

Three interface fittings, located between ribs and spaced at 120 degrees, are mounted to the barrel web. These fittings are designed to minimize induced bending of the antenna structure resulting from launch loads or differential expansion between the antenna and its support structure.

#### Rib Design

Outboard of the torque box, the reflector is supported by twelve, equally spaced, truss ribs. There are two rib configurations; eight of a basic design, plus four variants. The variant ribs are identical to the basic design, in all respects, except for a tang-like extension on the upper chord

which, on final assembly, projects through the reflector shell to pick up the subreflector struts. At its inboard end the vertical load components of each rib are transferred to the torque box web by shear clips while the lower chord axial loads are spliced by gussets that pass under the barrel to attach to the cone channels. The upper chord is spliced through the torque box web to the inboard shell mounted angles by Hi-Loc fasteners.

The reflector contour may be adjusted at any of the seventy-two intersection points of the ribs with the shell stiffening rings. A typical such point is shown in Figure 22. The adjustment may be carried out by adjustment of the micrometers and performance of a contour check on the profilometer any time after the shell and ribs have been bonded to the torque box but before the final bonding of the ribs to the shell.

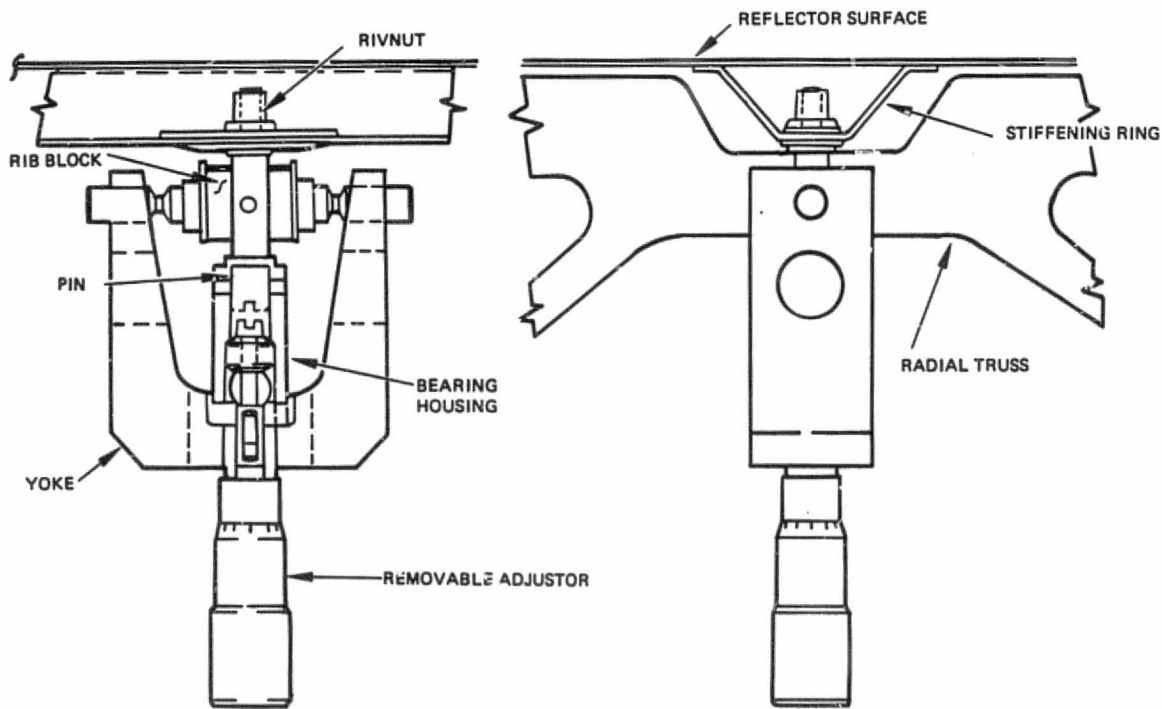


Figure 22. Shell adjustor (used during fabrication and removed after lockout).

### Subreflector Design

The subreflector is machined from an aluminum alloy casting (Tenzaloy) that, after heat treatment and air cooling, is stress free and dimensionally

stable. The subreflector is a hyperbolic body of revolution, of constant thickness that is mounted to a graphite/epoxy frame. The frame, in turn, is supported from the main reflector substructure by four tubular struts of rectangular cross-section. The struts are positioned at 90 degrees with respect to each other and with the wider strut dimension oriented in the radial direction.

#### Tent Design

A Kapton tent is installed over the back of the antenna to provide a thermodynamic shield for the structure. The tent is fabricated from twelve, wedge-shaped, gores that span the distance between adjacent ribs and are shaped to follow the rib contours. The individual gores are attached to the antenna structure at their inboard and outboard edges only. The inboard attachment consists of a small spring that joins the gore to the cone structure at its outboard edge; each gore is periodically tied to the outer ring of the main reflector. The tent does not contact the ribs but is suspended over them by periodic, rib mounted, standoffs. Adjacent gores are fastened together at each standoff and between these points simply overlap each other. The inboard spring at each gore allows the tent to expand and contract in a radial direction as the thermal environment varies with position in orbit.

#### Weight

Weight projection for a 4.4 meter symmetrical cassegrain reflector was made utilizing information from Table XII which contains actual weights for the 8-foot reflector and Table XIII which contains calculated weights from a preliminary designed and analyzed 12-foot reflector. Comparison of the weights of all three antennas is made in Table XIV.

As an independent check on weight prediction, a plot of the 8 foot and 12 foot antenna weights was made (see above). The projected weight for a 4.4 meter reflector would be between 120 and 130 pounds depending on the degree of nonlinearity and linearity in these plotted curves. It should be noted that no consideration has been made for fabrication of the basic reflector skin in segments and subsequent splicing. Because this may be

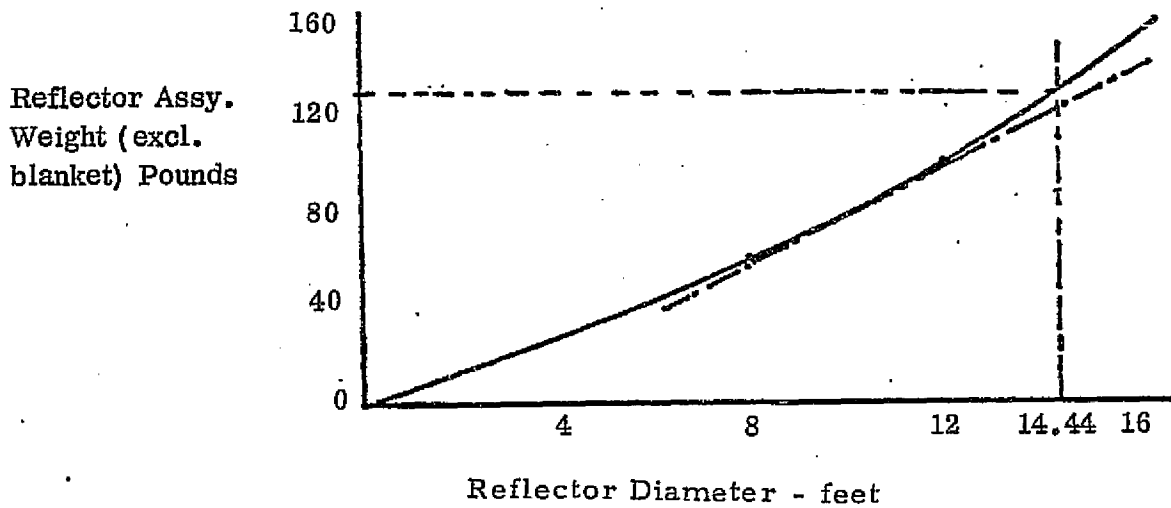
TABLE XIV. MASS PROPERTY COMPARISON

Sym. Cassegrain Antenna (excluding antenna support)

Component	8-Foot* (2.44M)	12-Foot** (3.66M)	14.44 Foot (4.40M)
Reflector Skin	32.69	41.5	51
Reflector Ribs	17.16	32.6	44
Pallet Assy.	5.45	--	--
Torque Box	--	12.4	16
Subreflector Assembly	4.19	6.2	8
Blanketing	--	5.5	8
Adhesive (incl'd. for 8-ft.)	--	5.0	6
<b>TOTAL</b>	<b>59.49</b>	<b>103.2</b>	<b>133</b>

\*Actual measurements

\*\*Based on preliminary design and analysis calculated weight



required for the 4.4 meter reflector, an additional weight increase is expected on the order of 3 to 6 pounds. Table XV compares the previously budgeted 4.4 meter antenna weight with the new calculated weight.

TABLE XV. WEIGHT SUMMARY

Elements	Budget	Estimated
a) Reflector Skin	52	51
b) Reflector Ribs	52	44
c) Torque Box		16
d) Subreflector Assembly	6	8
f) Blanketing	--	8
g) Adhesive	--	6
<u>Total Reflector Assembly</u>	110	133
Antenna Support	40	51
Feed and Radiometer	50	50
Gimbal Mech.	50	50
Gimbal Attachment Mount	--	16
<u>TOTAL (lb)</u>	250	300

Thermal Distortion

A 12- to 15-foot diameter millimeter wave antenna design can employ the same thermal design features as our 8-foot technology antenna, which has been developed, tested and qualified for space application. A large aperture thermal configuration is shown in Figure 23.

By using graphite/epoxy composites with their low thermal expansion coefficient, wide temperature excursions and gradients can be tolerated and passive thermal control methods can be used resulting in low weight and high reliability. The main reflector, subreflector and subreflector support leg exposed surfaces are coated with our  $\text{SiO}_x/\text{Al}$  coating that has high RF



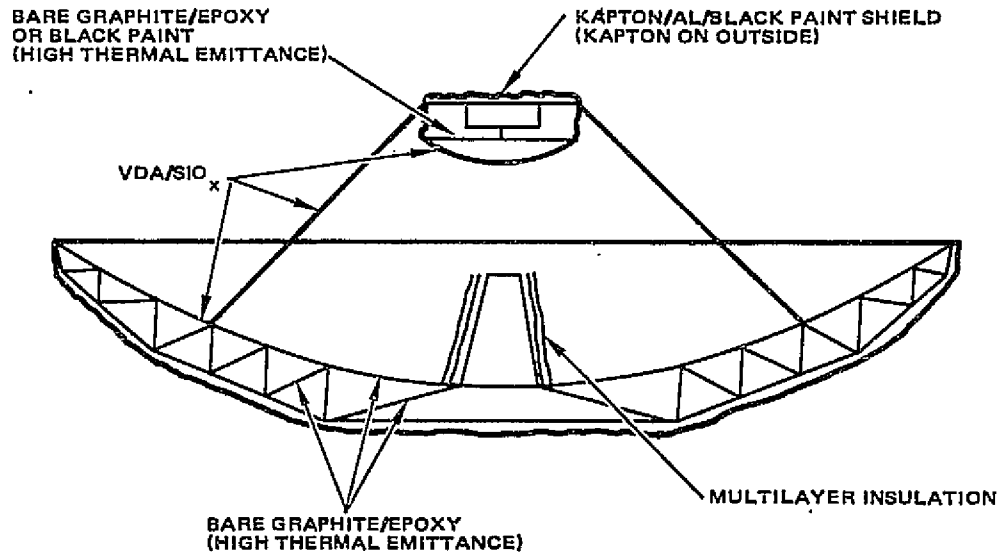


Figure 23. Large aperture antenna thermal design.

reflectance, provides a reasonable operating temperature range, and by proper substrate preparation, yields a surface on the main reflector with a low specularity with respect to solar energy. The main reflector and subreflector backup structures are enclosed with 2 mil Kapton/Al/black paint shields reinforced with fiberglass scrim as shown. The structure and surfaces within the shields are left bare or painted black to enhance radiation heat transfer.

To achieve low subreflector thermal distortion, a material with a high thermal conductivity and/or a low thermal expansion coefficient must be employed. Aluminum with its high thermal conductivity is used on our center mounted 10-inch subreflector (8-foot antenna) and is considered here for the 15-inch subreflector on the 12-foot antenna.

Antennas with 12- to 15-foot diameters may use a design approach similar to the 8-foot antenna hardware, thus a scaled version of the detailed 8-foot antenna mathematical thermal model was employed to obtain preliminary temperature distributions for distortion analyses. One of the worst thermal conditions with respect to RF performance losses results from the sun-on-side orientation in synchronous orbit. Although this case may not be the worst possible case, severe thermal gradients occur and it is a convenient case to use for preliminary analyses.

The sun-on-side temperature distributions obtained for the 12-foot main reflector and its 15-inch aluminum subreflector are presented here (see Figure 24). The temperature differences between hot and cold edges are 295F and 15F for the main reflector and subreflector respectively. The gradient across the 12-foot antenna is only about 10F higher than that for the 8-foot antenna under similar circumstances indicating that for these antenna configurations with thin reflector surfaces in the sun-on-side condition, the dominant mode of heat transfer is via radiation. The gradient across the 15-inch subreflector is about 5F higher than that for the same thickness 10-inch aluminum subreflector (on the 8-foot antenna) under similar circumstances indicating thermal conduction is the dominant mode of heat transfer. The maximum RMS surface error is 0.00013 inch for the sun-on-side condition using GY-70/X-30 graphite composite material.

#### Structural Analysis

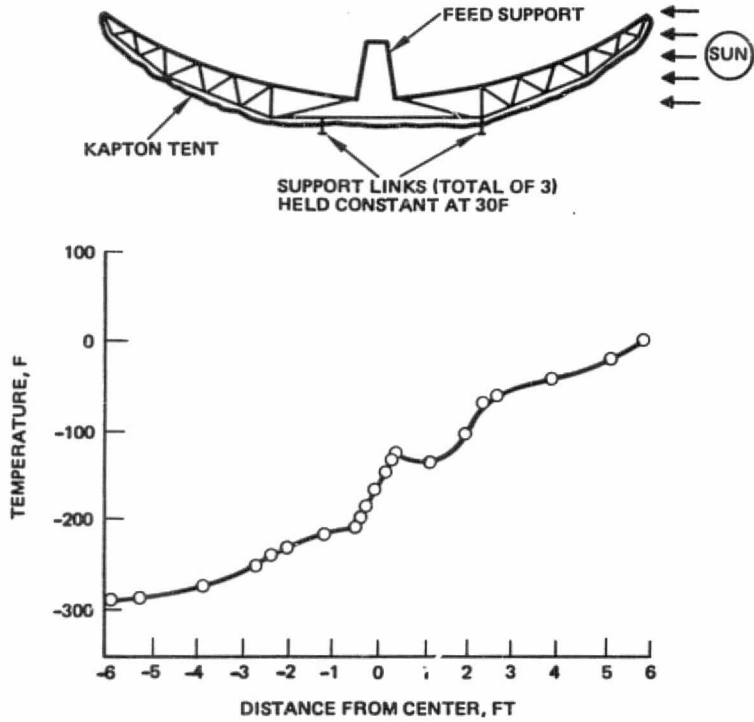
The results of a structural analysis of a 12-foot Cassegrain configuration are listed in Figure 25.

Material. The antenna is constructed from a graphite/epoxy with a very high stiffness to density ratio,  $E/\rho$ , and a very low coefficient of thermal expansion  $\alpha$ .

Finite Element Models. Two models were made to permit analysis of the structural elements. The internal loads obtained from this model were used in the stress and margin safety analysis. The deflections of the surface grids obtained from the model were used in the distortion analysis of the reflector surface. In addition, the model was used for the structural dynamics analysis.

Applied Loads. Space Shuttle launch only was considered. The stowed antenna +Z axis lies normal to the vehicle longitudinal axis and points upward on the vehicle for launch. For on-orbit operation, the deployed antenna was analyzed for sun-on-side thermal conditions.

MAIN REFLECTOR TEMPERATURE DISTRIBUTION ALONG LINE OF SYMMETRY



SUBREFLECTOR TEMPERATURE DISTRIBUTION ALONG CENTERLINE FOR SIDE-ON-SUN CONDITION 15.0-INCH DIAMETER ALUMINUM SUBREFLECTOR FOR 12.0-FOOT DIAMETER RIGID ANTENNA

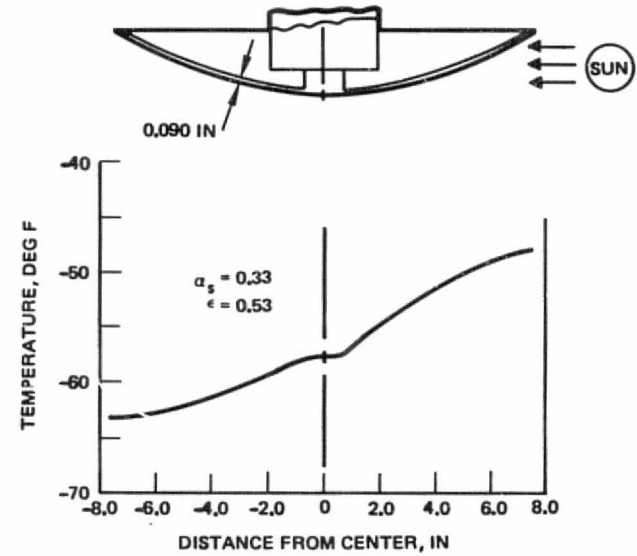


Figure 24. 12-foot antenna/15-inch subreflector temperature predictions.

ORIGINAL PAGE IS OF POOR QUALITY.

ORIGINAL PAGE IS  
OF POOR QUALITY

- MATERIAL GY-70/X-30 GRAPHITE/EPOXY
  - E = 14.68 MSI (AXIAL MODULUS)
  - $\alpha$  =  $-0.027 \times 10^{-6}$  IN./IN./F (COEFFICIENT OF EXPANSION)
  - $\rho$  = 0.063 LB/IN.<sup>3</sup> (DENSITY)
  - F<sub>TU</sub> = 22.07 KSI (ULT TENSILE STRENGTH)
  - F<sub>CU</sub> = 28.33 KSI (ULT COMPRESSION STR)
- STRUCTURAL CONFIGURATION
  - MIN GAGE THROUGHOUT (0.030 IN)
  - STIFFENED PARABOLOID SHELL
    - / 6 CONCENTRIC HAT SECTION RINGS
    - / 12 RADIAL TRUSS RIBS
    - / CENTER TORQUE BOX
- MATHEMATICAL MODEL
  - FINITE ELEMENT METHOD
  - MID-PLANE SYMMETRIC MODEL
    - / 192-NODES AND 421 ELEMENTS
- APPLIED LOADS
  - TITAN IIIC OR SHUTTLE LAUNCH
  - ON-ORBIT CONDITIONS
    - / WORST THERMAL CASE
    - SUN-ON-SIDE, 0.00013 IN. RMS
    - / SLEWING, 0.1G, 0.00011 IN. RMS
- STRESSES AND MARGINS OF SAFETY
  - CRITICAL FOR SHUTTLE CRASH
  - MAX TENSION STRESS, 4700 PSI
  - MAX COMPRESSION STRESS, 3431 PSI
  - MIN M S = +0.01 FOR SHELL BUCKLING
  - 80% OF STRUCTURE HAS M S > 0.50
- STRUCTURAL DYNAMICS
  - GOAL OF 40 Hz
  - 6 LOWEST NATURAL FREQUENCIES, 41.5, 41.9, 47.4, 48.0, 49.7, 54.4 Hz
  - FIRST MODE IS SHELL ASTIGMATISM

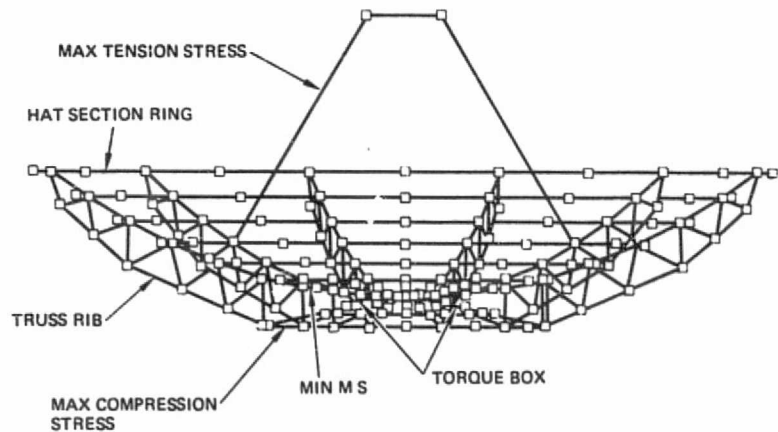


Figure 25. Structural analysis of 12-foot antenna.

Stresses and Margins of Safety. The antenna undergoes its most critical loading for the Space Shuttle crash condition while in the stowed configuration. For beam elements: maximum tension stress is 19608 psi; maximum compression stress is -11437 psi, and minimum margin of safety (M.S.) is +0.03 for crippling of the center bay edge longeron aft caps. This means structural failure of this element is expected with an increase of load of 3 percent. For membrane elements: square isogrid blade-type stiffening is required to give the basic 0.030 inch shell enough stiffness to resist buckling under the applied compressive loads (i. e., to give a zero margin of safety).

Structural Dynamics. The minimum natural frequency is 8.4 Hz for both the deployed and stowed configurations, but this value will increase due to the increased subreflector support thickness required as a result of the

internal loads analysis. The minimum shell natural frequency is 13.9 Hz for the stowed configuration. Both of these frequencies are above the expected 4 to 6 Hz major energy concentrations expected for the Space Shuttle launch environment.

#### 2.6.1.3 4.4 Meter Antenna

##### Antenna Support Arrangements

A number of supporting arrangements were investigated for the 4.4 meter symmetrical cassegrain reflector. Drawing SKDV770901 serves as a preliminary design for the basic reflector configuration in evaluating the various support methods. Assuming a weight distribution given before in Table XIV and the desire to support the antenna in line with its C.G. during launch, the following four concepts for structural arrangement were:

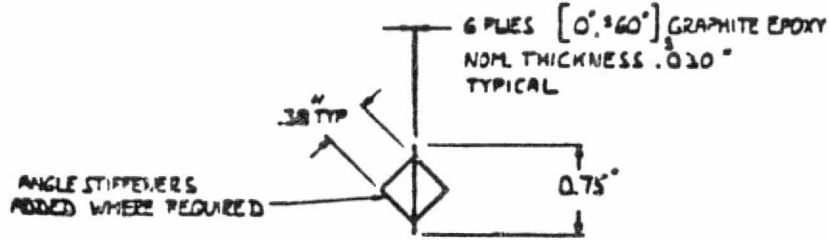
Concept No. 1. A determinate support at the back of the reflector torque box is proposed in this concept (see Figure 26). With a fixed attachment at the back of the reflector, the antenna must then pivot about the base of the support. This is a lightweight approach because of the direct tie between the reflector and the spacecraft, but the inertia during E-W axis scan is very large and may not be acceptable. The thermal distortion induced by this support design is minimal.

Concept No. 2. This partial yoke and beam concept shown in Figure 27 eliminated the large inertia effect due to E-W axis scan but because of its point of mount to the reflector can possibly induce thermal distortion. This is also a determinate mounting arrangement, provided that a scan mechanism is connected to one side only and the other side of yoke is free floating.

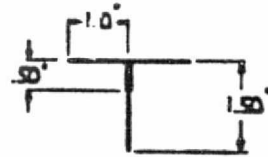
Concept No. 3. Here a nearly full yoke is employed as depicted in Figure 28. The intent is to get the support in close to the reflector. Thermal distortion effects are again a possibility here as in Concept No. 2. The separate gimbal points minimize the inertia effects due to scan.



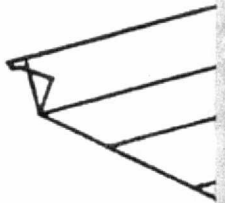
A-A  
ALTERNATIVE  
SECTION SHAPE



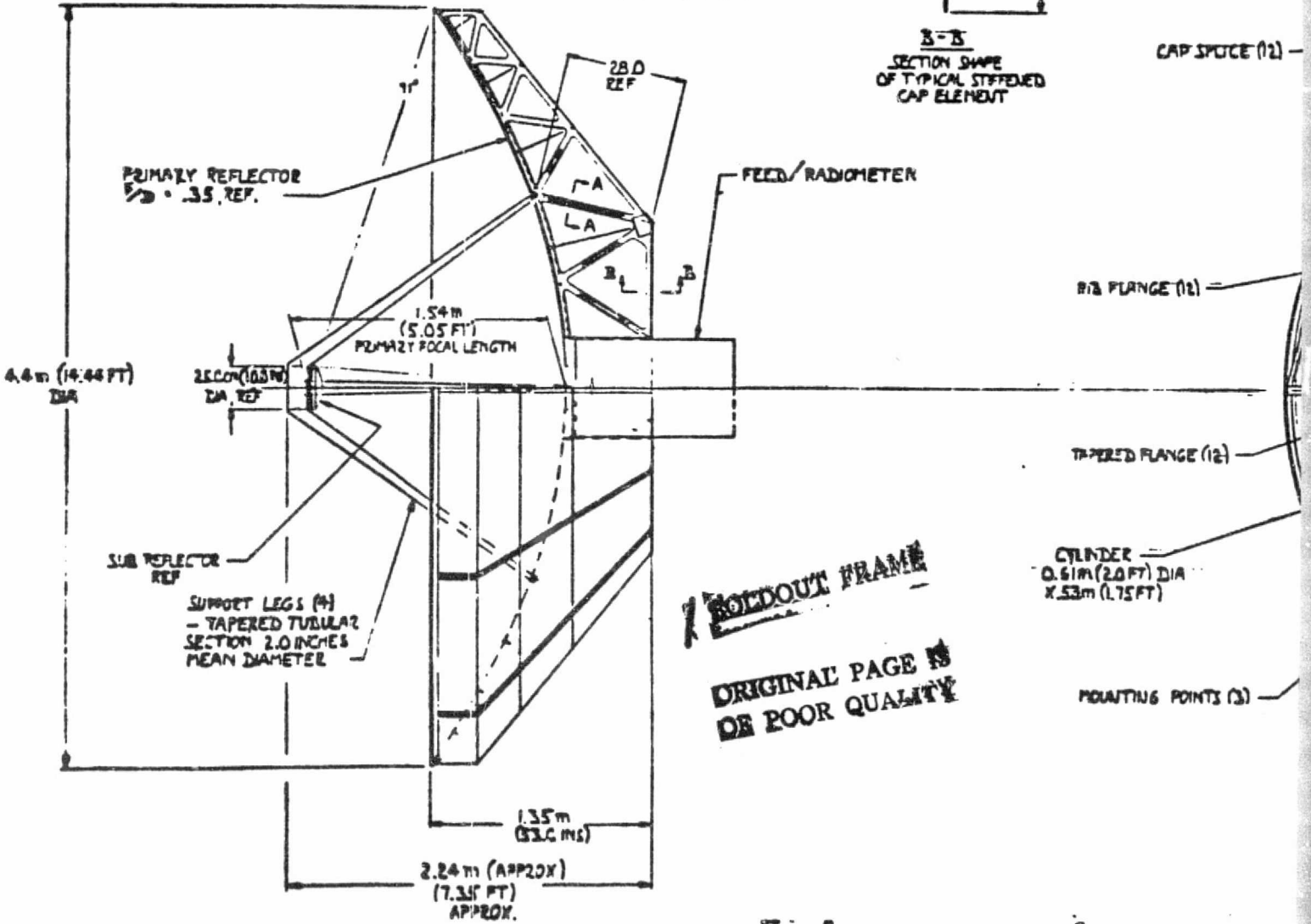
A-A  
SECTION SHAPE  
OF TYPICAL STIFFENED  
DIAGONAL ELEMENT



B-B  
SECTION SHAPE  
OF TYPICAL STIFFENED  
CAP ELEMENT

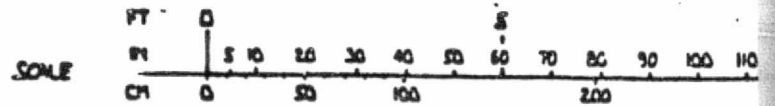


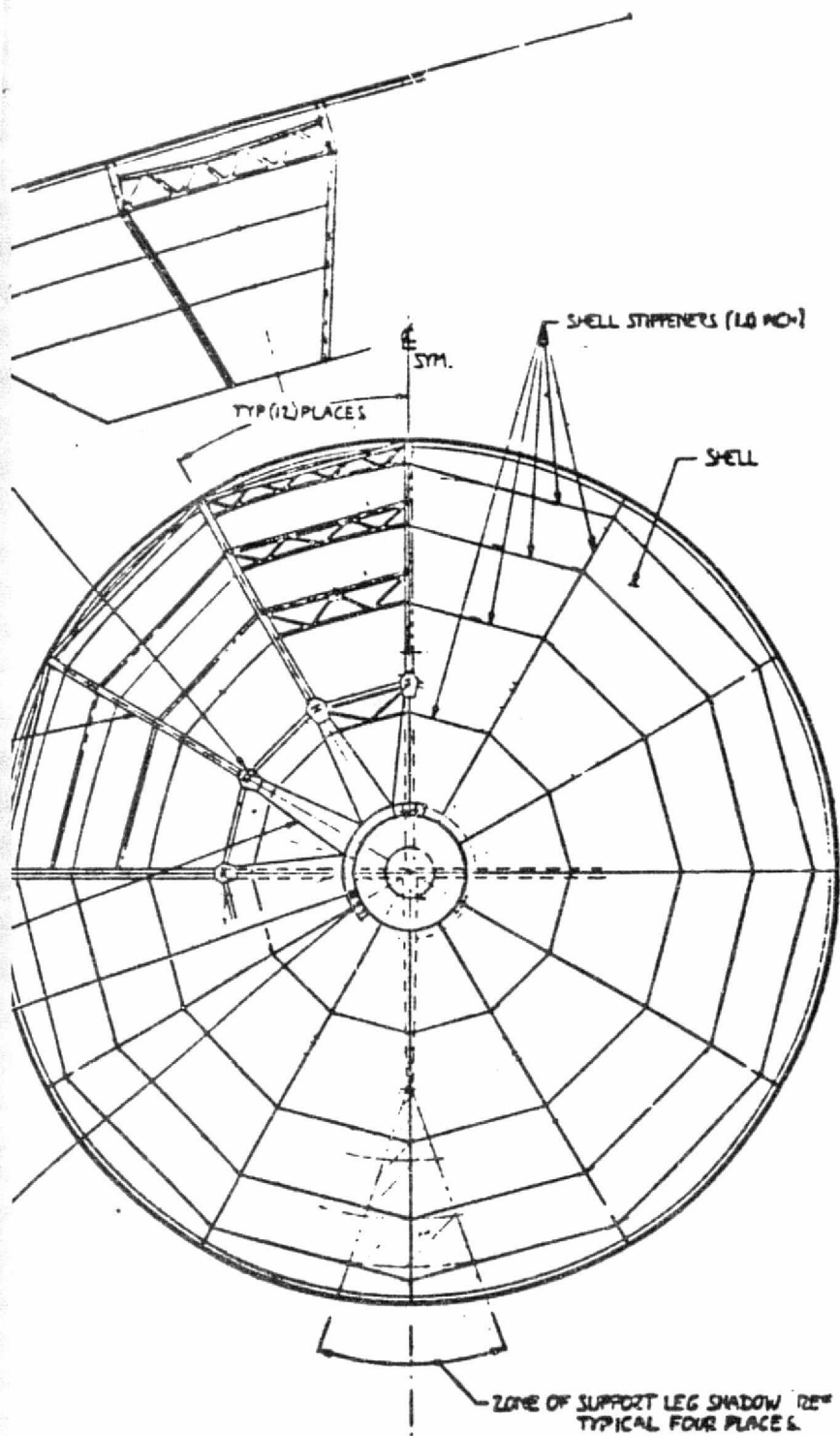
CAP SPACE (12)



**BOLDOUT FRAME**

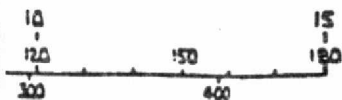
**ORIGINAL PAGE IS  
OF POOR QUALITY**





*J* FOLDOUT FRAME

ORIGINAL PAGE IS  
OF POOR QUALITY



MAT. GRAPHITE-EPOXY / X-30 6-PLY  
PSEUDO ISOTROPIC LAMINATE  
NOMINAL THICKNESS .03" THROUGHOUT,  
UNLESS OTHERWISE SPECIFIED

REVISED 6/77

PRELIMINARY DESIGN DRAWING	
4.4M CASSEGRAINIAN ANTENNA	
14170	3/2/770901

PRECEDING PAGE BLANK NOT FILMED

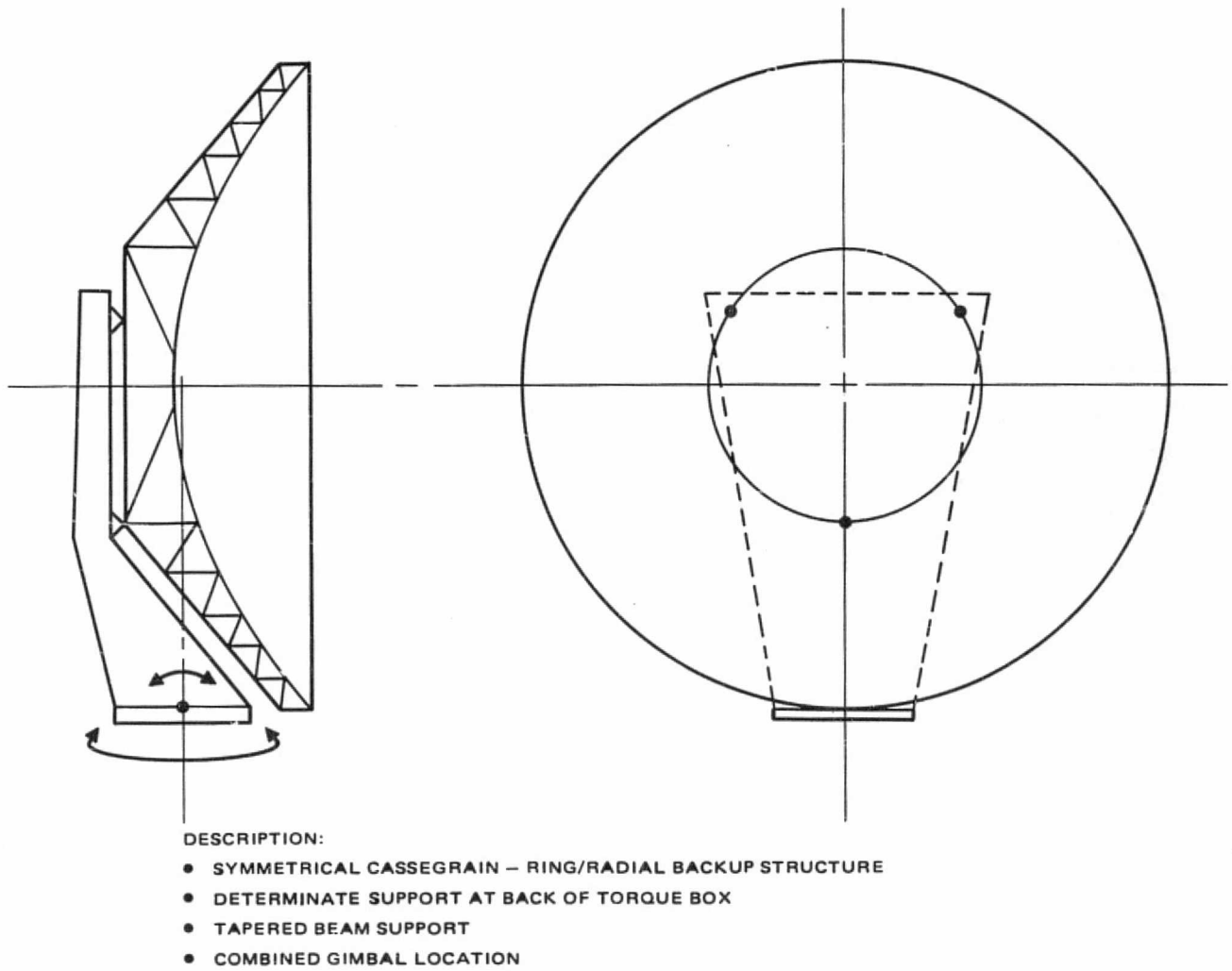
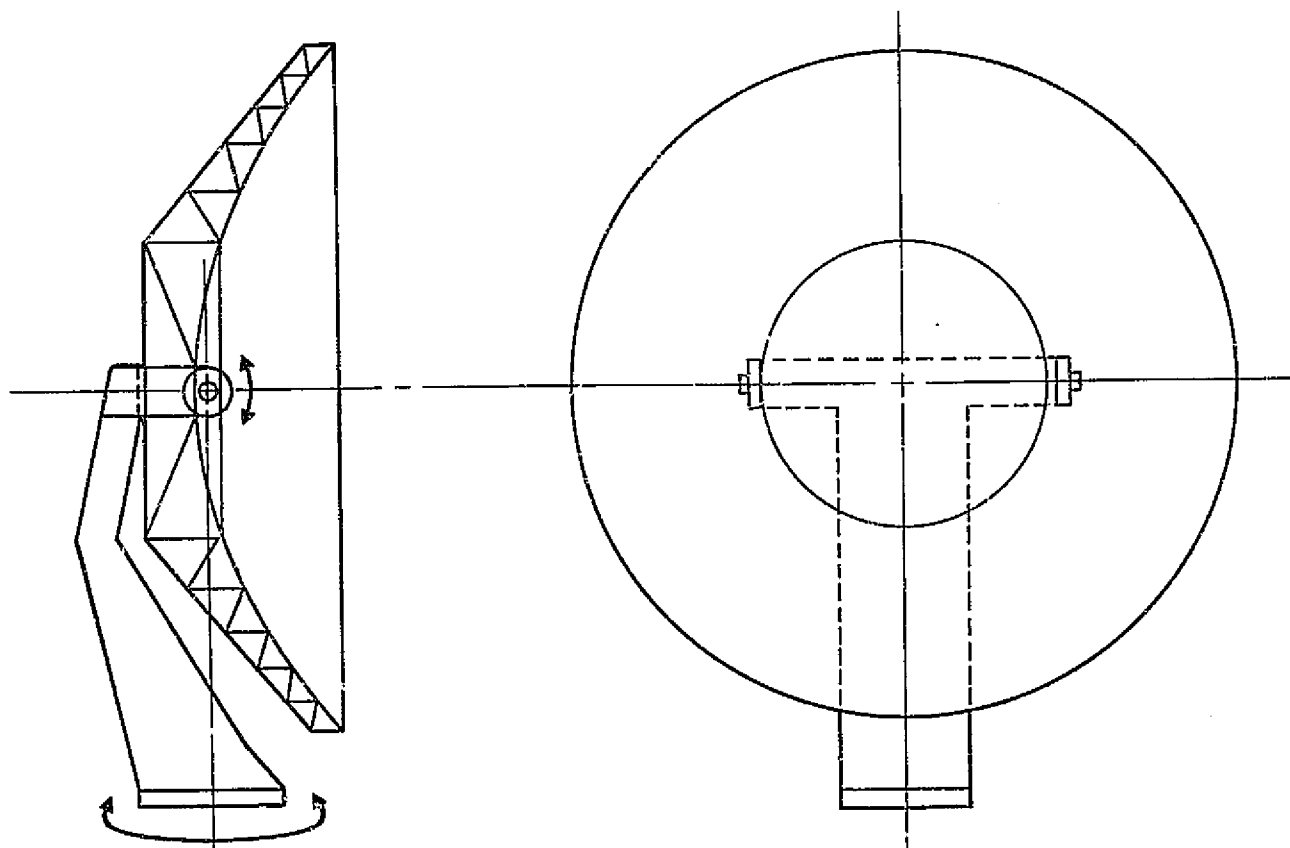


Figure 26. Concept No. 1.



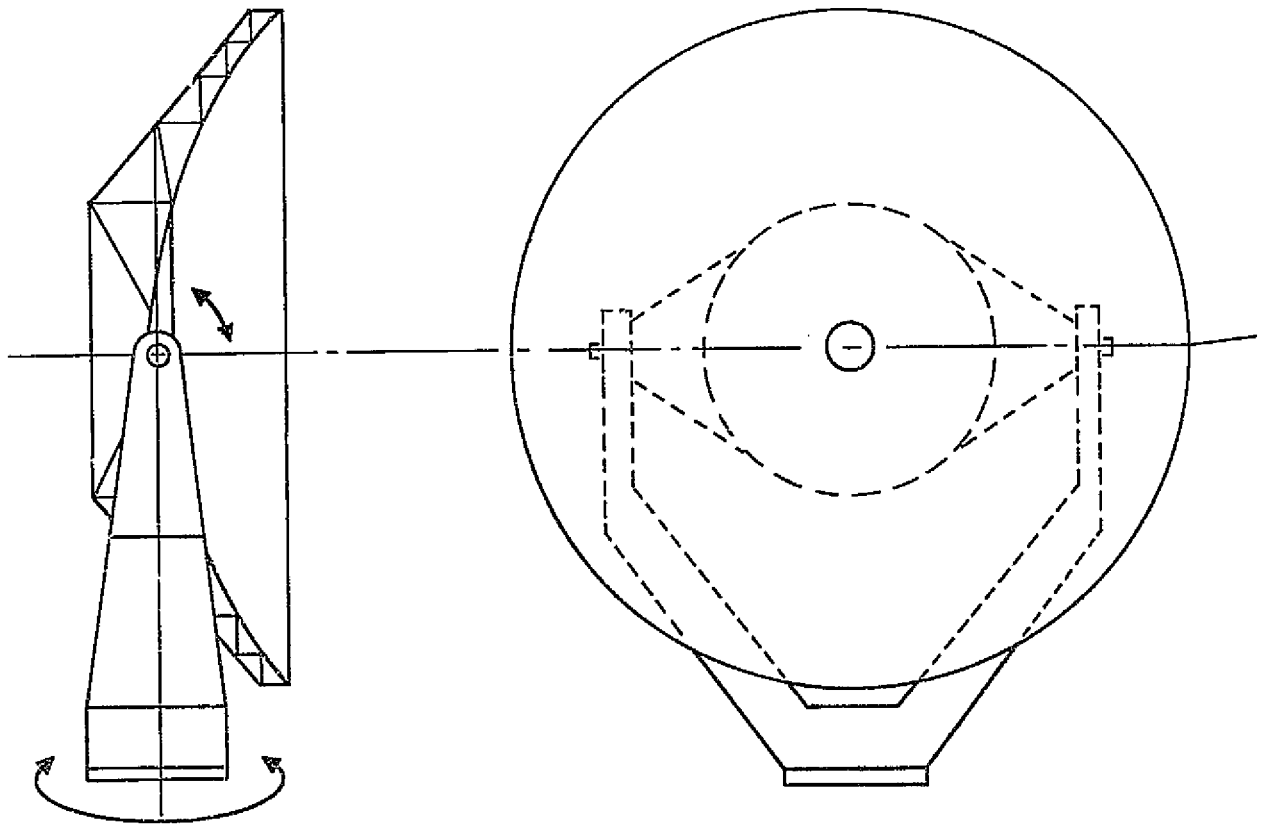
ORIGINAL PAGE IS  
OF POOR QUALITY



DESCRIPTION:

- SYMMETRICAL CASSEGRAIN - RING/RADIAL BACK-UP STRUCTURE
- DETERMINATE SUPPORT AT SIDE OF TORQUE BOX
- YOKE AND STRAIGHT BEAM SUPPORT
- SEPARATE GIMBAL LOCATIONS

Figure 27. Concept No. 2.

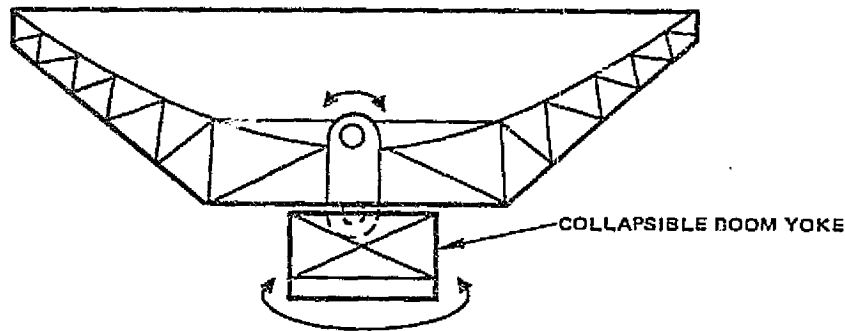


DESCRIPTION:

- SYMMETRICAL CASSEGRAIN - RING/RADIAL BACK-UP STRUCTURE
- DETERMINATE SUPPORT AT SIDE OF TORQUE BOX
- FULL YOKE SUPPORT
- SEPARATE GIMBAL LOCATIONS

Figure 28. Concept No. 3.

Concept No. 4. The weights of the prior support concepts are definitely greater than the 10 to 15 pounds necessary to keep weight within the 250 pounds set as a goal for the antenna system. This concept, shown in Figure 29, of a deployable support would offer the best chance of meeting the weight constraints (goals). A stiff and high strength support structure to withstand launch loads is not required because of the reduced moments created when the structure is stowed close to the spacecraft during launch.



DESCRIPTION:

- SYMMETRICAL CASSEGRAIN - RING/RADIAL BACK-UP STRUCTURE
- DETERMINATE SUPPORT AT SIDE OF TORQUE BOX
- COLLAPSIBLE BOOM/YOKE SUPPORT
- SEPARATE GIMBAL LOCATIONS

ORIGINAL PAGE IS  
OF POOR QUALITY.

Figure 29. Concept No. 4.

Some other possible ways to reduce the weight of this antenna support structure would be to add instruments (i. e., antenna pointing system) to a pallet behind the antenna reflector. This would have the effect of shifting the total system antenna and pointing system further in back of the reflector, thus allowing a single straight support (beam or pole) to come directly down to the spacecraft. Should the reflector interface be able to move down on the spacecraft, then a shorter straight support would be necessary.

2.6.2 Baseline Design Study: Deployable Symmetrical Cassegrain Antenna System

The baseline design study began with selection of a deployable symmetrical cassegrain antenna system. Primary reasons for selection of

this configuration were presented in earlier sections of this report. Selection of materials is discussed in Appendix B.

#### Deployable Support Frame

Graphite/Epoxy systems (i. e., HMS/934 and GY-70/934) would be considered acceptable alternatives to the GY-70/X-30 for this support structure. For this structure, thermal stability can possibly be of less concern than strength and cost. Structural stiffness is a prime reason for using the GY-70 fiber as opposed to HMS (or others) fiber, but it is not likely that the structural stiffness (dynamic) of the system will be determined by this support frame and gimbals.

Configuration. A deployable system was determined to provide the following advantages over a quasi-passive structure:

1. Reduced shuttle bay space required.
2. Reduced structural weight of total antenna system.
3. Higher dynamic stability during launch and payload orbital insertion.
4. Unloads gimbals during launch.

It is conceivable that the quasi-passive support tower could be more reliable (fewer moving parts) and less expensive (fewer systems) but the depth of study pursued herein does not demonstrate this to be correct.

#### 2.6.2.1 Study Plan

Starting with a general description of the MASR antenna as a symmetrical cassegrain reflector with a deployable support tower, the following study plan was exercised:

1. Define antenna requirements with respect to:
  - a. Interface envelope and attach points.
  - b. Gimbal type and interface.
  - c. RF requirements - (i. e., subreflector support blockage and location and RMS)
  - d. Loads (launch, payload insertion, slewing)

- e. System natural frequency (launch, payload insertion and slewing)
- f. Weight
2. Define the design approach.
3. Prepare baseline design drawings of various antenna systems.
4. Prepare math model and perform structural and distortion analysis of reflector and support structure.

#### 2.6.2.2 Results of Baseline Design Study

The required degree of surface accuracy for so large an antenna takes this task to the limits of the state of the art as seen in Section 2.6.1. General Dynamics/Convair has taken a minimum risk, minimum cost approach by building upon our existing substantial technology base:

(a) antennas up to 3.7M (12 feet) in size have been developed and characterized in existing Convair studies, and (b) a 2.4M (8 feet) diameter graphite/epoxy antenna was built and subjected to comprehensive thermal, vacuum, g-loading, vibration and RF tests.

The MASR antenna system, which is essentially a scaled-up version of the 8 and 12 foot antennas, was viewed to have the same general, yet critical, design requirements:

1. High fabrication accuracy of the reflective surface.
2. High shape stability in varying thermal environment.
3. High shape stability in varying dynamic environment.
4. Provision of antenna/spacecraft interface structure compatible with specified antenna slew requirements.
5. Compact and efficient stowage provisions and structural integrity of stowed configuration compatible with space shuttle launch requirements.
6. Reliability and durability in the space environments.
7. Minimum cost.
8. Minimum weight.

## Requirements

The specific requirements which relate directly to the MASR antenna system and which were used in subsequent design and analysis are as follows:

Interface Envelope and Attachments. Defined on HAC drawing 60320-20A, Figure 3.1 from Report SCG6032R (Stormsat Final Report) incorporated here for reference. Note that the MASR diameter in the figure is less than 4.4 meters.

Gimbal. Defined on HAC drawing 3574724. (See Figure 51, Section 2.7.2.)

## RF

Operating Frequency 104 - 193 GHz.

Surface Accuracy - 1.7 mils RMS

Transverse feed position fixed to within 2 mils (in-orbit conditions)

Weighted beam efficiency greater than 85 percent

## Loads

$N_x = 4.0$  g's (along axis of shuttle)

$N_y = 5.0$  g's (parallel to shuttle wing axis)

$N_z = 15$  g's (normal to shuttle wing)

(Loads were defined as worst case for launch, orbiter insertion of payload, and slewing.)

Frequency. 15 Hz.

Weight. 150 pounds plus 50 pounds feed and 50 pounds gimbal. This requirement may be relaxed in the interest of achieving performance goals.

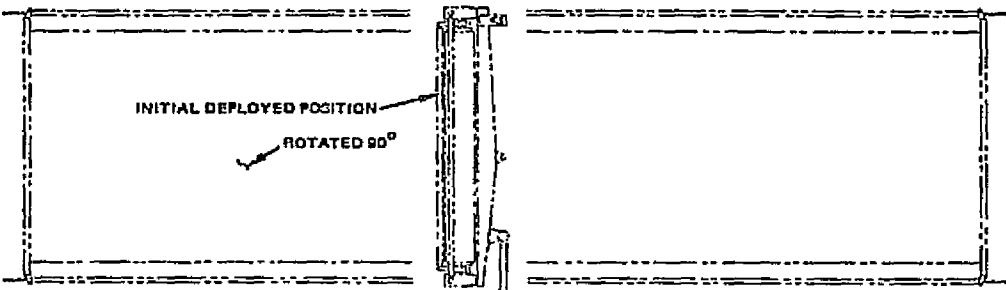
## Geometry

4.4 meter diameter reflector

F/D = 0.35

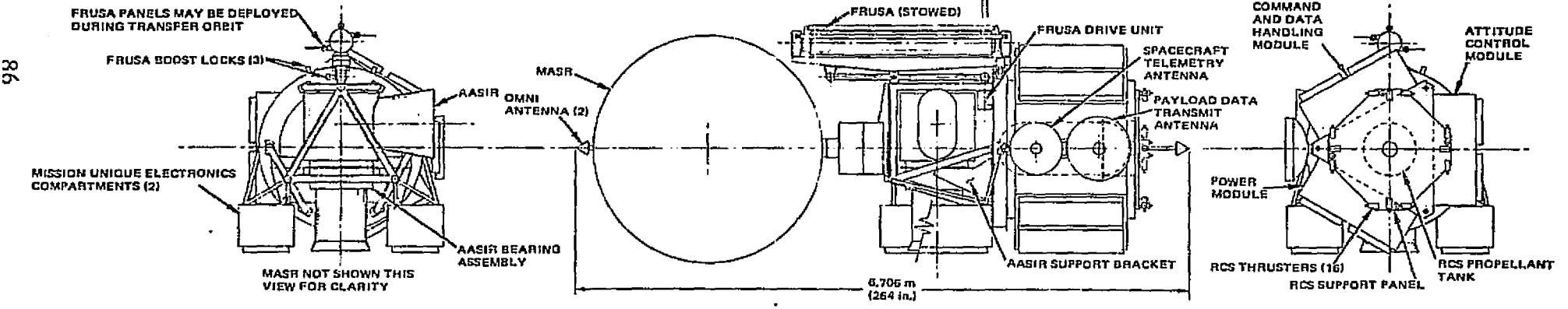
25 cm diameter subreflector

0.6 meter diameter radiometer module (20 cm diameter hole in reflector).



STORMSAT - OPERATIONAL CONFIGURATION

ORIGINAL FIGURE IS  
OF POOR QUALITY



a) VIEW 1

FIGURE 3-1. STORMSAT GENERAL ARRANGEMENT

### Design Approach

In the subject task the most critical requirement driving the structural design is dimensional stability. Typically, the necessary reflective surface accuracy of the reflector is a function of the wavelength ( $\lambda$ ).

In this case where operating frequencies will be as high as 193 GHz, the primary reflector surface contour must be within 0.0017-inch RMS of the perfect paraboloid, this value being the summation of fabrication errors and thermal and dynamic distortions in the operating environment. Such accuracy requires the use of high stability, high efficiency materials and design techniques emphasizing structural efficiency and rigidity.

High dynamic stability is also a requirement in the design of the support structure interfacing the antenna system with the spacecraft. Here stiffness must be provided compatible with the required system natural frequency with minimum weight impact on the antenna system structure. Considerable weight saving, in the design of this interface structure, was achieved by retracting the antenna to a position and attitude more appropriate to the launch phase than is its cantilevered operational location. This was achieved by designing the interface structure to be retractable/deployable, and by providing a secondary structural system designed solely to provide launch phase support. Such a concept has the additional advantage that the interface structure and antenna slew bearings would be virtually unloaded during boost phase.

With the understanding of the design requirements, the various assemblies that make up the total antenna system were studied in detail for their possible design options.

### Reflector Shell (Skin)

Option 1 - Single piece skin requiring large, high accuracy tool.

Option 2 - Subpanels (4, 5 or 12) assembled and aligned individually.

Segmentation seems attractive since it sharply reduces both size and cost of tooling, reduces the risk of scrappage and seems to suggest increased capability of shape adjustment (tuning). However, such segmentation destroys structural continuity, and the overall shape stability



characteristic of double curvature membranes is largely lost. Segmentation would greatly increase the total 'free edge' length, and 'free edge' shape errors are particularly troublesome to correct. Segment-to-segment alignment, to the tolerances required, could prove to be extremely difficult.

The effects of electrical discontinuity and of gaps between segments could also be significant to the primary function of the reflector.

As a result of this assessment of the two options, Option 1, a single piece skin was selected.

#### Subreflector Support Structure

Number of supports -

Option 1 3 Legs

Option 2 4 Legs

Option 3 5 Legs

The three-legged approach gives the least part count and minimum optical obscuration or blockage. It is also the lightest and least costly.

The concept of four legs equally spaced is more compatible with R.F. requirements for symmetry with minimum blockage.

The six legged configuration has superior structure rigidity since all members of its triangulated geometry react loads purely axially. Compared to the above this concept is very resistant to decentering deflections. It is heaviest and most costly and offers the greatest blockage.

Option 2 was selected for its RF performance characteristics.

#### Attachment Location at Reflector

The distance of the leg/reflector interface point(s) from the vertex of the reflector is significant in that there is a tradeoff between structural rigidity and loss of reflector area due to obscuration. The further outboard the attachment point is located then the smaller is the projected shadow (see Drawing SKDV 77090.), but at the expense of longer legs and therefore degraded subreflector stability.

### Slew Mechanism

- Option 1 Conventional 'az-el' (azimuth turntable and elevation trunnions) arrangement (i. e., horizontal (elevation) axis passing through prime axis of reflector with trunnions sufficiently separated to permit axis to be located through reflector c. g. ). The entire antenna system mounted on a horizontal turntable with vertical axis passing through c. g. of antenna.
- Option 2 Double actuated joint with same axes orientation as above but reduced to compact unit with two bolt on interfaces, one static and the other controllable in azimuth and elevation.
- Option 3 Conventional biaxial gimbal arrangement with interface ring carrying both x and y axes.
- Option 4 Flex joints - Any of the above with flex-joints substituted for conventional bearings for angular motion.

HAC recommended Option 2 because of similar designs in service. GD/C incorporated HAC design into structural arrangement of antenna support frame structure.

### Support Frame

- Option 1 Folding Frame
- Option 2 Telescoping Frame

Because of the discrete attach points to the spacecraft, a folding frame is expected to be more readily adaptable and lighter in weight. Latching mechanisms and activating mechanisms are expected to be less complex and less critical to alignment.

### Baseline Design Description

The selected baseline configuration (Figure 30) is a cassegrainian with a primary F/D ratio of 0.35. The paraboloidal primary reflector is 4.4M diameter while the aluminum secondary (sub-reflector) is 25 cm diameter. The RF feed is located close behind the primary reflector vertex and is contained within the 0.60M diameter radiometer module.

In order to meet the stringent thermal stability and dynamic stiffness requirements, the selected structural material for the reflector assembly is basically GY-70/X-30 graphite/epoxy, pseudoisotropic laminate.

ORIGINAL PAGE IS  
OF POOR QUALITY

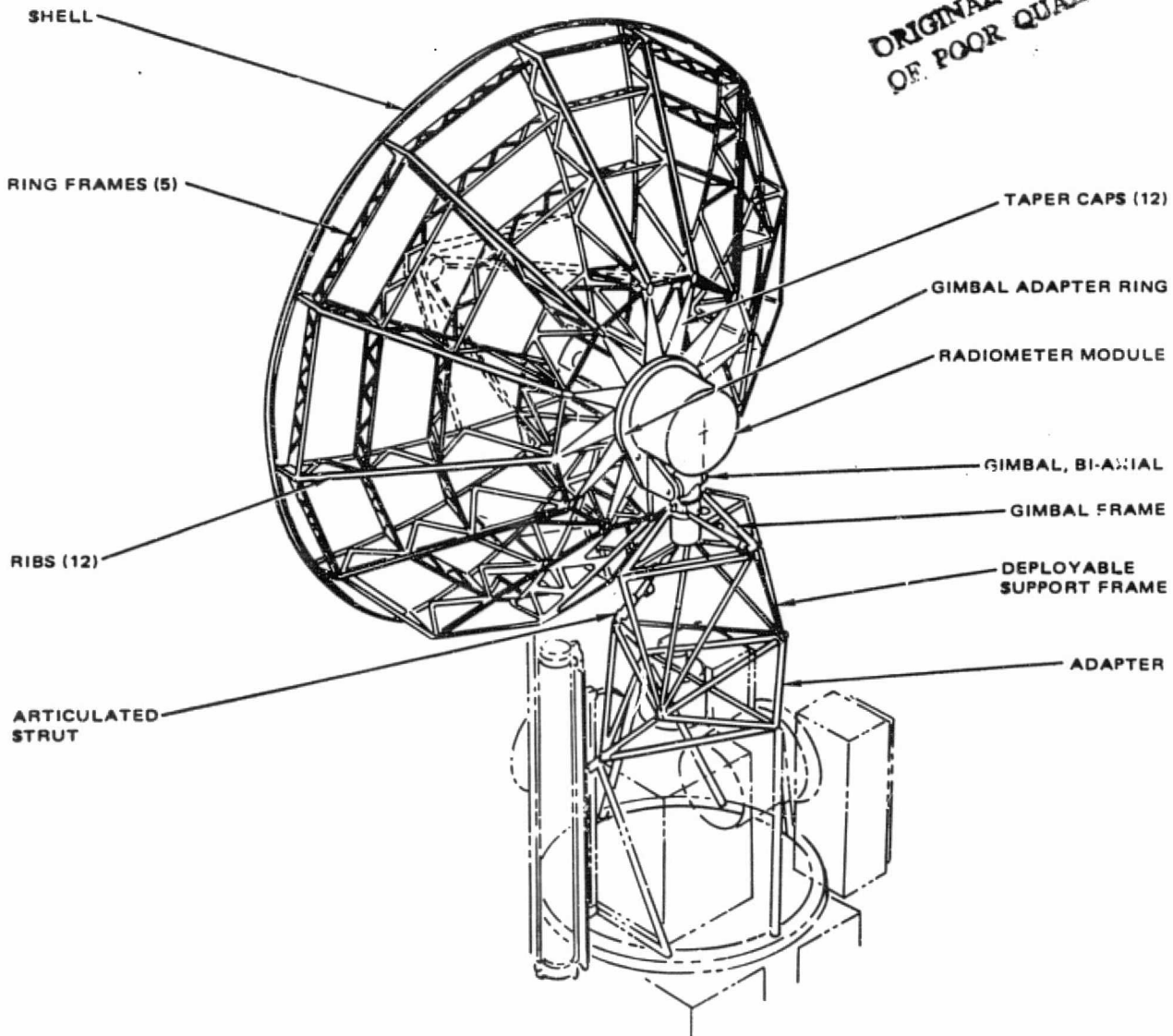


Figure 30. MASR baseline antenna system.

For the adapter and support frame where structural stiffness is more critical than thermal stability, the laminate for the structural elements is more predominantly unidirectional.

The support frame deploys from its stowed location, shown in Figure 31, by rotating its two space frames (reference Figure 32) to achieve the deployed (operational) configuration shown in Figure 32.

ORIGINAL PAGE IS  
OF POOR QUALITY

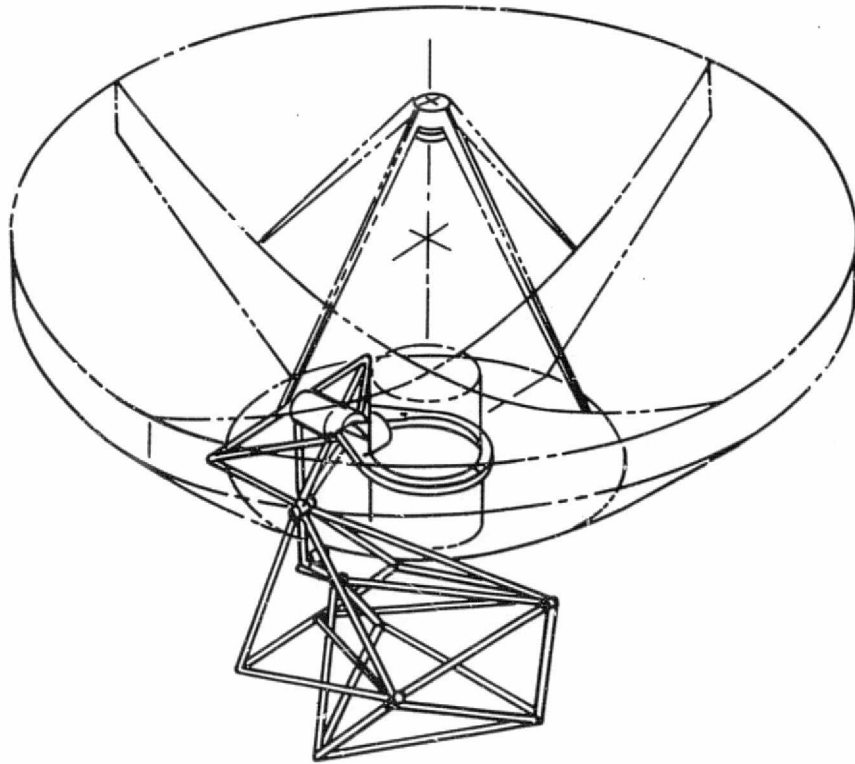


Figure 31. Stowed MASR antenna.

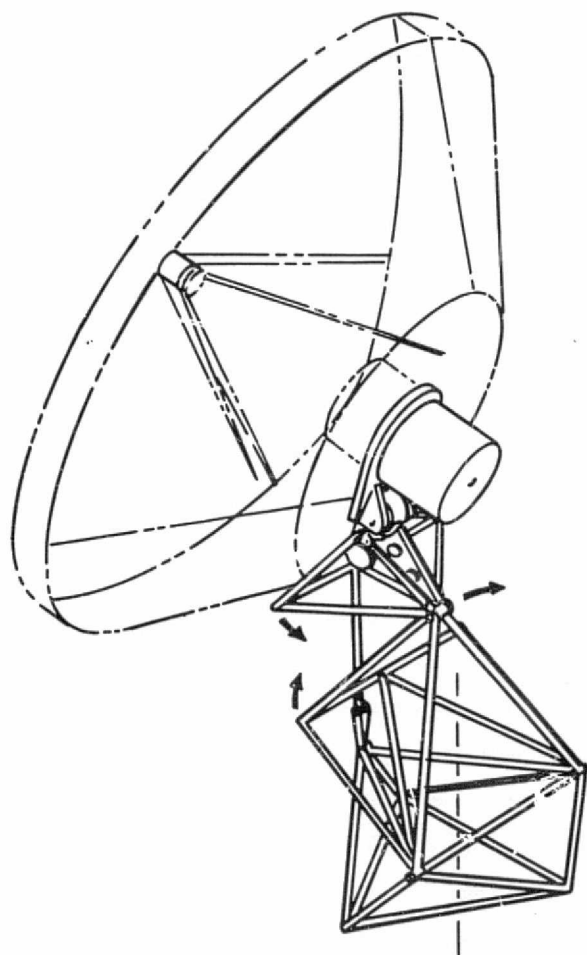


Figure 32. Deploying MASR antenna.

Inclusion of aluminum, titanium or Invar fittings may be required in instance of:

1. High point loadings (such as tube end and attachments.)
2. Frame structure node point splices.
3. Launch phase structure attachment points.

The subreflector support system consists of four, equally spaced, minimum section, tapered, round struts, reference Figure 30.

In the stowed position, the antenna rests upon six secondary support struts which provide support during the boost phase (reference Figure 33), and then disconnect and retract to permit inspace deployment of the antenna system.

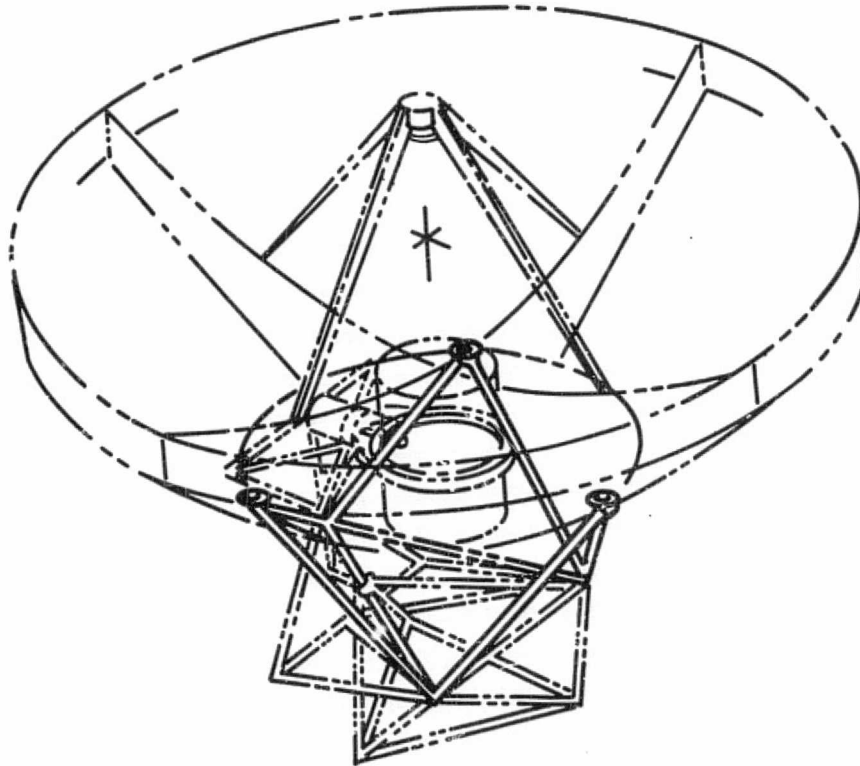


Figure 33. MASR antenna launch supports.

Reflector Structure. Drawing SKDV770901 presents a reflector baseline design developed from our existing designs to satisfy the specific requirements of the 4.4 meter (14.4 feet) MASR system.

Prior to the final stage of assembly, the reflector assembly consists of two major subassemblies:

1. A paraboloidal shell with a web pattern of 1-inch stiffeners bonded to its convex surface.
2. A three-dimensional, triangulated truss structure with a web configuration matching that of the shell stiffeners.

The faying surfaces at the interface of these two subassemblies are oriented normal to the reflector shell thus providing inherent shape adjustment capability. Before performing final bonding, the faying surfaces are clamped and a contour survey made of the reflector surface. Local shape deviations are then correctable by discretely adjusting the faying surfaces, where necessary, and reclamping. When the required shape accuracy is

achieved throughout, a room temperature cure adhesive is injected between the faying surfaces so that the stiffened shell and the backup structure then became a single, integrated deep truss structure.

The baseline design consists of twelve radial ribs and five concentric structural rings which, in effect, divides the single-piece shell into (72) zones. Thus, along the periphery of these zones the shell can be directly adjusted to the desired contour as described above. Accurate fabrication and the characteristic shape stability of a double curvature shell assures shape conformity within each zone. The average size of these zones is approximately 500 in.<sup>2</sup>. Figure 30 illustrates typical frame and rib details. Previous experience (8 ft antenna) indicates that adjustments along the rib members are most effective, but because zones are larger, intermediate adjustments at rings and between ribs provide additional adjustment capability without adding more ribs.

Shape error correction is best effected by determining influence coefficients of each discrete adjustable 'point' of a pattern and by utilizing available computer programs to determine overall corrections required to bring a shape survey to the required 'best fit' condition. However, in this case the shape adjustments should be of such small magnitude that their effect may prove to be very localized and thus essentially discrete in nature.

The shell itself is a thin (0.03-inch) single piece shell of pseudoisotropic GY-70 graphite/epoxy composite selected and laid up to give maximum dimensional stability in a varying thermal environment ( $CTE = <0.20 \times 10^{-6}$  in. / in. °F).

Deployable Support Frame (Tower). Drawings SKDV770927 and 28. A deployable concept for the antenna support tower was selected for the baseline design. Because cost of utilizing the space shuttle is based on weight and payload bay length occupied, the concept of an erectable support tower is attractive on grounds of economy. It also permits a more secure, stiffer boost phase support structural system and the opportunity to unload the gimbal during boost phase. Further, since the entire antenna installation cantilevers from the front end of the spacecraft the smaller the effective length of cantilever the less is the lateral 'g' loading.

FOLDOUT FRAME

ORIGINAL PAGE IS  
OF POOR QUALITY

ANTENNA (S/C 770901)  
OPERATIONAL CONFIGURATION

VERTEX REF

ADAPTER MOUNT

BIAXIAL TORQUE  
INSTALLATION

UPPER TRUSS, SUPPORT TOWER

ROTARY ACTUATOR  
- FOR DEPLOYMENT ONLY

LOWER TRUSS,  
SUPPORT TOWER

ROTARY ACTUATOR  
- DEPLOYMENT ONLY

INTERFACE ADAPTER

TRUSS  
(STOWED)  
REF

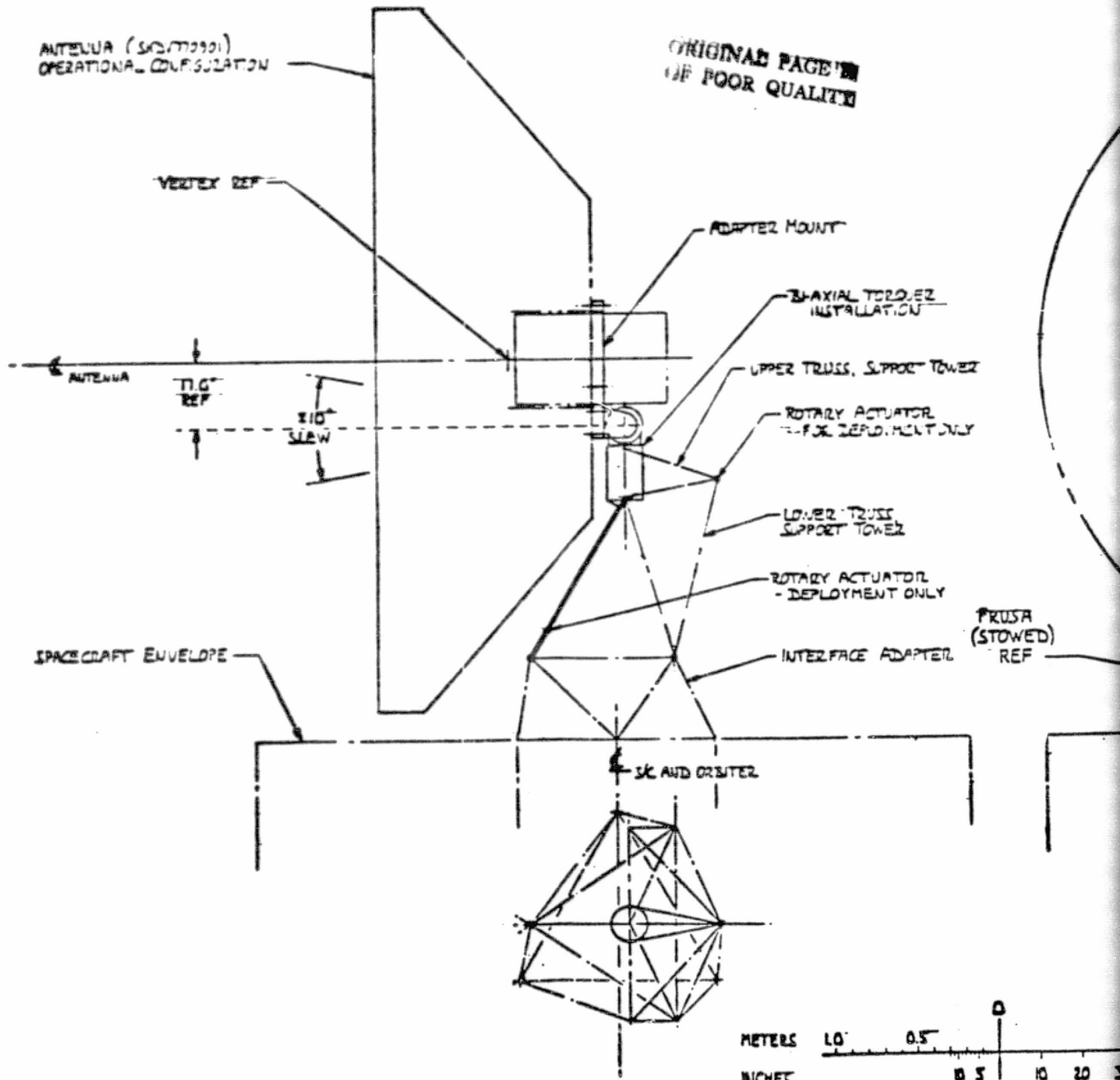
T.T.G.  
REF

±10°  
SLAW

ANTENNA

SPACECRAFT ENVELOPE

S/C AND ORBITER



METERS

10

0.5

0

INCHES  
FEET

0.5

0

10

20

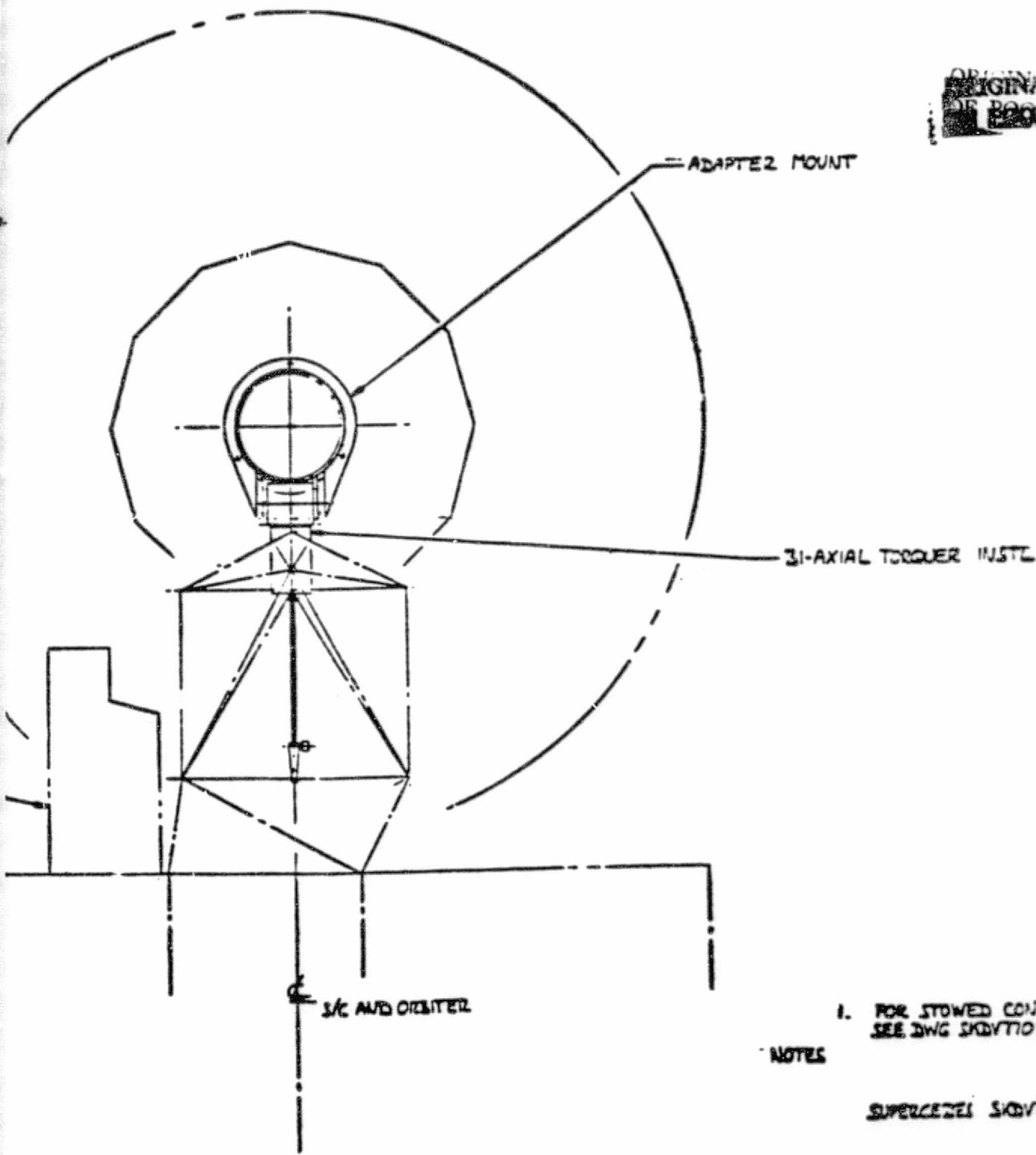
30

SCALE:—



2 **WELDOUT FRAME**

**ORIGINAL PAGE IS  
OF POOR QUALITY**

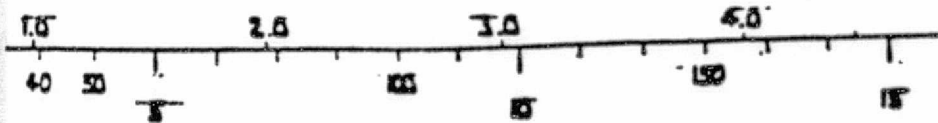


- 1. FOR STOWED CONFIGURATION  
SEE DWG SK0V770928 & 929

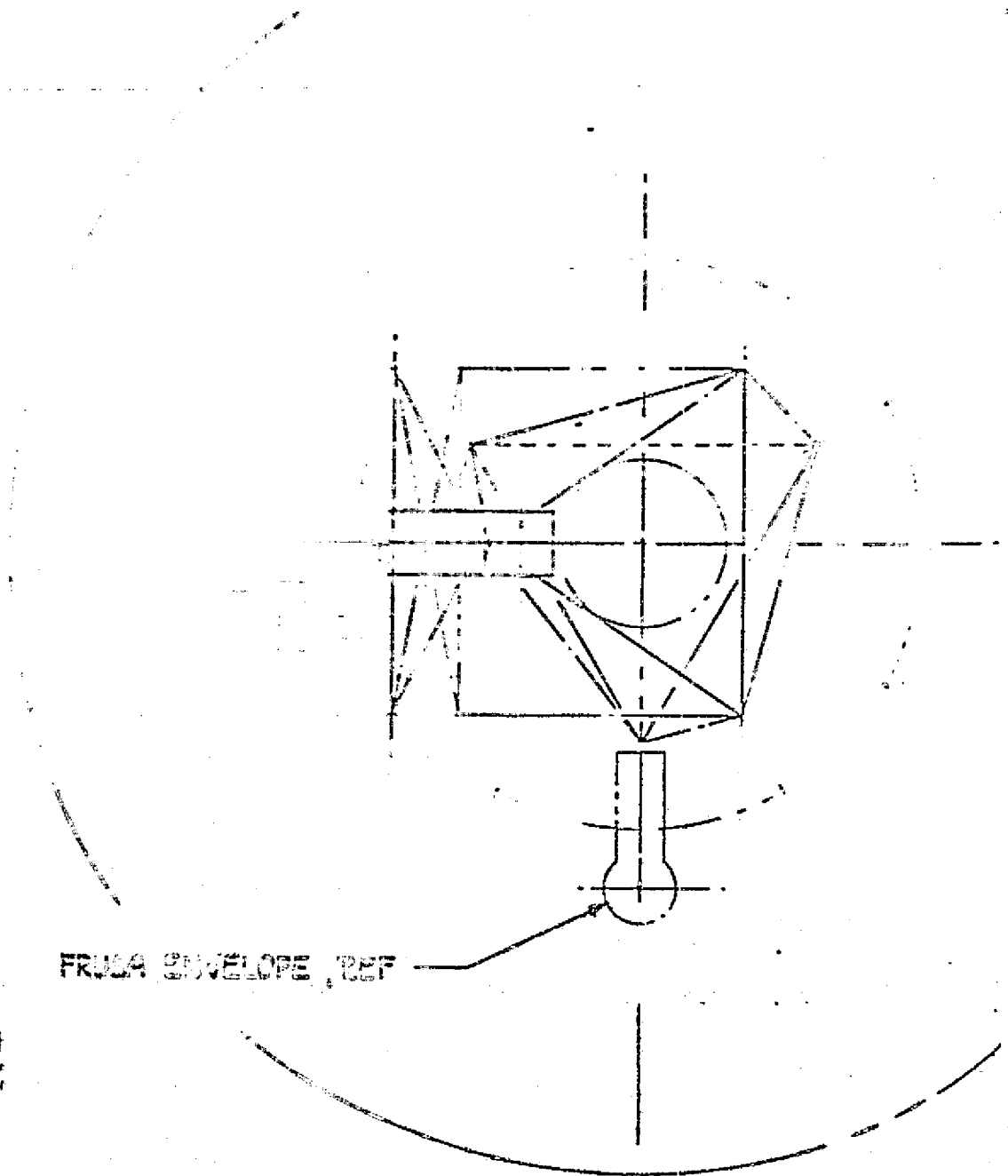
NOTES

SUPERSEDES SK0V770920

REVISED 01/77



PRELIMINARY DESIGN DRAWING	
C & M ANTENNA SYSTEM	
- DEPLOYED CONFIGURATION	
NAS2 / STORMCAT	
DESIGNED BY	14170 SK0V770927
CHECKED BY	
APPROVED BY	
DATE	

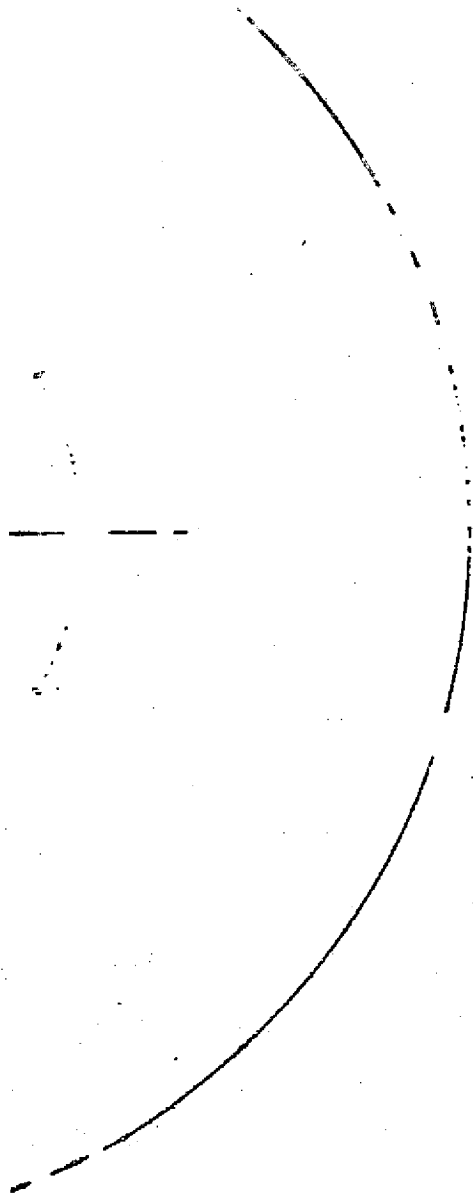


FROM ENVELOPE, REF

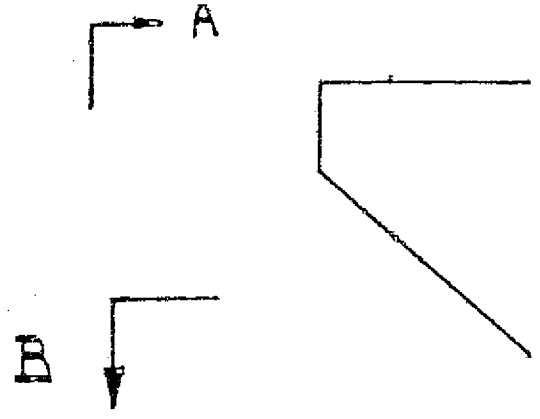
ORIGINAL PAGE IS  
OF POOR QUALITY

REPRODUCTION

B - B

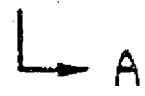


ORIGINAL EDGE  
SEE FIG. 4



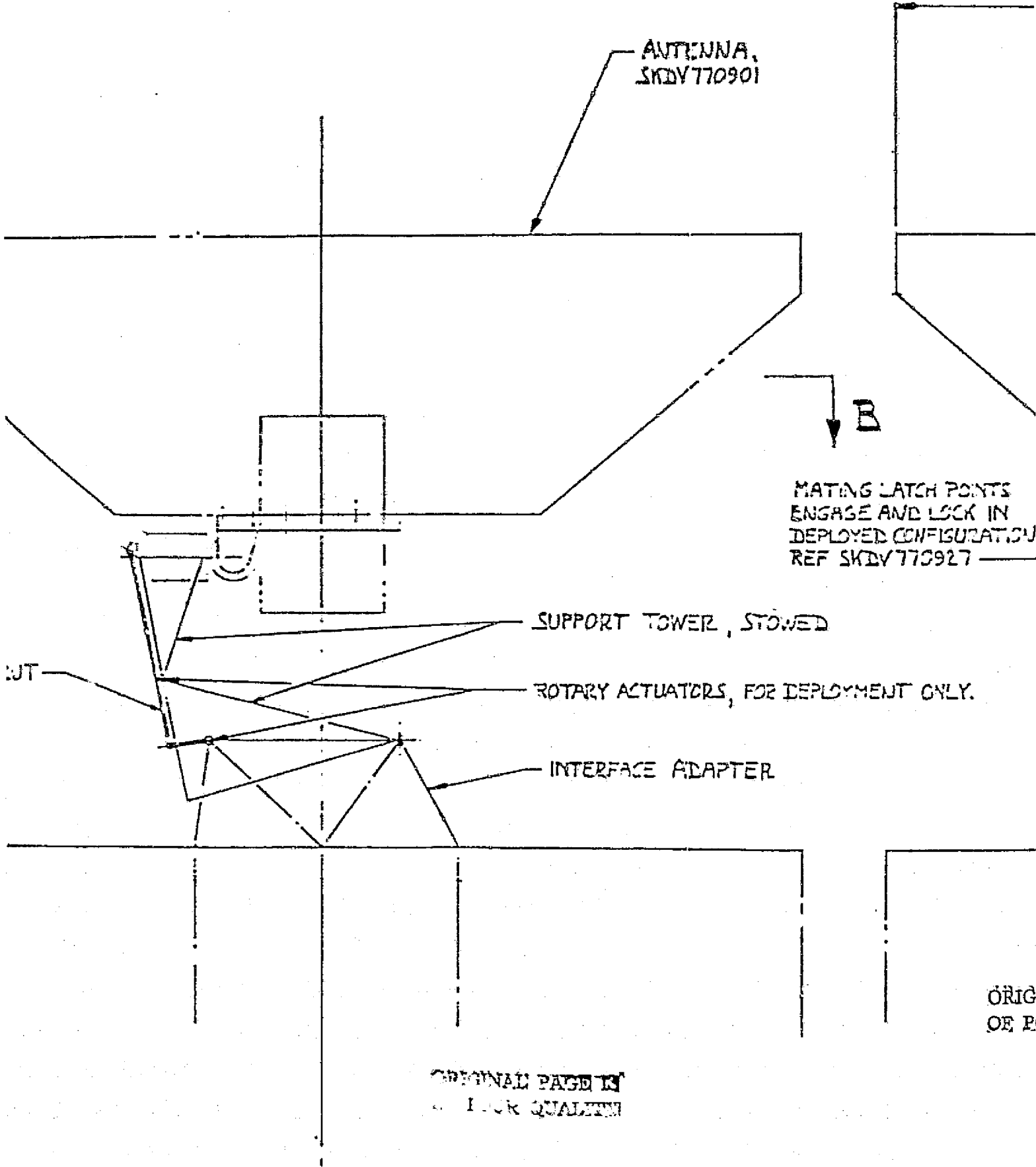
ACTUATED DEPLOYING STR

SPACECRAFT  
ENVELOPE



2

FOLDOUT FRAME



ANTENNA,  
SKDV770901

MATING LATCH POINTS  
ENGAGE AND LOCK IN  
DEPLOYED CONFIGURATION  
REF SKDV770927

SUPPORT TOWER, STOWED

ROTARY ACTUATORS, FOR DEPLOYMENT ONLY.

INTERFACE ADAPTER

WT

B

ORIGINAL PAGE IS  
OF HIGH QUALITY

ORIG  
OF P

3

FOLDOUT FRAME

14.4471  
(4.4 M)  
DIA, REF.

DE

NO LATCH POINTS  
SE AND LOCK IN  
MED CONFIGURATION  
NOV 770927

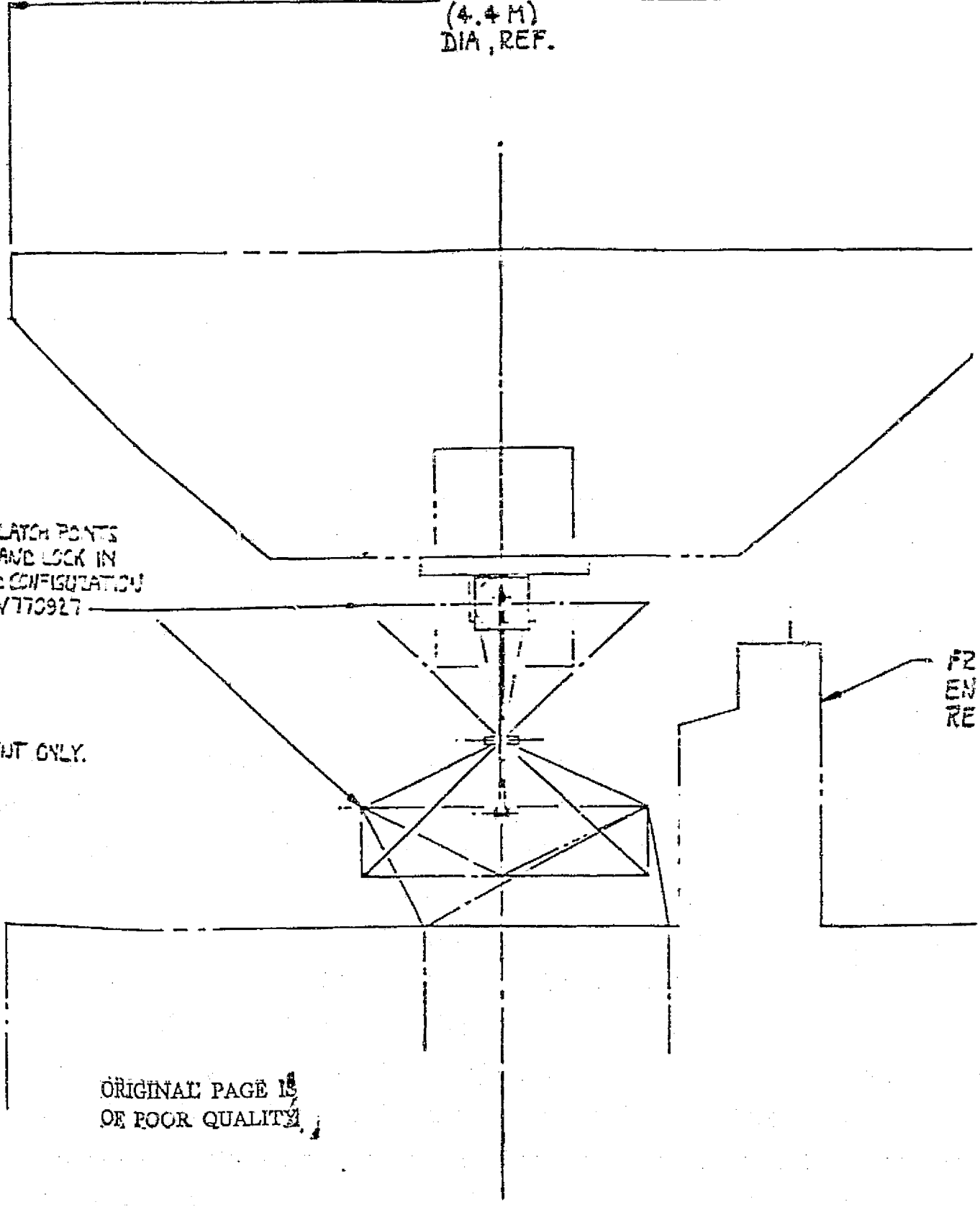
MENT ONLY.

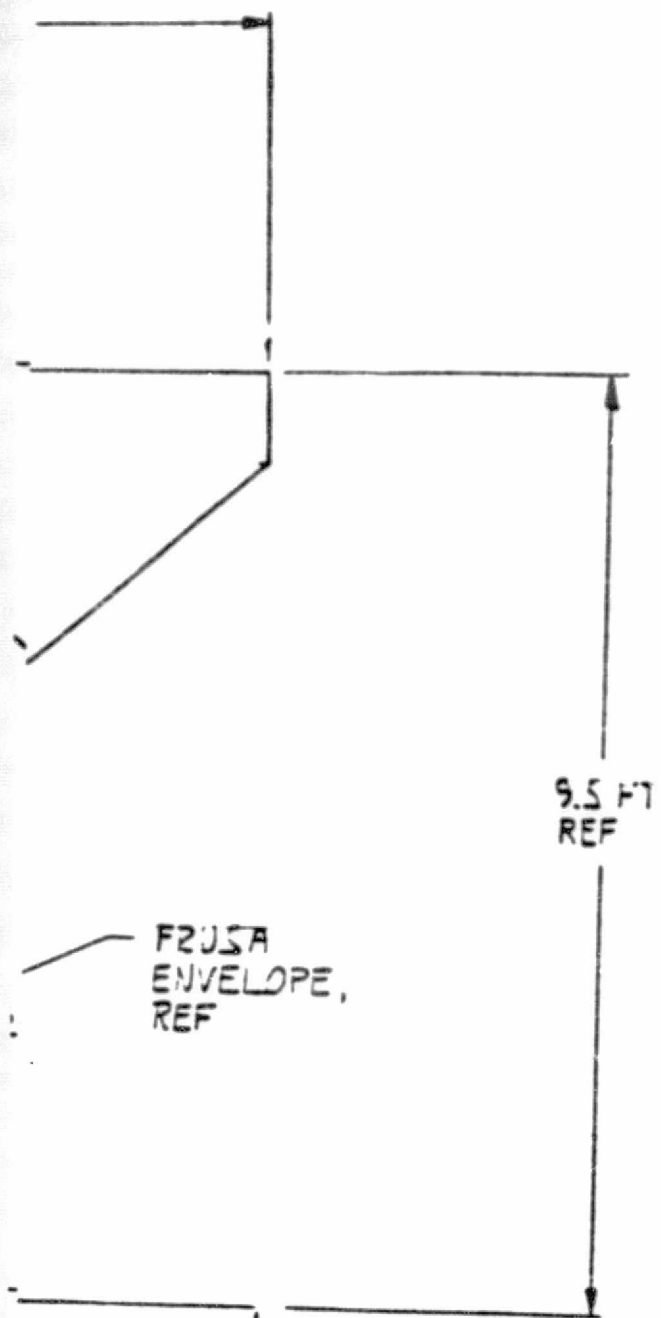
PRE  
RE

ORIGINAL PAGE IS  
OF POOR QUALITY

A-A

FOLDOUT FRAME





ORIGINAL PAGE IS  
OF POOR QUALITY

BOLDOUT FRAME

2 FOR DEPLOYED CONFIGURATION  
SEE DWG SKDV770927

1 FOR BOOST PHASE SUPPORT STRUCTURE  
SEE DWG SKDV770929

NOTE:

~~PRECEDING~~ PAGE BLANK NOT FILMED

REVISED 10/1/77

5

PRELIMINARY DESIGN DRAWING	
4.4 M ANTENNA SYSTEM	
— STOWED CONFIGURATION	
STORM SAT	
GENERAL DYNAMICS Cosmic Aerospace Division SAN DIEGO, CALIF.	14170 SKDV770928

The tower consists of two space frames that deploy from their stowed configuration, reference Figure SKDV770928 by rotating relative to each other and relative to the base pedestal as shown in Figure 31 to achieve the deployed (operational) configuration shown in Drawing SKDV770927.

Deployment is effected by means of an articulated strut that drives the upper frame to its deployed location and by a rotary actuator (powered hinge) that rotates the frames into their deployed orientation.

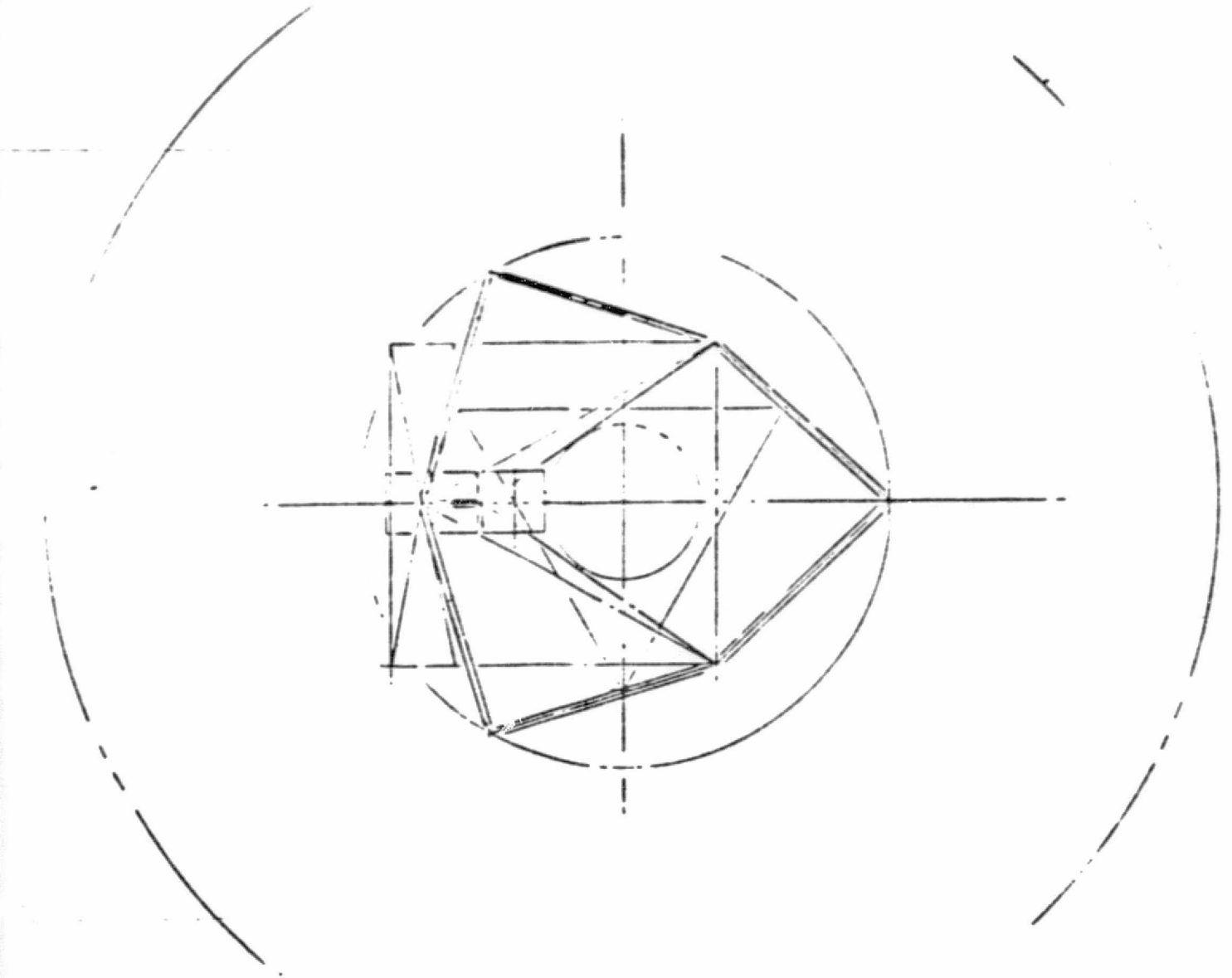
Subreflector. The subreflector support consists of four hollow rectangular sections tapered for structural efficiency (see Drawing SKDV770901). Although this arrangement has one leg more than the minimum required for structural adequacy, the compensation is that the fourth leg tends to contribute to the stability of the reflector since the four attachment points tend to stay in-plane and RF symmetry is maintained.

As shown, the legs attach to the reflector backup structure at node point's 45 inches from the vertex, throwing the shadow shown. This loss of reflector surface area could be reduced by relocating leg attachment outboard to the next structural node point 64 inches from the vertex. However, this improvement must be traded against resultant degradation of subreflector position stability relative to the feed.

Feed Installation (Radiometer). The 'feed' unit (defined on drawing SKDV770901) is defined as a cylindrical canister requiring a 24-inch diameter accommodation. It is set back 6 cm from vertex. A 20 cm hole is required in reflector shell for the feed unit.

Launch Phase Support Structure. Drawing SKDV770930 depicts this support structure in a launch configuration. A series of struts in a truss arrangement attach the back support structure of the antenna to the support tower interface structure. Upon deployment of the antenna these struts will rotate about their lower interface attach point and be caught by suitably designed stops on the interface structure.

~~PRECEDING PAGE BLANK NOT FILMED~~



B - B

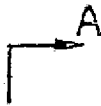
FOLDOUT FRAME

ORIGINAL PAGE IS  
OF POOR QUALITY

ORIGINAL PAGE IS  
OF POOR QUALITY



ANTENNA  
SKDV770901  
REF



BOOST PHASE SUPPORT  
STRUTS, MINOR (3)

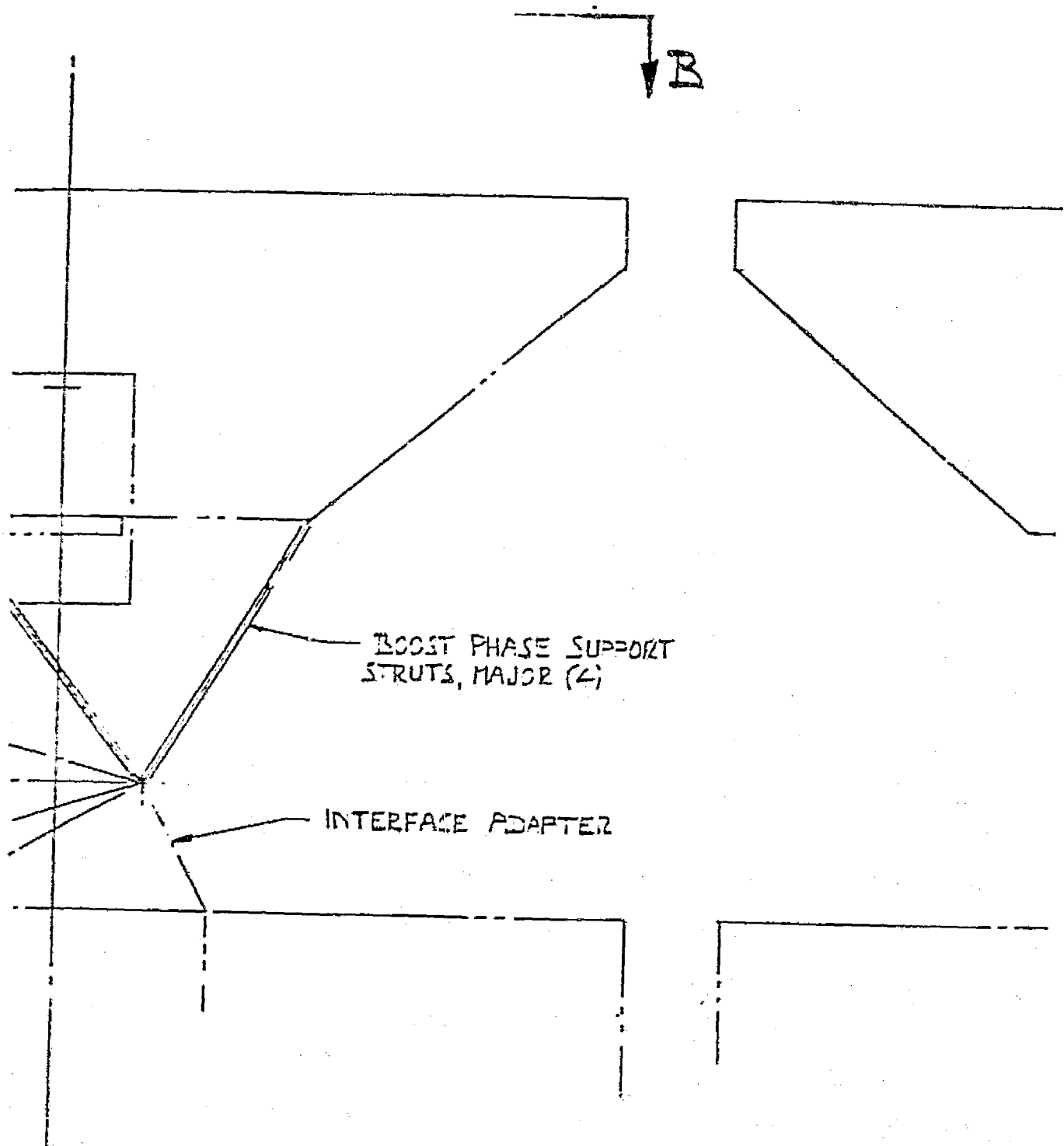
TOWER STRUCTURE, STOWED  
REF

SPACE CRAFT  
ENVELOPE  
REF



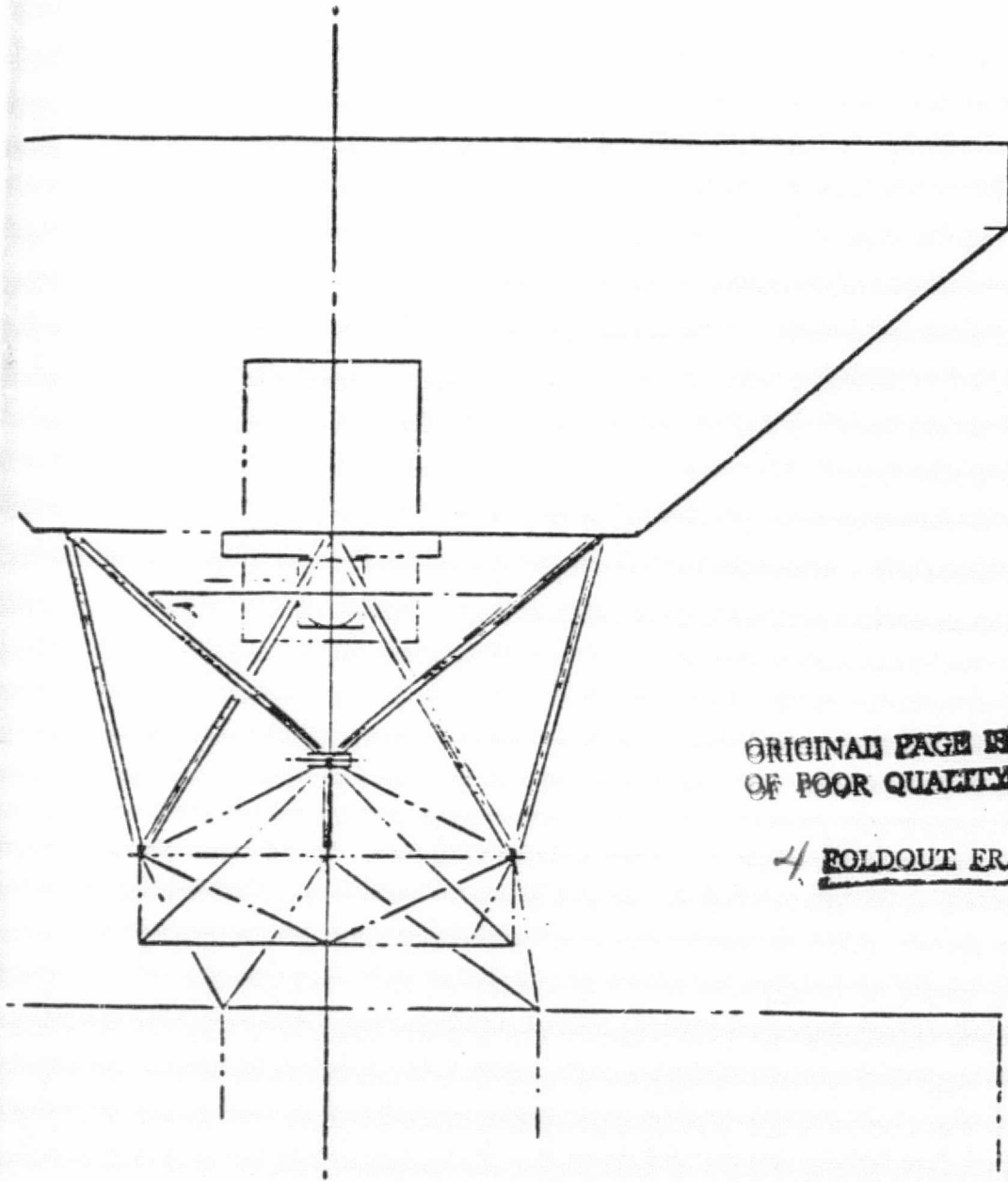
2 BOLTS PER FRAME

ORIGINAL PAGE #  
OF 10 FOR QUALITY



**FOLDOUT FRAME**

**ORIGINAL PAGE IS  
OF POOR QUALITY**



ORIGINAL PAGE IS  
OF POOR QUALITY

4 FOLDOUT FRAME

A-A

PRECEDING PAGE BLANK NOT FILMED

SUPERCEDES SKDVT70922

DESIGN	PRELIMINARY DESIGN DRAWING
DESIGNED BY <i>DH Vaughan 2/5/77</i>	<b>BOOST PHASE SUPPORT STRUCTURE</b> <b>4.4 M ANTENNA SYSTEM</b> <b>STORM SAT.</b>
DATE	
SCALE	
PROJECT	
REVISION	
GENERAL DYNAMICS Corporation Aerospace Division SAN DIEGO CALIFORNIA	14170 SKDV 770930 SHEET 01

Analysis

Antenna Dish. The preliminary stress analysis of the 4.4M MASR antenna has proven the feasibility of successfully meeting the structural performance criteria proposed for the system. The primary areas of consideration for this study are the dynamic and thermal characteristics and the structural integrity of the antenna dish structure and the support tower. Several finite element models using Convair's SOLID SAP program were generated to perform the analyses. Due to budgetary and time constraints simplifications were made to the models wherever possible.

Figure 34 shows an isometric view of the model representing the antenna dish and stiffeners. For this study the ribs and rings are modeled at the shell centerline with their appropriate stiffnesses and areas. The ribs and rings are shown as solid lines in Figure 35, where the membranes

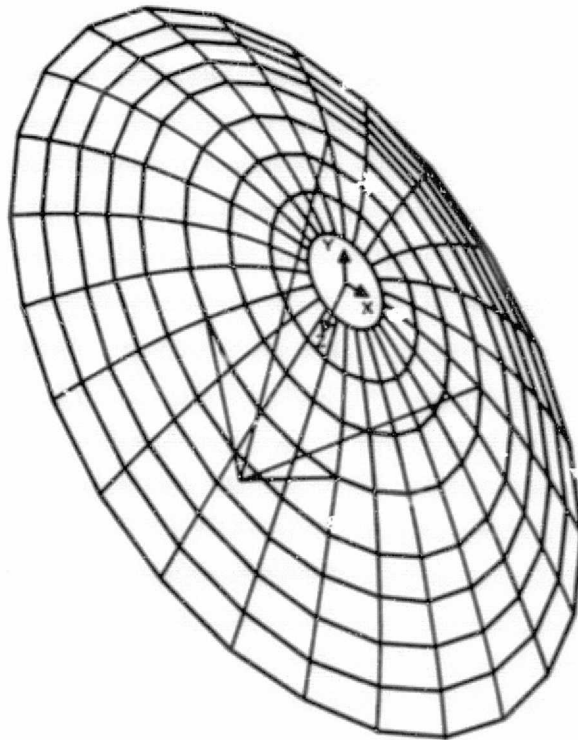


Figure 34. Isometric view of MASR antenna dish.

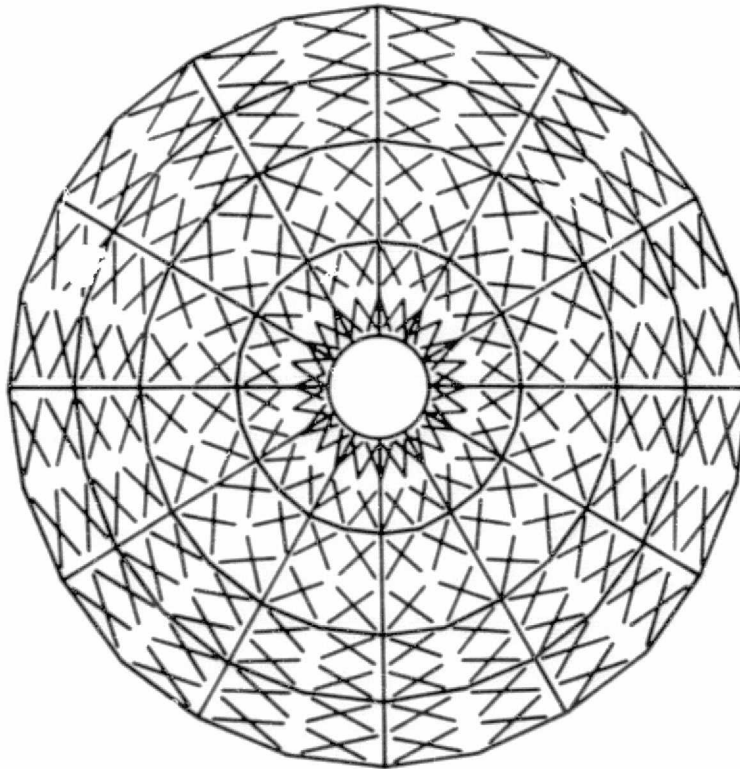


Figure 35. Ribs, rings, and membrane elements in finite element model of dish.

representing the shell are shown as X's. There is an extra node in the middle of each panel defined by two ribs and two rings. Figure 36 shows all of these nodes connected by solid lines.

For this study, the dish shell is modeled with membrane elements with extensional stiffness only rather than bending plates. With only one additional node in the panel bays the bending plates would not add to the refinement of the analysis but would add to the cost of the computer solutions.

The material used throughout the structure in this model is a 6 ply  $(\pm 60, 0)_s$  pseudoisotropic layup of GY-70/X-30 graphite epoxy. The basic material properties used are

$$\begin{aligned}
 E_x = E_y &= 15 \times 10^6 \text{ psi} & \alpha_x = \alpha_y &= -0.168 \times 10^{-6} \text{ in./in./}^\circ\text{F} \\
 G &= 5.67 \times 10^6 \text{ psi} & \rho &= .063 \text{ lb/in.}^3 \\
 \nu &= 0.320
 \end{aligned}$$

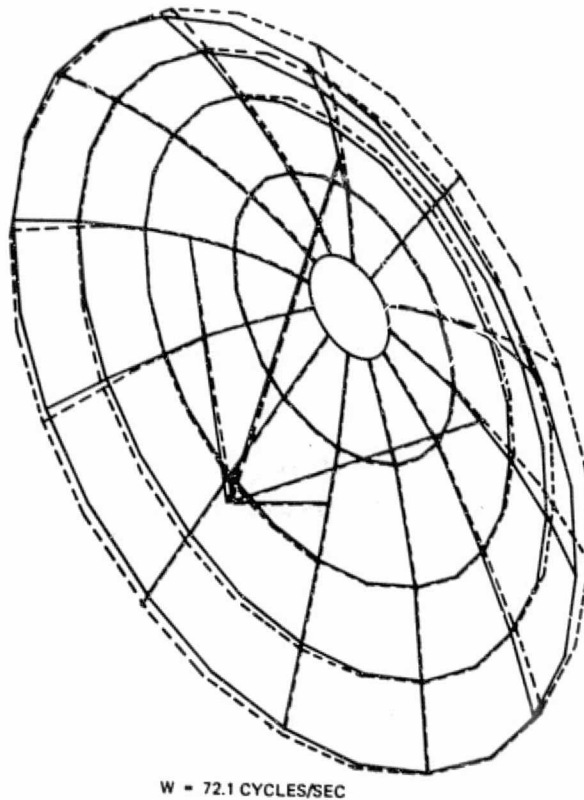


Figure 36. Mode 1 of MASR antenna dish.

where

$E_{x,y}$  = Young's Modulus

$G$  = shear modulus

$\nu$  = Poisson's ratio

$\alpha_{x,y}$  = coefficient of thermal expansion

$\rho$  = specific weight.

This data was generated by Convair's SQ-5 laminate analysis program. These theoretical values compare well with test data except for the coefficients of thermal expansion (CTE).

The values calculated for the Coefficient of Thermal Expansion (CTE) are high compared to test data generated by Convair. More typical values at room temperature are  $\pm 0.03 \times 10^{-6}$  in./in./ $^{\circ}\text{F}$  with  $\pm 0.10 \times 10^{-6}$  in./in./ $^{\circ}\text{F}$  being extreme. A possible explanation for this difference is a variation

in percent fiber volume. Figure 37 shows a plot of CTE for a pseudo-isotropic layup of GY-70/X-30 versus the percent fiber volume. The curve shows that it is theoretically possible to achieve a zero CTE at a fiber percent of 60 percent. Most laminates tested had a percent fiber volume between 63 percent to 67 percent. Using a lower fiber percent would degrade the modulus and strengths of the laminate slightly.

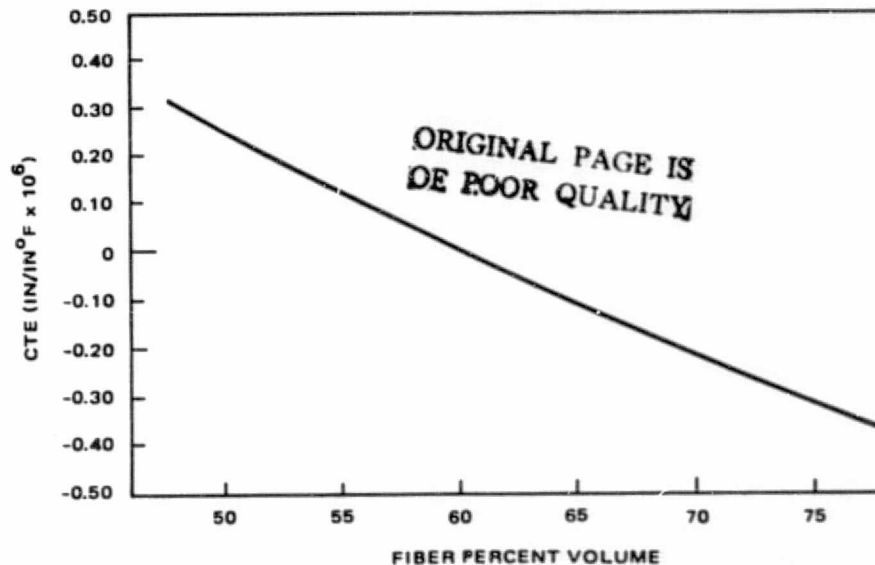


Figure 37. Calculated variation in coefficient of thermal expansion as a function of fiber content for pseudoisotropic GY-70/X-30 (room temperature)

There has been limited testing of GY-70/X-30 to determine the effects on CTE over the extreme temperature ranges being discussed. Most data has been compiled around room temperature. It turns out that the CTE is not constant for the wide temperature range. One test with a pseudoisotropic layup of GY-70/X-30 over a temperature range of  $\pm 320^{\circ}\text{F}$  gave as the highest CTE =  $-0.12 \times 10^{-6}$  in./in./ $^{\circ}\text{F}$  in the  $-150^{\circ}\text{F}$  to  $+75^{\circ}\text{F}$  range. In the  $-150^{\circ}\text{F}$  to  $-320^{\circ}\text{F}$  range the CTE was actually slightly positive. This particular test specimen did not exhibit any microcracking during the thermal cycling. Other tests of GY-70/X-30 laminates have exhibited microcracking and

resulted in  $CTE = -0.5 \times 10^{-6}$  in./in./°F. The microcracking occurred in the first thermal cycle which indicates a possible screening process for manufactured parts.

It is not known what causes microcracking in some laminates and not others. Part of the predesign effort for the MASR antenna should include a materials development program to investigate the correct laminate configuration and makeup to give a near zero CTE without any microcracking.

If it is impossible to prevent microcracking, heaters may be necessary to limit the temperature range in the structure of the antenna. Microcracking does not occur in GY-70/X-30 above  $-150^{\circ}\text{F}$ .

The dynamics model was run separately from the support structure initially to simplify the problem and to obtain a preliminary natural frequency. But since results showed a relatively high natural frequency of the dish compared to the support structure, the two models could be run separately in the future because there would be no coupling of the two structures.

The shell thickness is 0.030 inch. The rings and ribs for this analysis are assumed to be made of "H" sections as shown in Figure 38, which make up the caps and shear members of the frames.

This cross section was proposed for the Convair designed Mariner Jupiter/Saturn 1977 (MJS77) S/X-Band Antenna Subsystem. A typical rib was built utilizing the end bonding and tested assuring its structural integrity.

The density of each beam element in the model is modified to account for material not included in the moment of inertia and area calculations of the beam, i. e., shear members, shell-rib attachments, etc.

The dish is simply supported at three points on the inner ring 120 degrees apart. This provides a kinematic support system for the dish.

The subreflector is modeled as a concentrated mass at the apex of the four support struts shown in Figure 34. The total weight of the assembly is assumed to be 8 pounds with the subreflector itself being half of that total.



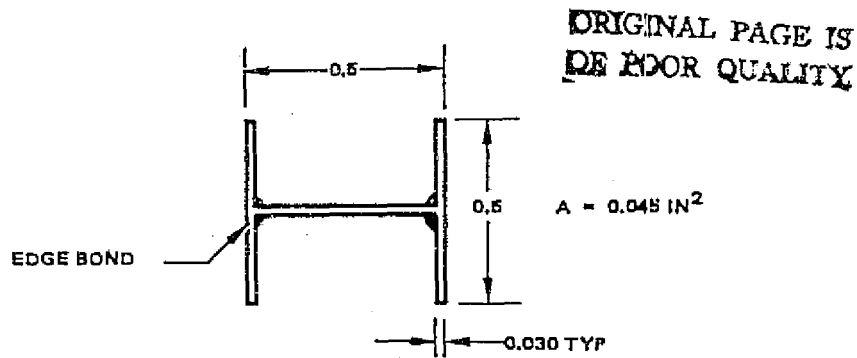


Figure 38. Typical rib and ring element cross section.

The mass of the antenna as computed by the program is 101.8 pounds for the shell, ribs, and frames. This compares to 103 pounds computed by hand. These figures however, do not include such things as the thermal blanket all of which add an additional 30 pounds. Assuming this additional weight is uniformly distributed over the surface the natural frequencies should be reduced by the ratio.

$$\sqrt{\frac{101.8}{133}} = 0.875$$

and are shown in the table of results, Table XVI, in parenthesis.

For the thermal distortion analysis one thermal loading condition is considered that represents the worst thermal gradient over the antenna dish, the sun-on-side condition. The curves below in Figures 39 and 40 showing the gradients versus radius are taken from the thermal analysis of the similar MJS77 12-foot reflector. The sun-on-side condition, even though it has the worst gradients, may not result in the worst RMS surface deflection.\* The temperature distributions shown are "steady state" as if the sun exposure were over an extended period of time and should represent a worse condition

---

\*The gradients over the aluminum subreflector will be less severe due to its greater thermal conductivity.

ORIGINAL PAGE IS  
OF POOR QUALITY

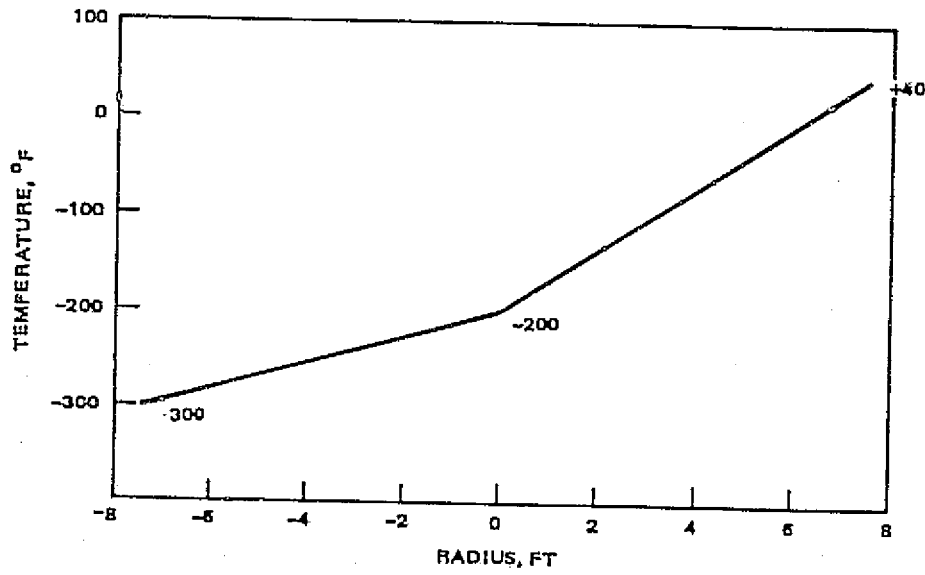


Figure 39. Reflector surface temperature versus radius for a sun-on-side condition.

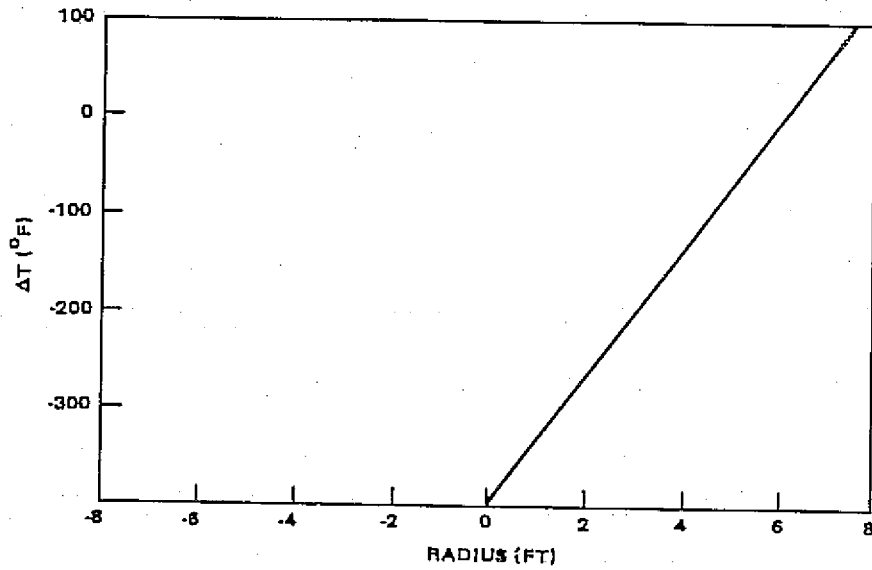


Figure 40. Through the depth temperature gradient versus radius.

than actual operating conditions. For a complete analysis several orientations of the antenna in earth orbit with respect to the sun will be needed. The through the depth gradient is an estimate that should represent a worst case. These two gradients must be added together such that at the extreme edge, closest to the sun, the temperature distribution would be +40 degrees on the skin and 90 degrees on the frame as shown in Figure 41.

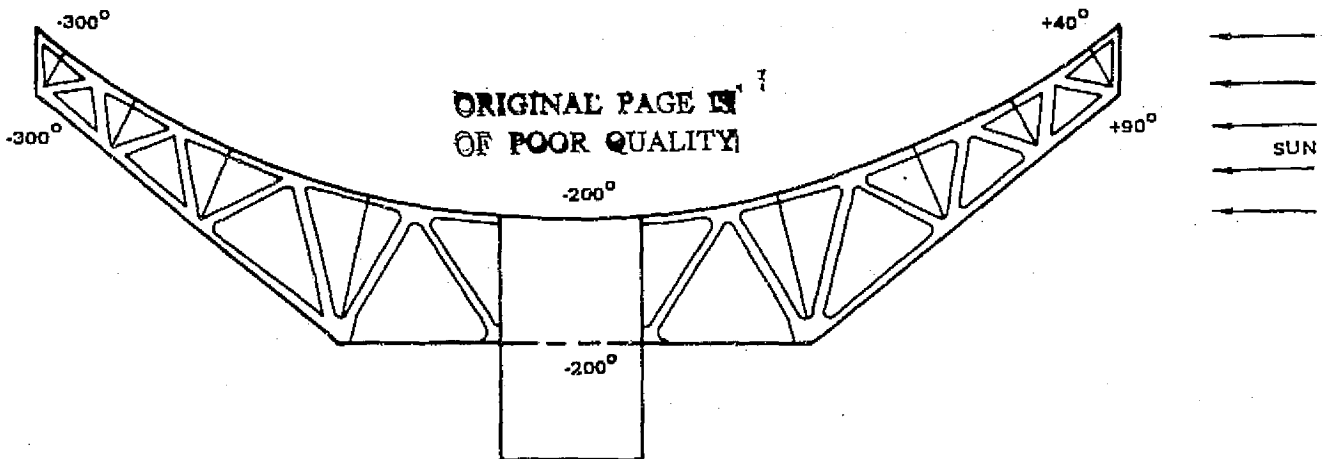


Figure 41. Assumed temperature distribution over antenna structure.

The critical load condition for analysis to ensure the structural integrity of the antenna is the shuttle launch. The load factors shown are from a preliminary document called "Structural Design Criterion for Space Transportation System Payloads." For the final design and analysis, these values must be determined for the actual configuration.

Limit Load Factors for Launch:

$N_x = 4.0$  g's (along axis of shuttle)

$N_y = 5.0$  g's (parallel to shuttle wing axis)

$N_z = 15$  g's (normal to shuttle wing)

The Factor of Safety for launch is 1.40.

The antenna dish is mounted at three points for launch and therefore can be considered as a rigid body with respect to the launch support structure (Drawing No. SKDV770930). The support struts are modeled as boundary elements (springs). Since the two dimensional frames are modeled as one dimensional beams on the shell centerline the resulting moments, axial loads and shears must be resolved into cap loads.

### Antenna Dish Results

The DYNAMICS analysis of the antenna dish yielded the natural frequencies and mode shapes shown in Table XVI.

TABLE XVI. NATURAL FREQUENCIES AND MODE SHAPES

Mode Number	Frequency (cycles/sec)	Mode Shape
1	82.4 (72.1)*	Astimagtic
2	83.2 (72.8)	Astimagtic
3	99.1 (86.7)	Spherical
4	108.9 (95.3)	
5	140.1 (122.5)	

\*Values in parentheses are reduced due to increase in mass.

The graphics plot of the first mode shape is shown in Figure 37.

The lowest natural frequency for the longest truss member in the dish backup structure assuming simply supported boundary conditions is 72.4 cycles/sec.

### Surface Distortion

The finite element solution for the antenna dish thermal distortion analysis was run with a CTE =  $-0.168 \times 10^{-6}$  in./in./°F. This value as stated earlier is a theoretical value and is not representative of test data. The correct value for CTE to use in the temperature range for MASR must still be determined by further tests. This testing must also include developing

a laminate that does not exhibit microcracking in order to meet the 1.0 mil RMS surface distortion budgeted for thermal distortion. Therefore for the present the results in Table XVII are shown for a CTE =  $-0.168 \times 10^{-6}$  in./in./°F which should be conservative. The results are linear with CTE. The largest CTE allowable and still be able to meet the 1.0 mil RMS is  $-0.350 \times 10^{-6}$  in./in./°F.

The C terms in Table XVII are the displacements of vertex of the antenna along its three axes (see Figure 34), plus two rotations about the axes. The sixth term is the change in focal length. These terms describe the pointing error of the antenna.

TABLE XVII. RESULTS OF SURFACE RMS ANALYSIS

LOAD CONDITION	$C_1 - \Delta X$ IN $\times 10^3$	$C_2 - \Delta Y$ IN $\times 10^3$	$C_3 - \Delta Z$ IN $\times 10^3$	$C_4 - \Delta \theta_x$ RAD $\times 10^6$	$C_5 - \Delta \theta_y$ RAD $\times 10^6$	$C_6 - \Delta F$ IN $\times 10^3$	RMS IN $\times 10^3$	RMSH IN $\times 10^3$
SURFACE TEMP. DIST.	-0.773	0.058	-0.504	0.395	5.326	1.612	0.339	0.332
$\Delta T$ THRU RIBS	2.296	0.000	-0.122	0.000	-12.743	-0.346	0.209	0.195
TOTAL TEMP. DIST.	1.522	0.058	-0.626	0.395	-7.417	-1.066	0.479	0.464
IG STATIC	5.063	-0.114	0.000	0.024	49.284	0.000	0.060	0.056

The gain of the antenna is a function of the surface RMS about the best fit paraboloid and is independent of the C terms. The RMS surface distortion is one part of the total RSS surface distortion where only if the largest displacement due to thermal distortion occurred say at the same location as the largest distortion due to manufacturing tolerance would their RMS be added directly. It is accepted practice to RSS the individual RMS values of an antenna.

The values in the table are:

$C(6)$  = best fit displacements (3), rotations (2) and change in focal length of dish

RMS = RMS normal error

RMSH = RMS half path length error

### Subreflector Displacement

Table XVIII gives the subreflector's displacements relative to its original position under no load. The values shown are for a material CTE =  $-0.168 \times 10^{-6}$  in./in./°F. The results are linear with respect to CTE.

TABLE XVIII. SUBREFLECTOR DISPLACEMENTS  
FOR THERMAL CONDITION

Load Condition	$\Delta Y$ $\times 10^3$ Inch	$\Delta X$ $\times 10^3$ Inch	$\Delta X + \Delta Y$ $\times 10^3$ Inch	$\Delta Z$ $\times 10^3$ Inch
Surface Temp. Dist.	0.608	0.000	0.608	-0.008
$\Delta T$ Thru Ribs	-0.014	0.000	-0.014	-0.002
Total Temp. Dist.	0.594	0.000	0.594	-0.010
1G Static	1.313	0.120	1.318	0.155

### Structural Integrity

For the launch condition the structural element in the backup structure with the lowest Margin of Safety is a shear carrying diagonal member in the circumferential ring located at the radius of the three pickup points of the launch support structure. The limit load is 165 pounds and the allowable load as a simple supported column is 233 pounds. So

$$M.S. = \frac{233}{165(1.40)} - 1 = \underline{+0.01 \text{ (ult)}}$$

The next highest margin calculated is in a diagonal of a rib.

$$M.S. = \frac{287}{165(1.40)} - 1 = \underline{+0.24 \text{ (ult)}}$$

### Shell Membranes

The 0.030 shell portion of the antenna should not buckle during launch to preclude cracking of the coating, separation at a bondline between the shell and stiffeners, and any permanent wrinkles. A factor of safety on limit loads of 1.15 is advisable using the buckling failure load as the allowable stress.

The overall stress level in the shell is low for the launch condition except near the points of support structure attachment. In these regions local stiffening may be required.

The more detailed model of the antenna structure which properly accounts for the depth of the backup structure will be needed to determine the shell load intensities.

For a detailed analysis of the reflector, the model shall have sufficient nodes to allow definition of the shell panel as offset from the rings and ribs, the truss arrangement of the backup structure, the subreflector support, the barrel, and mounting structure to the gimbaling system. Whereas the model for the preliminary analysis, Figure 34 is a full 360 degrees model, a half model utilizing symmetry would be sufficient for the detailed analysis.

The half model for a dynamics analysis would require runs with both symmetric and antisymmetric boundary conditions. Because of the need for a greater number of nodes than is practical in the larger model, a small model of an individual shell panel will be required to include the effects of "oil canning" thermal distortion. The distortions will be a small fraction of a mil because the thickness is small and little bending will occur.

### Deployable Support Frame

The support structure for the antenna during in-orbit operation is modeled separately from the dish. The two models can be analyzed separately because the natural frequencies are widely enough spaced that there will be no coupling. The mass and the mass moments of inertia of moving portion of the antenna structure are modeled as a lump mass at the

components' center of gravity. This eliminates the problems of cross coupling terms of translation and rotation. The mass properties are listed below:

$$W_t = 173 \text{ pounds}$$

$$I_{\text{roll}} = 395672 \text{ lb-in.}^2$$

$$I_{\text{pitch/yaw}} = 271285 \text{ lb-in.}^2$$

The center of gravity, CG, is located 2.7 inches in front of the reflector surface. Figure 42 shows the finite element model for the support structure.

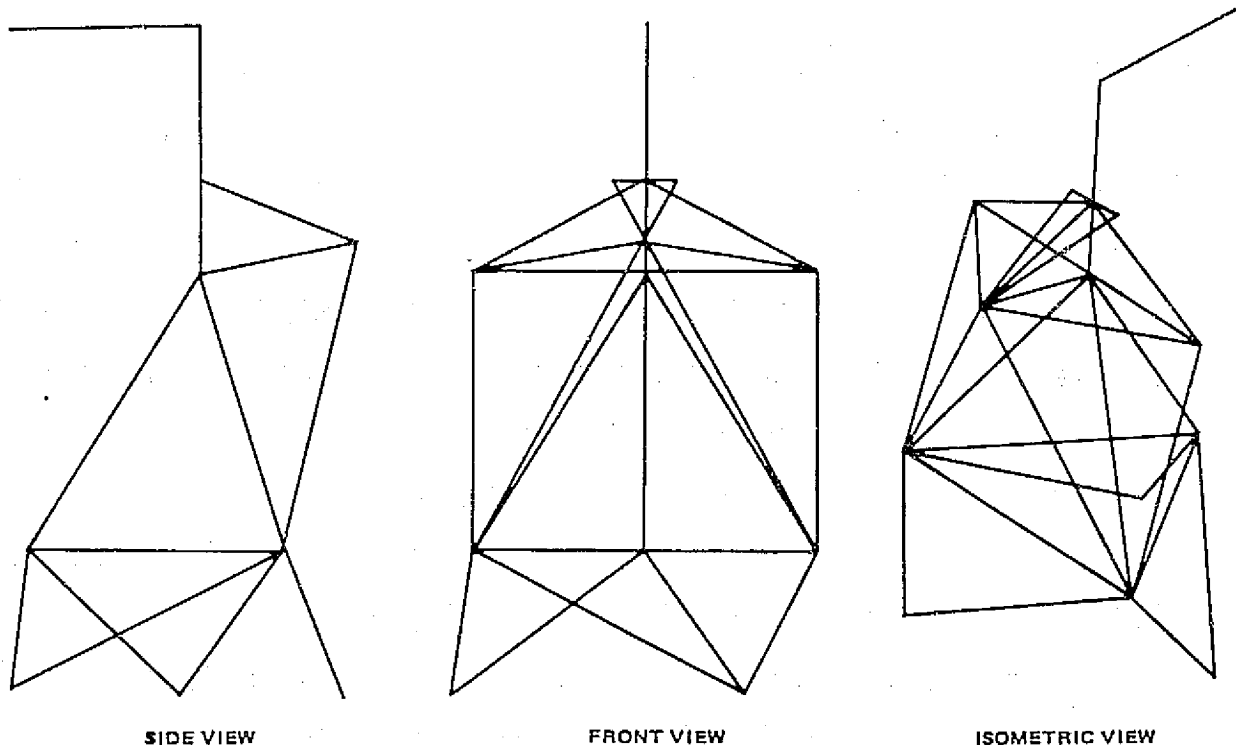


Figure 42. Finite element model of deployable support frame.

All members of the frame structure are modeled as pin-ended elements except for a few in the upper portion of the model that are modeled as beams in order to transfer the mass terms of the concentrated mass representing the antenna into the truss members.



The material assumed for the tubes is a nearly all unidirectional GY-70/X-30 graphite epoxy. A thin glass fabric, such as 120, is used to give the laminate some cross ply strength. The net longitudinal modulus will be around  $35 \times 10^6$  psi where the unidirectional modulus of GY-70/X-30 is around  $42.5 \times 10^6$  psi.

The density of the material is increased by 30 percent for the end fittings. The design details of the end fittings will be simplified because the load levels in the tubes will be low during normal operation. A separate launch support structure handles the shuttle launch accelerations.

The important structural parameter for the tubes in the support frame is their AE, area times modulus of elasticity. The CTE of the material should not be a concern because the temperature can be monitored and the control system for the antenna should be able to correct for any resulting errors in pointing due to thermal distortions of the deployable support frame by using predictions of verified mathematical models.

The cross sectional areas of the various members of the frame shown below are those which give the results presented. (Ref Dwg. No: SKDV770927)

Interface Adapter	$A = 0.565 \text{ in.}^2$
Actuator Strut	$A = 1.131 \text{ in.}^2$
Lower Truss Members	$A = 0.565 \text{ in.}^2$
Upper Truss Members	$A = 0.754 \text{ in.}^2$

A Convair program called FADSTOP can be used to direct the optimization of a structure with respect to frequency and deflection constraints for rods, beams, and membranes. The program indicates how to reduce the weight of a nonoptimum structure while maintaining the desired structural performance constraint. FADSTOP can also direct the stiffening of a structure to increase the performance for minimum weight. FADSTOP uses the deflection file from a SOLID SAP finite element solution.

The math model of the support frame structure does not include the flexibilities of the gimbal system. Including the gimbal system would greatly complicate the model. Figure 43 indicates a possible approach to modeling the bearings, housing, and shaft stiffnesses.

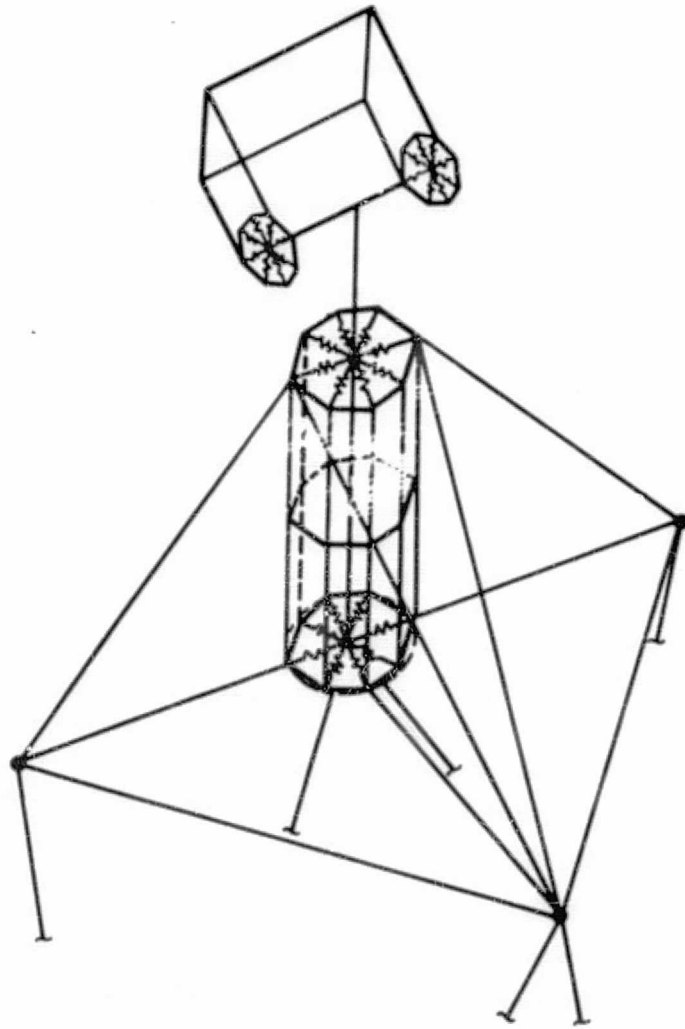


Figure 43. Possible bearing/gimbal model.

### Deployable Support Frame Results

The current model of the support frame structure as described weighs 43 pounds and has a natural frequency of 29.5 cycles/sec. Figure 44 shows the first mode of the support structure. Table XIX lists the five lowest natural frequencies.

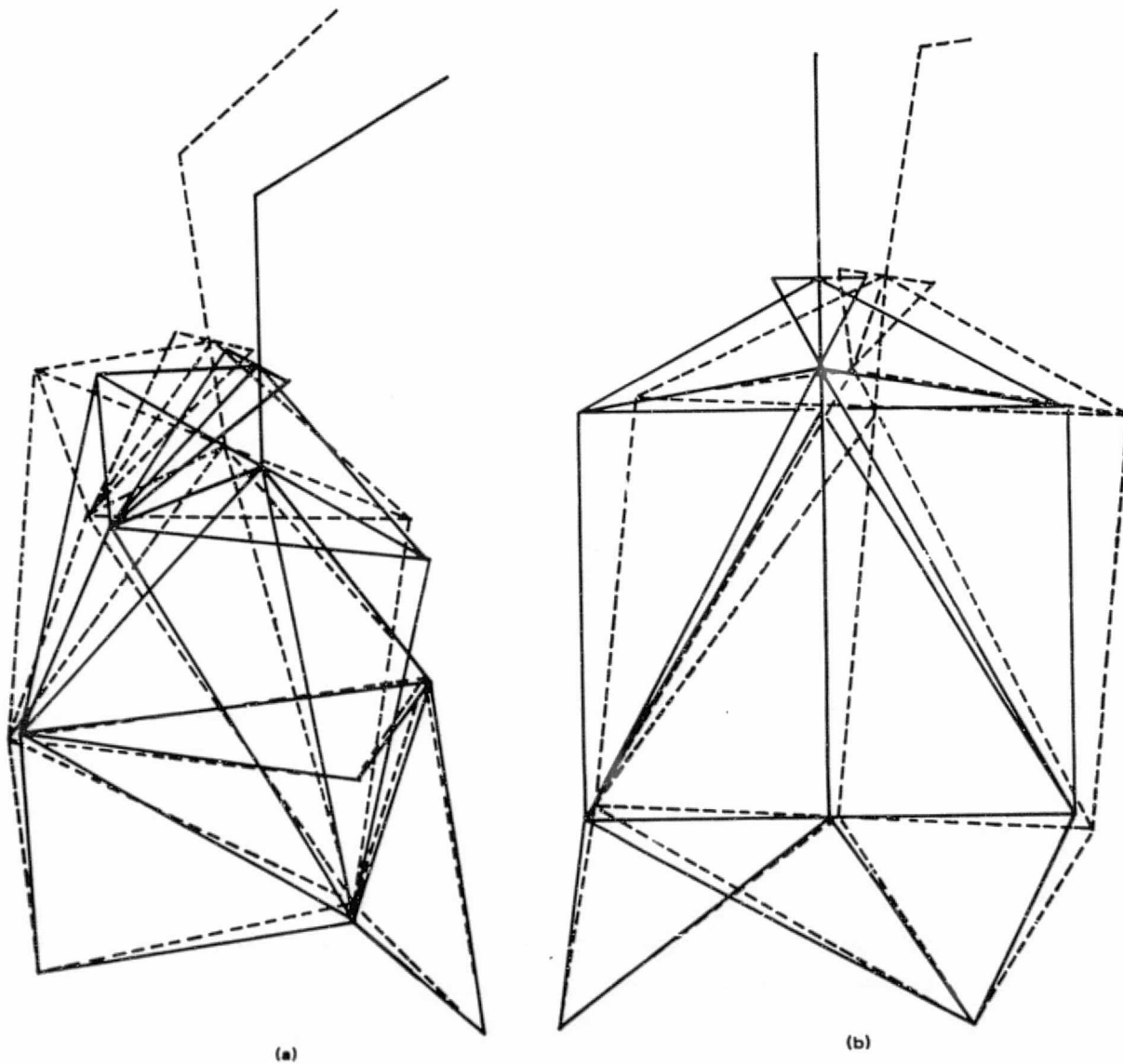


Figure 44. First mode shape of deployable support frame,  
 $\omega_1 = 29.5$  Hz.

TABLE XIX. NATURAL FREQUENCIES OF THE DEPLOYABLE SUPPORT FRAME

Mode	Frequency Hz
1	29.5
2	31.5
3	42.1
4	66.3
5	79.1

Launch Support Structure

Figure 45 shows a sketch of the launch support structure finite element model. Each element in the model is identified by an adjacent

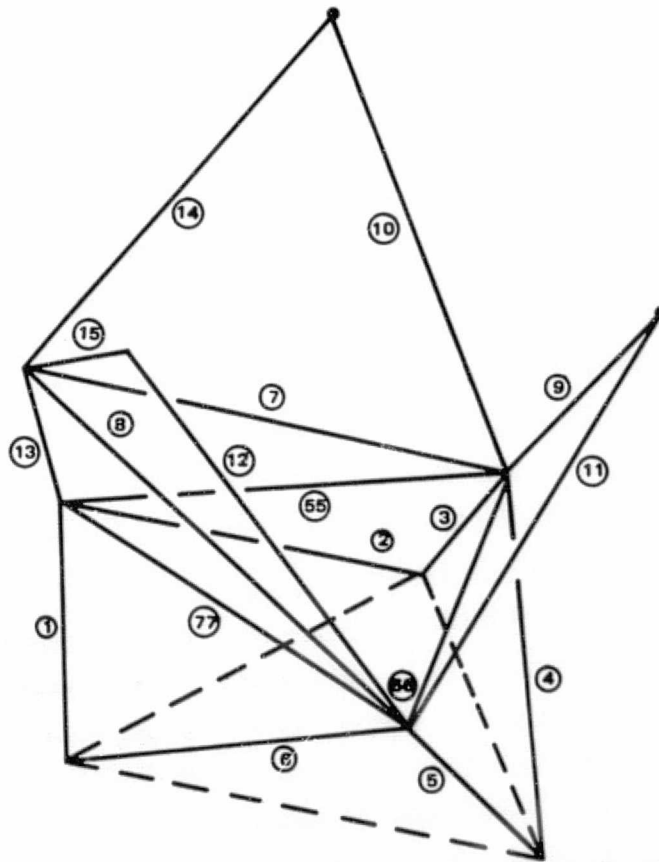


Figure 45. Launch support structure finite element model.

number. The mass and its CG location are located by "dummy" structure, not shown, on top of the three antenna support points. In the launch configuration the antenna is rotated 90° by "breaking" the in-orbit support structure and supporting the antenna dish by the launch support struts, elements 9 through 15.

The material for the launch support struts is the same as the in-orbit support structure, GY-70/X-30 with some glass giving a modulus of around  $35 \times 10^6$  psi.

In the adapter the elements are principally designed for stiffness, i. e., AE, to provide a 15 Hz system. The cross sectional area is 0.565 in.<sup>2</sup>. At this level of effort all tubes are assumed the same even though the loads and lengths are different. For weight efficient joint design, the smallest practical tube diameter is advantageous. The tubes can be made with a 1.0-inch diameter and a wall thickness of 0.18-inch. The launch support struts are sized to have a cross sectional area of 0.22 in.<sup>2</sup>, a diameter of 1.0-inch, and a wall thickness of 0.070-inch.

#### Support Structure Results

In the transition adapter the critical tube is element No. 66,  $l = 47.5$  inches and a limit design load of -3346 pounds. The Margin of Safety for Euler Buckling is

$$M.S. = \frac{10824}{3346(1.40)} - 1 = \underline{+1.31 \text{ (ult)}}$$

The critical element in the launch support struts is No. 10. The length is 55.6 inches with a limit compressive load of 2195 pounds. The tube is sized for a zero margin for Euler Buckling. The natural frequency of the tube is 70 cycles/sec. The weight of the six tubes and fittings is about 8 pounds.

### Special Study Areas

As part of this study, specific areas relating to feasibility of manufacturing a large 4.4 meter reflector dish have been studied. This section is included to elaborate more fully on such items as:

1. Surface contour - RMS attainment
2. Adjustment loads in dish
3. Identified future development areas

#### Surface Contour - RMS Attainment

GD/C has studied the requirement for achieving an accuracy of 1.7 mils rms on the operational reflector surface and considers it feasible using proprietary design, tooling, and fabrication steps.

#### Calculated Total RMS and Error Budget (mils)

Tool Manufacturing rms		1.2 = T <sub>1</sub>
PDMO	1.0	
Measurement Error	<u>.2</u>	
Surface Adjustment Error		.2 = T <sub>2</sub>
Thermal Distortion		.479 = T <sub>3</sub>
Subreflector		0.30 = T <sub>4</sub>
1 G Sag (max condition)		0.06 = T <sub>5</sub>
Slew Error		<u>0.01 = T<sub>6</sub></u>
Total rms = T	$= \sqrt{T_1^2 + T_2^2 + T_3^2 + T_4^2 + T_5^2 + T_6^2}$	= 1.34

The effects of moisture are not included because of uncertainties in computation of their effect on surface rms. An error budget entry of 1.04 rms for moisture effects can be tolerated without the total surface rms exceeding 1.7 rms.

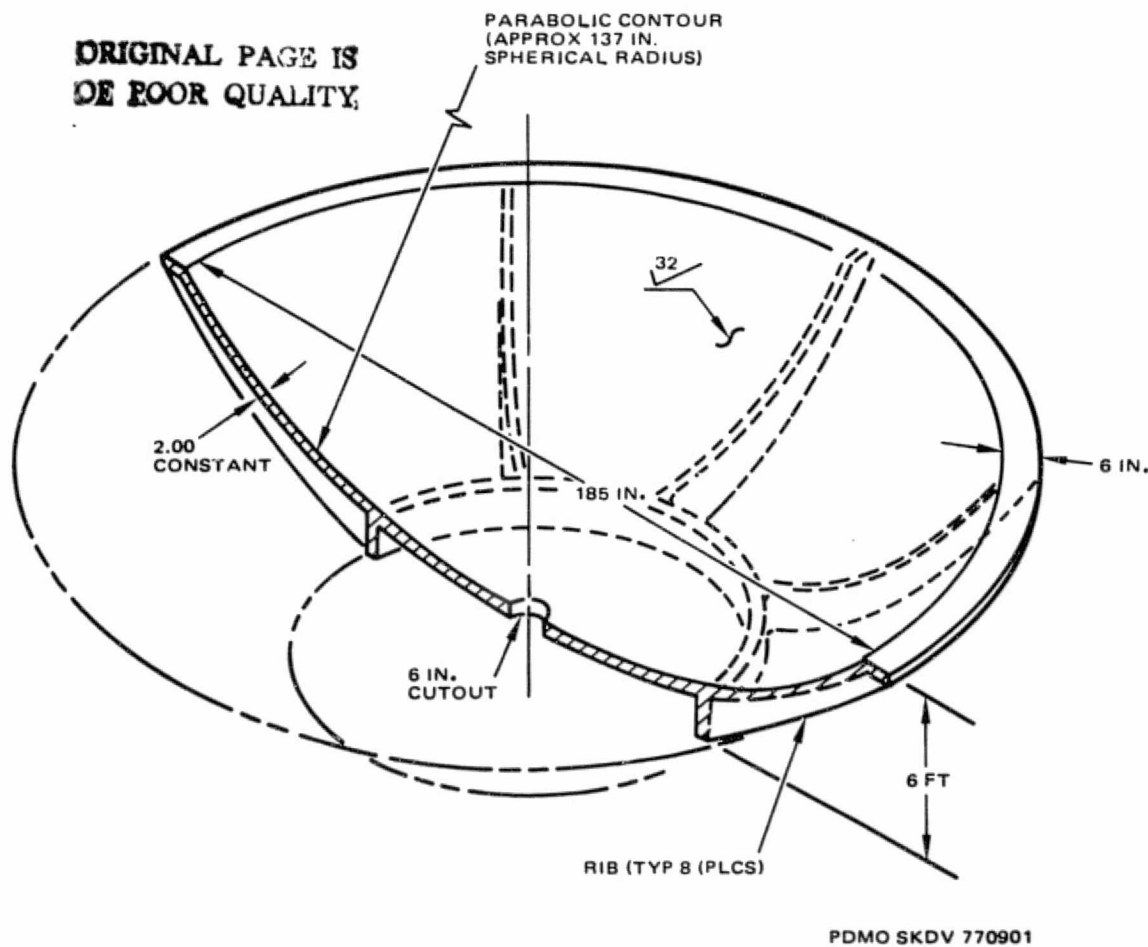


Figure 46. PDMO for 4.4 M MASR antenna.

#### Surface Adjustment Loads

The loads that will be imposed on the structure of the antenna will be small due to any micrometer adjustment of the surface. Because the surface of the reflector is manufactured to the 1.0 mil rms requirement any adjustment that may be necessary by definition must be small. To determine an order of magnitude of an applied load, a shallow spherical shell with a point load was considered (Ref. Theory of Plates and Shells,

Timoshenko and Woinowsky - Krieger, Second Edition, McGraw-Hill, 1959, New York, p. 561). The deflection,  $w_0$ , is given by the following expression.

$$w_0 = \frac{\sqrt{3(1-\nu^2)}}{4} \frac{Pa}{Eh^2}$$

where

- P = Force in pounds
- E =  $15 \times 10^6$  psi = Young's modulus
- h = 0.030 in. = shell thickness
- a = 120 in. = diameter
- $\nu$  = 0.32 = Poisson's ratio

Assume a displacement of 0.002 inch. The resulting force is P = 0.548 pound.

The resulting membrane stresses at the point of load application are:

$$\sigma_r = \sigma_\theta = 126 \text{ psi}$$

In fact the type of surface corrections to be made are astigmatic in nature which occur upon removal of the unstiffened reflector from the tool. The forces required to correct the entire surface in a uniform manner are significantly less than the forces required for a local aberration. Thus the stresses to be encountered during adjustment will be very low and below the Precision Elastic Limit strength of 10,000 psi for the GY-70 X-30 material.

## 2.7 MASR GIMBAL DESIGN

### 2.7.1 Gimbal Requirements

Identical gimbals will be utilized to provide pitch and roll scanning of the 4.4 meter Microwave radiometer Antenna (MASR). The scan requirements, Table XX, are accomplished by a closed loop drive system utilizing a limited rotation, brushless DC torque motor controlled by a dual speed



TABLE XX. BASIC GIMBAL REQUIREMENTS

<u>MASR Antenna</u>	
Diameter	4.4 meters (15 feet)
Weight	173 pounds
$I_{\text{Roll}}$ (about gimbal axis)	107 slug-ft <sup>2</sup>
$I_{\text{Pitch}}$ (about gimbal axis)	90 slug-ft <sup>2</sup>
$I_{\text{Yaw}}$ (about gimbal axis)	68 slug-ft <sup>2</sup>
<u>Gimbal</u>	
Travel - each axis	$\pm 10^\circ$ (primary calibration) 21 mr scanning raster
Scanning and slewing rate	350 $\mu\text{r}/\text{sec}$ 1-10 sec for line reversing and indexing
Line-to-line stability	45 $\mu\text{r}$ (0.1 beamwidth)
Frame-to-frame stability	145 $\mu\text{r}$ (0.3 beamwidth)

(72:1) resolver. The 21 mrad square frame pattern is depicted in Figure 47. Line scan is continuous,  $\omega = 350 \mu\text{rad}/\text{sec}$ , so that the dwell integration time exceeds one second per beamwidth. The resolver readout establishes the frame boundaries for line scan and indexing. The optimum rate profiles to be implemented are shown in Figure 48. Once the edge of the frame is reached, a programmed profile of rate commands each torque motor simultaneously to reverse the antenna scan direction and index to the next line.

Although the angular accelerations required are very small, the large inertia of the MASR makes its motions critical to the pointing of the AASIR on the main body. This momentum compensation will be implemented by torquing the ACS momentum wheel directly in synch with the gimbal acceleration commands as proposed in the STORMSAT Final Report.

ORIGINAL PAGE IS  
OF POOR QUALITY

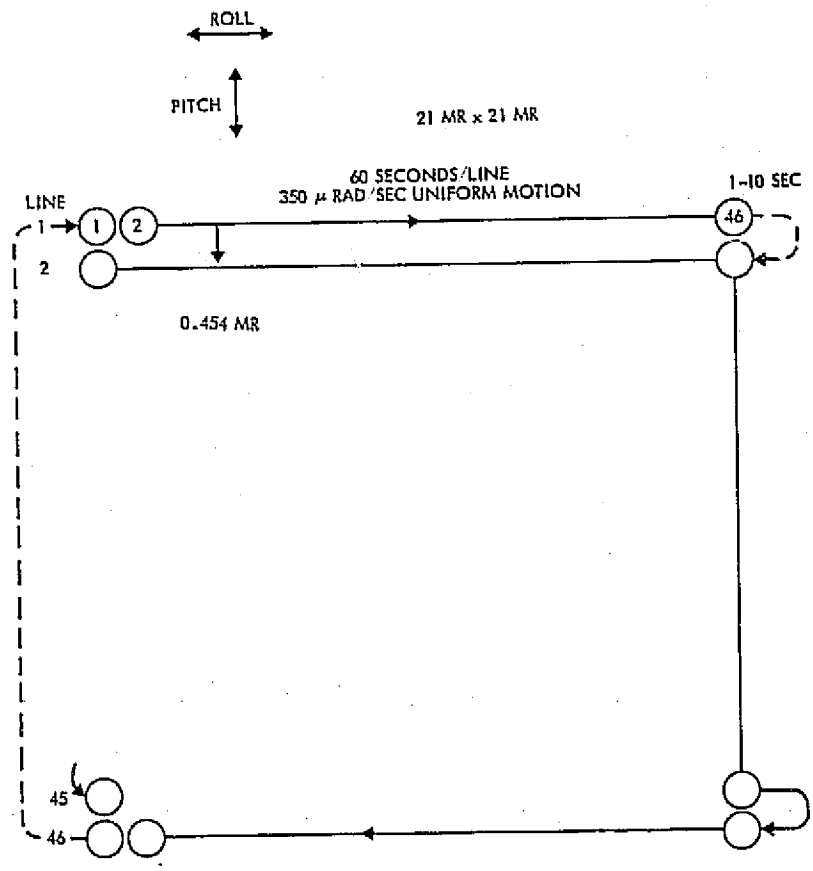
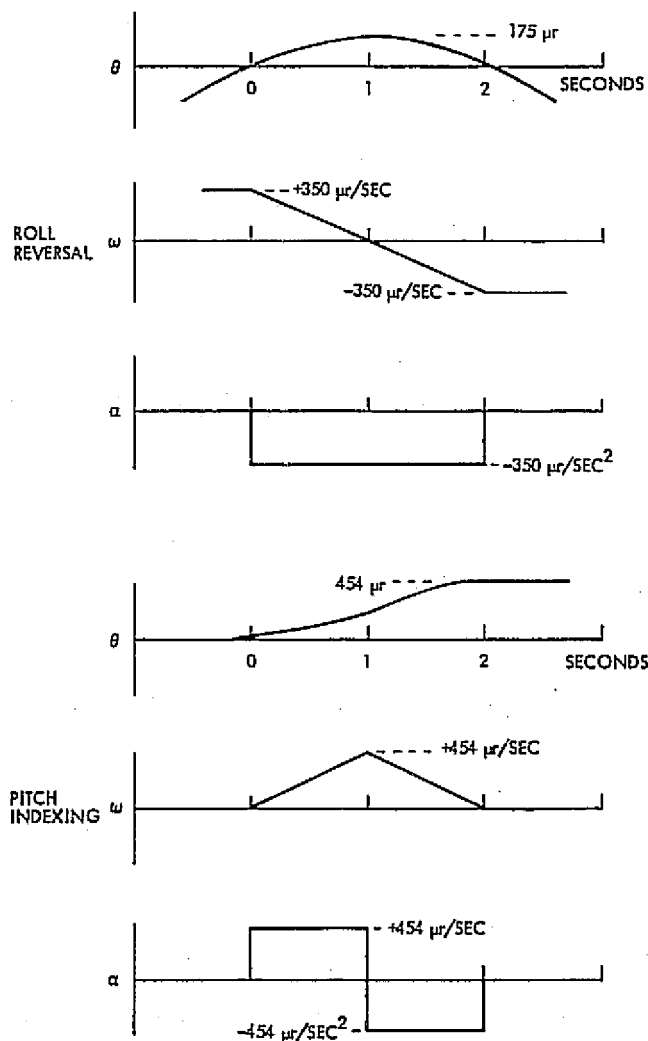


Figure 47. Standard frame.



ORIGINAL PAGE IS  
OF POOR QUALITY

Figure 48. Command profiles for line indexing and reversals.

### 2.7.2 Mechanism Description

The general configuration of the selected mechanism is shown in Figure 49 with overall dimensions as illustrated in that figure. The mechanism employs pitch and roll axes designs that are identical with respect to housing, shaft, installation of components, etc. Attachment of the pitch axis housing to the roll axis shaft is accomplished by a simple adaptor yoke. The common design approach reduces the design/drafting task to one-half and further reduces the effort required for thermal, dynamic, and stress analysis of the gimbal system. A decrease in fabrication and assembly cost can also be realized by the similarity between axes and the use of common assembly fixtures for each.

ORIGINAL PAGE IN  
OF CASE NUMBER

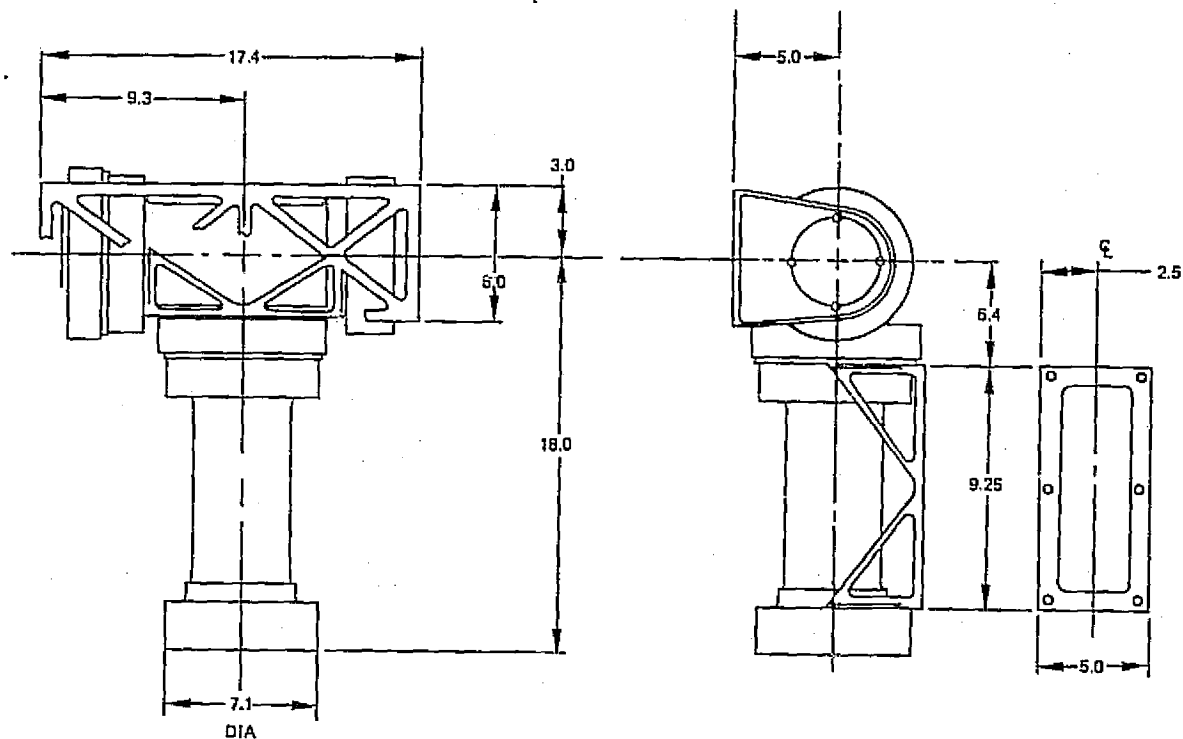


Figure 49. Maser gimbal dimensions in inches.

A summary of the materials, lubrication and components selected for the baseline design is presented in Table XXI. The anticipated weight breakdown is shown in Table XXII.

### 2.7.3 Component Selection

The design presented emphasizes low cost and high reliability. Weight and power, although considered in all tradeoff exercises, were secondary factors in the selection process. The basic approach to satisfy the low cost, high reliability goals was to emphasize:

- simplicity
- minimum development effort
- use of existing Hughes technology

TABLE XXI. COMPONENTS

Torquer

Type: Limited rotation, dual winding, brushless, DC  
Mfg: Sperry Rand Corporation, Durham, NC  
Hughes Part No.: 258074  
Weight: 8.9 pounds  
Peak Torque: 120 in-oz/winding over  $\pm 45$  degree range  
Stall Power: 51 watts

Resolver

Type: Dual Speed - 72:1  
Mfg.: American Electronics Inc (87PX1)  
Hughes Part No. 258073  
Weight: 3.9 pounds  
Accuracy: Single speed - 60 arcminutes  
              72 speed       - 10 arcseconds  
              Repeatability - 4 arcseconds  
Input Power: 0.1 watts

Bearings

Type: Angular Contact, Separable  
Mfg.: Barden Corporation, Danbury Conn. (S114BX1)  
Hughes Part No.: 258083  
Weight: 1.4 pounds  
Size: 70 mm I.D., 110 mm O.D, 20 mm wide  
Material: 440C per QQ-S-763

TABLE XXII. MASR - STORMSAT GIMBAL  
WEIGHT ESTIMATE

Housings (2)	7.4 pounds
Shafts (2)	2.8
Load Yoke	1.0
Inter Gimbal Yoke	0.7
Interface Yoke	0.9
Torquers (2)	17.8
Resolvers (2)	7.8
Bearings (4)	5.6
Spring Assemblies (2)	2.0
Hardware (miscellaneous)	0.5
Wiring Guides plus Harness	2.0
Miscellaneous	<u>0.5</u>
Unit Weight	49.0 pounds

#### 2.7.3.1 Torquer

The limited rotation, dual windings, brushless DC torque motor was selected over the stepper motor/gear box approach due to its simplicity and smoothness of drive features. The elimination of both the stepper impulses and gear drive harmonics improves antenna pointing stability and reduces the spacecraft stability analysis to simple gross reaction torques. The limited rotation torquer was selected over the full rotation units to take advantage of simplified drive electronics. The increased weight and power requirements of the limited rotation torquers is offset by simplicity and higher reliability of its electronics. Both the torquer and drive electronics have been developed, fabricated and qualified for a military space program.

#### 2.7.3.2 Position Transducer

The 72:1 dual speed, brushless resolver has an accuracy of 10 arcseconds with repeatability of 4 arcseconds. Both the resolver and processing electronics have been designed and qualified for the previously

mentioned military space program. Important considerations justifying the selection of the resolver include the following:

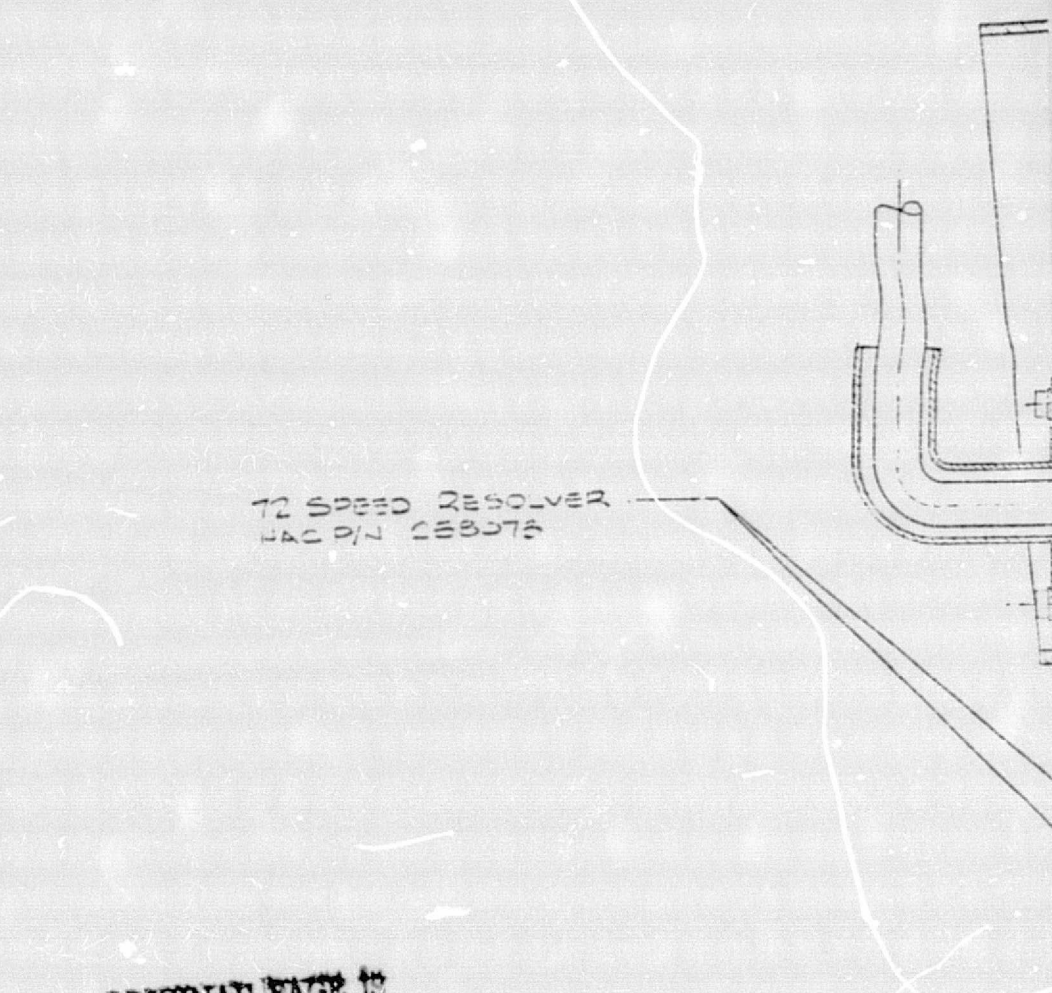
- Brushless characteristics offer friction-free operation.
- Absence of brushes, optical devices and other wearout components provide unlimited life capability.
- Input power required is very low.
- Large temperature extremes are permissible without significant changes in accuracy.
- Highly reliable because of low probability failure modes of wire windings.

In arriving at the resolver choice, several other angular position devices were considered. They include

- single speed resolvers
- magnetic core V-scan devices
- brush-type encoders
- optical encoders
- variable inductance encoders (inductosyn)

#### 2.7.3.2 Bearing and Lubrication Configuration

The installation of the bearings as proposed for both axes is shown in Figure 50. The 10-inch spacing between the 70 mm I.D. angular contact bearings is provided to minimize errors due to runout and maximize gimbal stiffness. The inner and outer races of one bearing are fixed relative to housing and shaft. For the opposing bearing, the inner race is clamped to the shaft while the outer race is connected to the housing by means of a diaphragm-type double flexure spring. The radially stiff but axially soft spring eliminates radial clearances, provides rotational stiffness, and permits axial compliance. The axial compliance is necessary to prevent undesirable buildup of bearing preload, stress and friction due to thermal differential expansion effects. The use of angular contact bearings throughout also negates any effect of thermal differential expansion in the radial direction of the housing and shaft. In order to minimize costs and development, the same bearings and steel preload springs as used on previously qualified and orbited precision despun assemblies, such as GMS, will be employed.



72 SPEED RESOLVER  
HAC P/N 283078

ORIGINAL PAGE 13  
OF POOR QUALITY

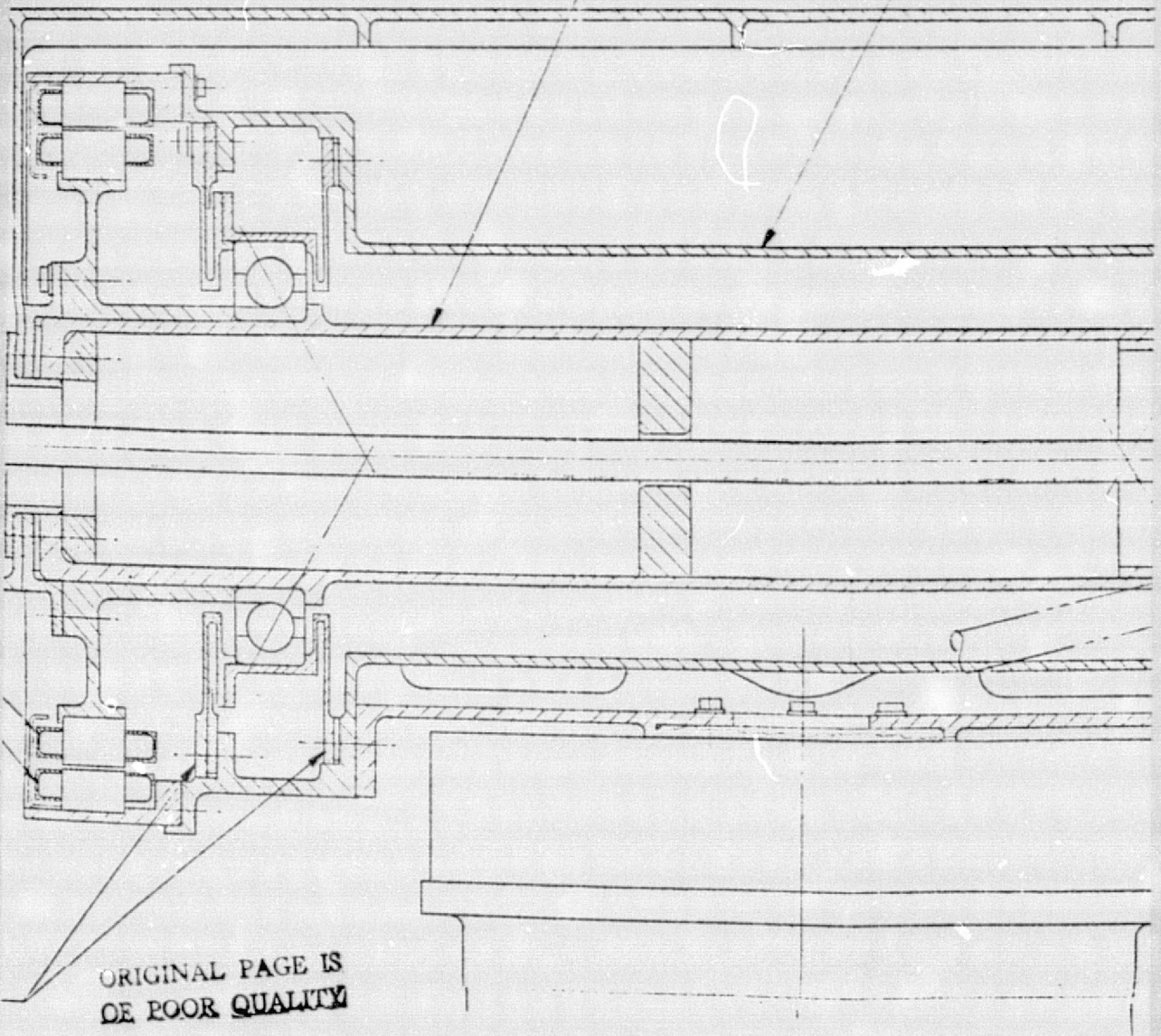
WELDOUT FRAME

BEARING PRELOAD -  
SPRING ASSEMBLY  
HAC P/N 3377060  
PRELOAD 50 LBS



SHAFT, BERYLLIUM  
SIMILAR TO HAC P/N 33770

HOUSING, B  
SIMILAR TO



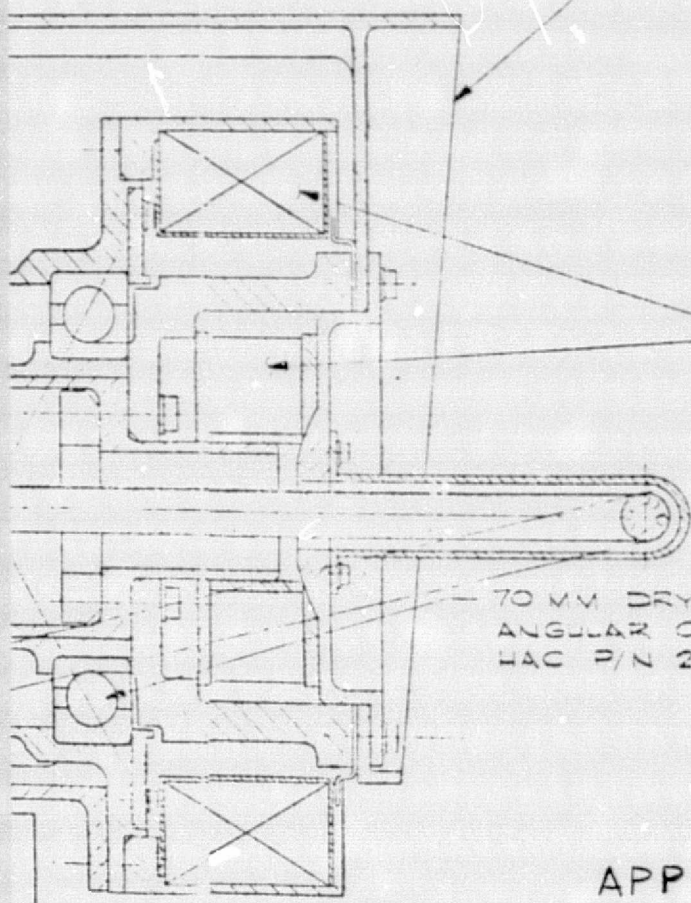
ORIGINAL PAGE IS  
OF POOR QUALITY

2 FOLDOUT FRAME

DI

BERYLLIUM  
HAC P/N 3317005

LOAD YOKE  
BERYLLIUM



1 FT LB BRUSHLESS  
MOTOR ASSY  
HAC P/N 258074

70 MM DRY LUBED  
ANGULAR CONTACT BEARING  
HAC P/N 258083

APPROX 2/3 SCALE

**ORIGINAL PAGE IS  
OF POOR QUALITY**

3 **FOLDOUT FRAME**

Figure 50. MASR gimbal detail.  
(Only one axis shown. Orthogonal  
axis similar. Approximately  
2/3 scale.)

Both dry and wet lubricants were considered for lubrication of the ball bearings in the mechanism. The dry lube was selected because of the lower mechanism complexity, lower cost, higher operating temperature range and constant friction vs temperature. The balls, races and retainers will be RF sputtered with a 600 Å thick coating of MoS<sub>2</sub>. The retainer will be fabricated from a lead-tin-bronze compound to eliminate all sacrificial material. The Hughes RF sputtering process for deposition of MoS<sub>2</sub> lubricating films onto bearings has been found superior to other available methods of MoS<sub>2</sub> coating application. DC sputtering does not provide as uniform a coating and the MoS<sub>2</sub> adherence is weaker due to the lower arrival energy. Other methods fail to control film thickness and/or adhesion, resulting in incomplete coating coverage and poor film quality repeatability. Bonded coatings generally are too thick for use in ball bearings, or fail at the bond line long before film wearout. The various burnished film processes are difficult to reproduce exactly and seldom cover more than half the substrate area. This lack of coverage exposes high surface energy material, resulting in excessive lubricant transfer from the bearing retainer. The micro-sized glass bead impingement process for MoS<sub>2</sub> deposition provides better coverage than hand burnishing, but film thickness of MoS<sub>2</sub> is difficult to control and bearing surfaces are roughened by the glass beads. The Hughes RF sputtering process has been applied to more than 300 space quality bearings in the last two years.

#### 2.7.3.4 Gimbal Structure Material

After the basic configuration for the gimbal had been established and the rotating components selected, the next significant tradeoff was the material selection for the main housings, shafts and yokes. The primary factors considered in this tradeoff were thermal parameters, gimbal stiffness, weight, reliability and cost. The materials evaluated were aluminum, magnesium, titanium and beryllium.

The thermal properties of the four candidate materials were given prime attention in the trade study. The areas where the thermal characteristics cause concern are with respect to the accuracy requirements and the bearing installation. Accuracy is, of course, degraded by thermal distortion

of the shaft/housing while bearing performance is directly affected by thermal gradients and by differences in thermal expansion coefficients of bearing and housing/shaft materials. Titanium, even though it matches the steel bearing coefficient of expansion, could cause severe problems because of its poor thermal conductivity. Aluminum, on the other hand, has good conductivity, but like magnesium, has a very high coefficient of expansion. Beryllium was selected, despite its higher initial cost, because of its good thermal conductivity, compatibility of its coefficient of expansion with respect to the steel bearings, low weight, and high modulus of elasticity.

#### 2.7.4 Gimbal Performance

The performance of the gimbal, as proposed, is summarized in Table XXIII. The allotted time for antenna slew reversal or line stepping was between one and ten seconds. A time of two seconds was used to determine the required accelerations as shown in Figure 50. The torque required from the DC torquer is:

$$T_D = I_A \alpha \quad \text{where } I_A = \text{antenna inertia}$$

$$\alpha = \text{gimbal acceleration}$$

The maximum torque requirements occur when stepping between scan lines.

$$T_D = 90 \times 454 \times 10^{-6} \quad I_A = 90 \text{ slug-ft}^2 \text{ (pitch axis)}$$

$$T_D = 0.041 \text{ ft-lbs} \quad \alpha = 454 \mu\text{r/sec}^2$$

$$\approx 8 \text{ in-oz}$$

The stepping torque of 8 in-oz and the antenna reversal torque of 7 in-oz would be the momentum compensation required to be implemented by torquing the ACS momentum wheel. Table XXIII lists the additional torque budget for bearing friction and harness stiffness. Torque margins, using only one of the dual torquer windings, exceed 6:1 under worst case conditions.

The stiffness of the bearing/shaft/housing was measured on an almost identical gimbal assembly to be  $0.9 \times 10^6$  ft-lbs/rad. When this number is



TABLE XXIII. MASR GIMBAL PERFORMANCE

<u>Gimbal Range</u> (each axis)	±10 degrees
<u>Torque:</u>	
Peak torquer output (each axis)	120 in-oz
Time required for antenna reversals or stepping	2 seconds
Torque for antenna reversals	7 in-oz peak
Torque for antenna stepping	8 in-oz peak
Cross gimbal wiring (each axis)	5 in-oz
Bearing friction with 50 pounds preload (each axis)	8 in-oz
Torque margin slewing (each axis)	9:1 single winding 18:1 dual winding
Torque margin antenna reversals or stepping	6:1 single winding 12:1 dual winding
<u>Stiffness</u>	
Bearing/shaft/housing stiffness (each axis)	$0.9 \times 10^6$ ft-lb/rad
Natural gimbal frequency (each axis)	≥ 10 Hz
<u>Accuracy:</u>	
Frame to frame	±90 μrad (limited by A-D bit size resolution)

combined with the antenna inertia a natural frequency of 14 to 16 hertz results. The overall gimbal resonance, when the mounting yokes between gimbal axes and the load and tower interface are included, will decrease to between 10 and 12 hertz.

## 2.8 AREAS REQUIRING FURTHER STUDY

Several areas require further study either prior to, or concurrent with the MASR antenna development program. These areas are summarized in this section.

(i) Antenna Testing Methods. As outlined in Section 2.5 the testing of a large millimeter wave antenna poses some difficult problems. Direct measurements of patterns and gain require antenna ranges with long paths. Even if they were available, atmospheric effects such as attenuation and scintillation would make accurate measurements difficult. Other techniques such as near field techniques require large, precise, equipment and facilities. A more detailed study of testing techniques and the measurement accuracies attainable with each is necessary to estimate costs, schedules and achievable accuracies.

(ii) Feed studies. A second area in which additional preliminary study is desirable is the interaction of the quasi-optical feed technique with the Cassegrain reflector. Effects such as the consequences of the limitation of beam transverse dimensions and the departure from true Gaussian shape must be considered, since these effects have an impact on forward spillover loss and ultimately on the calibration temperature of the antenna.

(iii) Reflectivity Measurements. A third area in which more data is required is that of the reflection coefficients of aluminum and dielectric coatings. Measurements of these quantities should be made over the frequency range of interest.

(iv) Material. GY-70/X-30 proves to be the best choice for the MASR antenna because of its high stiffness and its thermal stability over a wide range of temperature. Even so, the extreme temperature range expected for the MASR antenna ( $-300^{\circ}\text{F}$  to  $+100^{\circ}\text{F}$ ) makes it questionable whether even GY-70/X-30 will be thermally stable enough to satisfy surface accuracy (rms) requirements during space operation. Microcracking has been shown to occur at temperatures below  $-150^{\circ}\text{F}$  in the GY-70/X-30 laminate, which over repeated cycling drives the CTE of the laminate to a value of  $-0.5 \times 10^{-6}$  in/in $^{\circ}\text{F}$ , severely affecting the accuracy of the reflector surface. Interestingly enough other graphite-epoxy combinations (i. e., HMS/934, T-300/934) which may be unacceptable because of initially high CTE ( $+0.7 \times 10^{-6}$ ) could microcrack and have a tolerable CTE. The uncertainties about microcracking relative to the temperature at which microcracking will occur, effects of cycling, processing effects, and many others suggest further material testing.

Consideration should also be given to investigating laminates which seem to be less prone to microcracking and hybrid laminates that resist microcracking, or to optimization of a laminate (regardless of microcracking presence in the laminate). Appendix B provides backup data of GD/C's experience with microcracking.

Another materials related problem is moisture absorption. It is expected that surface accuracy (distortion) will be affected by the existence of moisture in the graphite/epoxy material. The effect moisture absorption has on accuracy is very difficult to assess:

- a. Parts of the reflector may have varying degrees of moisture present at launch and subsequently lose the moisture at varying rates. Temperature gradients across the reflector can affect the desorption rate.
- b. The basic reflector skin and backup structure interface design may influence the effect moisture absorption/desorption has on surface distortion.
- c. Environmental control procedures that are reasonable to expect for the MASR antenna are not known at this time.
- d. The combination of microcracking and moisture absorption on the surface accuracy can produce opposite or balancing effects.

It is recommended that further moisture testing on graphite/epoxy laminate be pursued.

To evaluate the results of these material development programs (relative to microcracking and moisture absorption) it is Convair's recommendation that a new 8-foot Technology Antenna be designed, fabricated and tested. The intent being to utilize state-of-the-art technology and new materials technology to demonstrate the feasibility of a scaled down 4.4 meter MASR antenna reflector. Accuracies for the scaled down reflector would necessarily be more stringent.

(v) Profilometer. GD/C profilometer (a facility) will have to be modified to accommodate this large structure. Normal procedures would require that agreement to spend the money to modify the facility be requested from GD corporate headquarters. This request is not being made at this time.

**PRECEDING PAGE BLANK NOT FILMED**

### 3.0 SCHEDULE

An estimated schedule for the design, development and testing of the MASR antenna is presented in Figure 51.



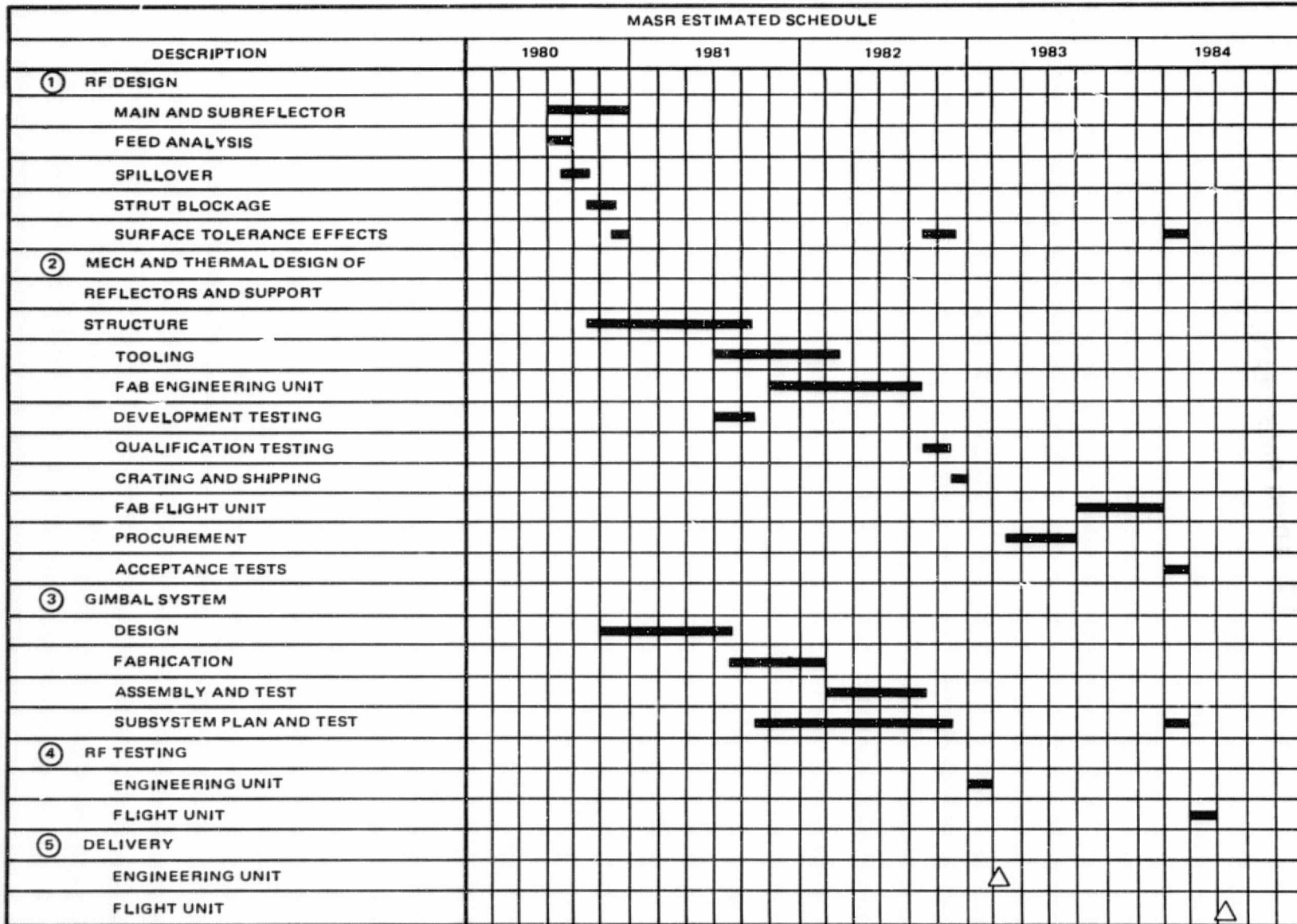


Figure 51. MASR estimated schedule.

#### 4.0 SUMMARY AND CONCLUSIONS

Two candidate antenna configurations were compared on the basis of anticipated performance, manufacturability, cost effectiveness and technical risk. The candidates were the paraboloidal reflector with an offset focal point feed, and the symmetrical Cassegrain antenna. While both candidates appear acceptable from an rf point of view (exclusive of tolerance effects), the symmetrical Cassegrain configuration was superior to the offset in all other respects. It is doubtful that the offset configuration could be constructed to the required surface tolerances even if manufacturing facilities were available. Consequently, the Cassegrain antenna was selected as the preferred configuration and additional studies of it were made. These studies indicate that it is feasible to build such an antenna and costs and schedules have been estimated. Several areas have also been identified as areas that require additional study prior to starting the construction of the antenna. These areas include rf testing of electrically large antennas, detailed study of quasi-optical feeds, reflectivity measurements of materials in the frequency range from 104 to 183 GHz, and further materials studies. It is also recommended that a new 8-foot antenna be designed, fabricated and tested as a scaled-down version of the 4.4 meter antenna.

PRECEDING PAGE BLANK NOT FILMED

## APPENDIX A. EFFECT OF BLOCKAGE AND SHADOWING

The effect of blockage and shadowing on the field strength at the peak of the beam may be computed by referring to Figure 13 on page 37. The blockage caused by the struts effectively removes the projected area of the struts from the aperture. For tapered struts, the strut width,  $w(\rho)$ , is a linear function of distance from the reflector axis, varying from a value  $w_s$  at the edge of the subreflector, to  $w_0$  at the main reflector. The shadowing caused by the struts effectively removes the projected area of the shadow from the aperture.

At the junction of the strut and the main reflector the shadow subtends an angle  $2\beta$  approximately equal to  $w_0/\rho_0$ , while at the edge of the main reflector, the shadow subtends an angle of approximately  $2w_1/D$ , where  $w_1$  is the width of the shadow at the reflector edge. It is determined by the position at which the struts join the main reflector, the  $F/D$  ratio of the main reflector, the diameter and eccentricity of the subreflector and on the strut diameter.

In order to evaluate the shadow width as a function of  $\rho$ , consider Figure A-1. Figure A-1a is an edge view of the main reflector, the subreflector, and a tapered strut. Figure A-1b is a view looking in along the axis of the reflectors. The radius,  $r_{st}$ , of the strut varies linearly along its length and may be described by the following expression

$$r_{st} = r_{sts} + \frac{(r_{sto} - r_{sts})}{(z_s - z_0)} (z_s - z) \quad (A-1)$$

where

- $r_{sts}$  = strut radius at the subreflector
- $r_{sto}$  = strut radius at the main reflector
- $z_s$  = axial position of subreflector edge
- $z_o$  = axial position of strut - main reflector junction

Let  $\rho_{st}$  be the radial distance from the  $z$  axis to the center line of the strut,  $\rho_s$  the radius of the subreflector, and  $\rho_o$  the radius from the  $z$ -axis to the junction of the strut centerline and the main reflector. Then in terms of the symbols of Figure A-1 the equation expressing  $\rho_{st}$  as a function of axial position,  $z$ , may be written as follows:

$$\rho_{st} = \frac{\rho_{st} + \delta - \rho_o}{z_s - z_o} (z - z_o) + \rho_o \quad (A-2)$$

where

$$\delta = r_{sts} / \cos \eta \quad (A-3)$$

$$\cos \eta = \frac{r_{st} (\rho_o - \rho_s) + (z_s - z_o) \sqrt{(\rho_o - \rho_s)^2 + (z_s - z_o)^2 - r_{st}^2}}{(\rho_o - \rho_s)^2 + (z_s - z_o)^2} \quad (A-4)$$

The shadow is determined by locating the intersections of the strut and the rays from the focus to the main reflector. These points of intersection are approximated by the points of intersection of the rays and the center line of the strut. For a typical ray the strut and its shadow will subtend an angle,  $2\beta$ , about the  $z$ -axis given approximately by  $2 r_{st} / \rho_{st}$ . Then the width

of the shadow of that ray on the main reflector will be given approximately by the following expression

$$w_{sh} \approx 2 r_{st} \frac{\rho_r}{\rho_{st}} = 2 \beta \rho_r \quad (A-5)$$

where  $\rho_r$  is the radius from the z-axis at which the ray would have intersected the main reflector, and  $\beta$  is the half angle subtended by the corresponding portion of the shadow. The equation of the ray at an angle  $\psi$  to the negative z-axis is given as follows.

$$\rho_{ray} = (F - z) \tan \psi \quad (A-6)$$

The ray intersects the strut center line at  $\rho_{ray} = \rho_{st}$ . Thus, from equations A-2 and A-6 the following equation results.

$$\frac{\rho_s + \delta - \rho_o}{(z_s - z_o)} (z - z_o) + \rho_o = (F - z) \tan \psi \quad (A-7)$$

This has a solution,  $z_1$ , given by the following expression

$$z_1 = \frac{F \tan \psi - \rho_o + z_o \left( \frac{\rho_s + \delta - \rho_o}{z_s - z_o} \right)}{\tan \psi + \left( \frac{\rho_s + \delta - \rho_o}{z_s - z_o} \right)} \quad (A-8)$$

The corresponding radius to the point of intersection is then given as follows.

$$\rho_{st} = \frac{\left( \frac{\rho_s + \delta - \rho_o}{z_s - z_o} \right) (F - z_o) \tan \psi + \rho_o \tan \psi}{\left( \frac{\rho_s + \delta - \rho_o}{z_s - z_o} \right) + \tan \psi} \quad (A-9)$$

The ray intercepts the main reflector when  $\rho_{ray}$  is equal to  $\rho_r$ , the radius to the main reflector. But  $\rho_r$  is given as follows

$$\rho_r = 2\sqrt{Fz} \quad (A-10)$$

The intercept is then the solution of the following equation

$$2\sqrt{Fz} = (F - z) \tan \psi \quad (A-11)$$

The solution is

$$z = F \tan^2 \frac{\psi}{2} \quad (A-12)$$

so that  $\rho_r$  is given as follows

$$\rho_r = 2F \tan \frac{\psi}{2} \quad (A-13)$$

But

$$\tan \psi = \frac{2 \tan \frac{\psi}{2}}{1 - \tan^2 \frac{\psi}{2}} = \frac{\frac{\rho_r}{F}}{1 - \frac{\rho_r^2}{4F^2}} \quad (A-14)$$

Therefore the following set of expressions is obtained:

$$\rho_{st} = \frac{\left[ \left( \frac{\rho_s + \delta - \rho_o}{z_s - z_o} \right) (F - z_o) + \rho_o \right] \frac{\rho_r / F}{1 - (\rho_r / 2F)^2}}{\left[ \frac{\rho_r / F}{1 - (\rho_r / 2F)^2} + \frac{\rho_s + \delta - \rho_o}{z_s - z_o} \right]} \quad (A-15)$$

$$z_{st} = z_o + \frac{(\rho_{st} - \rho_o)(z_s - z_o)}{\rho_s + \delta - \rho_o} \quad (\text{A-16})$$

where

$$z_o = \frac{\rho_o^2}{4F} \quad (\text{A-17})$$

and

$$z_s = \sqrt{\frac{\rho_s^2}{(e^2 - 1)} + \left(\frac{F - z_h}{2e}\right)^2} + \frac{F + z_h}{2} \quad (\text{A-18})$$

in which  $e$  is the eccentricity of the subreflector and  $\delta$  is given by Equations A-3 and A-4.

The angle  $\beta$ , that the shadow subtends at the reflector axis varies nearly linearly from a value  $w_o/2\rho_o$  at the junction of the strut and the reflector to a value  $w_1/D$  at the reflector edge, where  $w_o$  is twice the strut radius,  $r_{sto}$ . Thus  $\beta$  may be approximated by Eq. 18 in the report.

The far-field on axis relative to the far-field that would exist without shadowing or blockage is denoted by  $R$ , and is obtained by integrating the field over the aperture, omitting the blocked and shadowed regions and dividing by the integral of the field over the unblocked, unshadowed aperture. If the aperture field is assumed to be Gaussian, as given by Equation 19 of the report,  $R$  is given by the following expression.

$$\begin{aligned}
R = 1 - E_o \left\{ \int_0^{2\pi} \int_0^{d_s/2} e^{-\alpha^2 \rho^2} \rho d\rho d\phi + n \int_{-d_s/2}^{p_o} \left[ w_s - \frac{(w_o - w_s) d_s}{\left(\rho_o - \frac{d_s}{2}\right)^2} \right] e^{-\alpha^2 \rho^2} d\rho \right. \\
\left. + n \int_{-d_s/2}^{p_o} \frac{(w_o - w_s)}{\left(\rho_o - \frac{d_s}{2}\right)} \rho e^{-\alpha^2 \rho^2} d\rho + 2n \int_{p_o}^{D/2} \int_0^{\beta(\rho)} e^{-\alpha^2 \rho^2} \rho d\rho d\phi \right\} \\
/ E_o \int_0^{2\pi} \int_0^{D/2} e^{-\alpha^2 \rho^2} \rho d\rho d\phi \quad (A-19)
\end{aligned}$$

where  $n$  is the number of struts and the aperture amplitude distribution is given by  $E_o e^{-\alpha^2 \rho^2}$ . The expression may be evaluated to give the following result.



$$\begin{aligned}
R &= 1 - \frac{\left(1 - e^{-\alpha^2 \frac{d_s^2}{4}}\right)}{\left(1 - e^{-\alpha^2 \frac{D^2}{4}}\right)} - \frac{n\alpha \left[ w_s - \frac{(w_o - w_s) \frac{d_s}{2}}{\left(\rho_o - \frac{d_s}{2}\right)} \right]}{2\sqrt{\pi}} \frac{\left[ \operatorname{erf}(\alpha \rho_o) - \operatorname{erf}\left(\alpha \frac{d_s}{2}\right) \right]}{\left(1 - e^{-\alpha^2 \frac{D^2}{4}}\right)} \\
&- \frac{n(w_o - w_s)}{2\pi \left(\rho_o - \frac{d_s}{2}\right)} \frac{\left[ e^{-\alpha^2 \frac{d_s^2}{4}} - e^{-\alpha^2 \rho_o^2} \right]}{\left(1 - e^{-\alpha^2 \frac{D^2}{4}}\right)} \\
&- n \left[ \beta_o - \left(\frac{\beta_1 - \beta_o}{\frac{D}{2} - \rho_o}\right) \rho_o \right] \frac{\left[ e^{-\alpha^2 \rho_o^2} - e^{-\alpha^2 \frac{D^2}{4}} \right]}{\pi \left[ 1 - e^{-\alpha^2 \frac{D^2}{4}} \right]} \\
&- n \left(\frac{\beta_1 - \beta_o}{\frac{D}{2} - \rho_o}\right) \frac{\left[ \rho_o e^{-\alpha^2 \rho_o^2} - \frac{D}{2} e^{-\alpha^2 \frac{D^2}{4}} \right]}{\pi \left[ 1 - e^{-\alpha^2 \frac{D^2}{4}} \right]} \\
&- n \left(\frac{\beta_1 - \beta_o}{\frac{D}{2} - \rho_o}\right) \frac{\left[ \operatorname{erf}\left(\alpha \frac{D}{2}\right) - \operatorname{erf}(\alpha \rho_o) \right]}{2\sqrt{\pi} \alpha \left[ 1 - e^{-\alpha^2 \frac{D^2}{4}} \right]}
\end{aligned}
\tag{A-20}$$

where

$$\operatorname{erf}(x) = \frac{2}{\sqrt{\pi}} \int_0^x e^{-t^2} dt \tag{A-21}$$

ORIGINAL PAGE IS  
 OF POOR QUALITY  
 PRECEDING PAGE BLANK NOT FILMED

APPENDIX B  
 MATERIAL SELECTION

The selection of the proper materials of construction for an antenna is dependent upon specified design criteria. For an orbital antenna this application, in general, requires a thermally stable structure of low weight and mass moment of inertia, coupled with high stiffness, strength and natural frequency. The interaction of these factors and their influence on the antenna system and spacecraft performance are shown in Figure B-1.

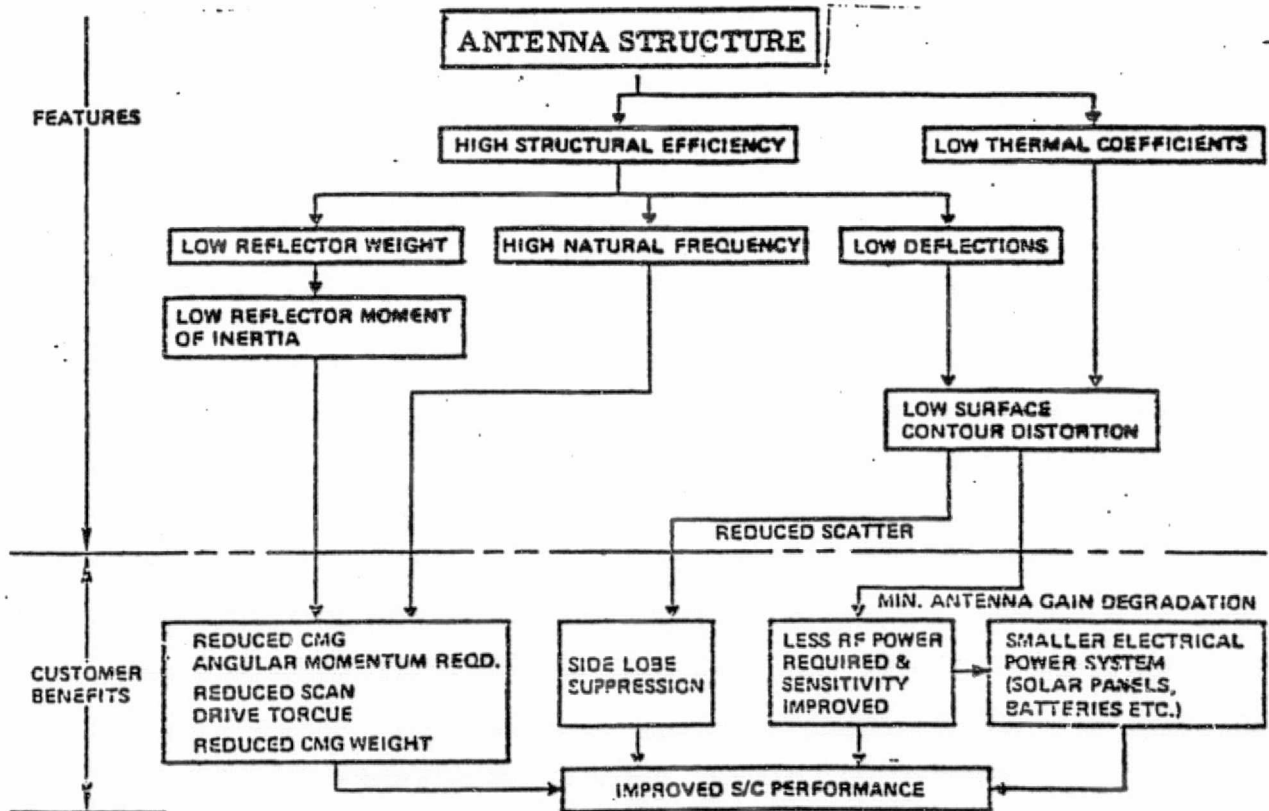


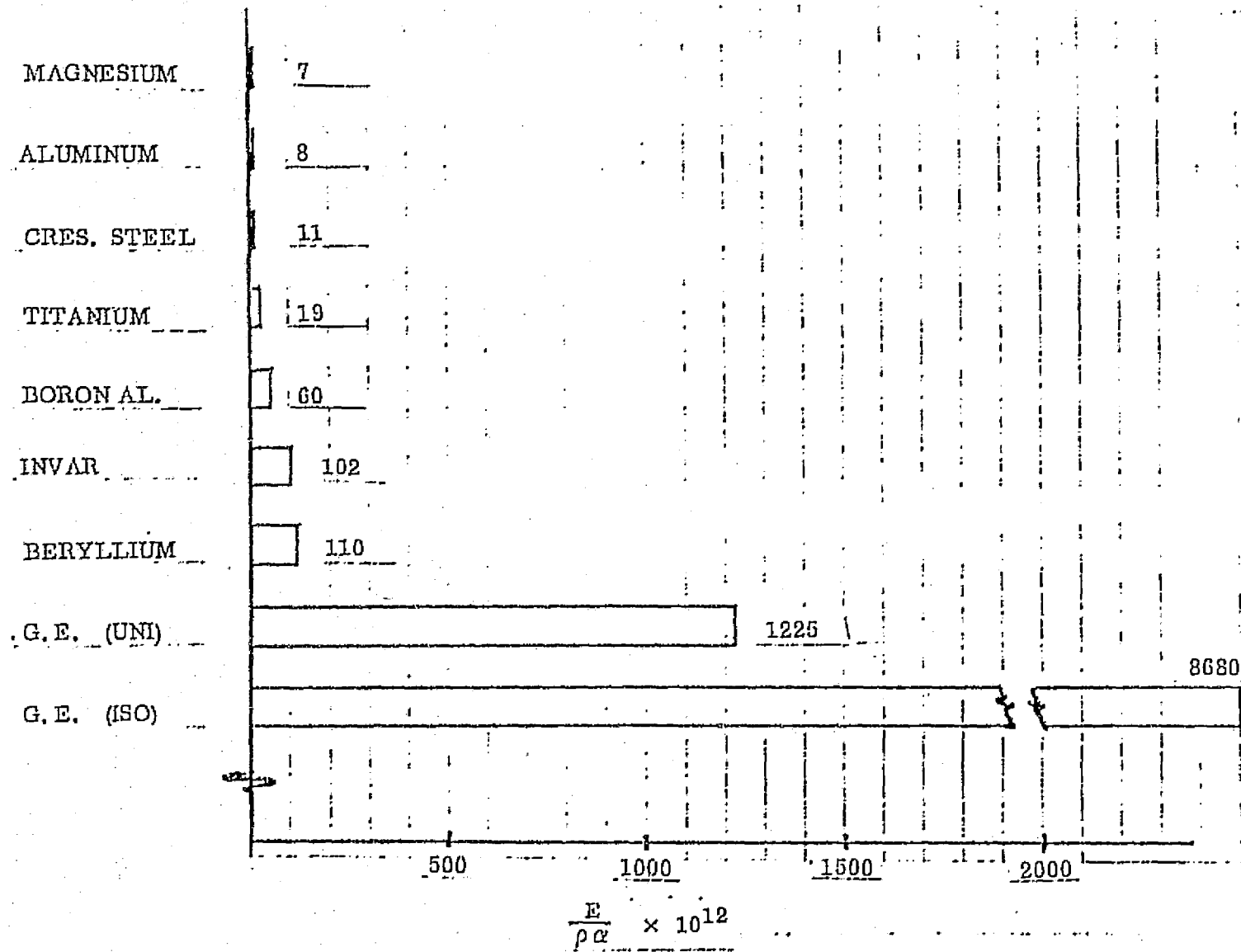
Figure B-1. Antenna design optimization.

Key factors in the selection of the antenna construction material are a low coefficient of expansion ( $\alpha$ ) and specific weight ( $\rho$ ), a high Youngs modulus (E) and ultimate tensile strength  $F_{tu}$ . These factors vary from material to material and typical values, of candidate materials, are presented in Table B-1. The structural efficiency of a material is commonly measured by means of a merit function number obtained by dividing the materials modulus by the product of its specific weight and expansion coefficient. Thus, a high merit function characterizes a material with high stiffness and low weight, which is thermally stable. The merit functions of various materials have been computed and are compared in Figure B-2. An examination of this chart will show that, for our application, graphite/epoxy is far superior to the other materials; by a factor of ten when in its unidirectional configuration and by a factor of eighty in its isotropic form.

The strength to weight ratio of the candidate materials has also been computed. This data is illustrated in Figure B-3 and unidirectional graphite/epoxy again is shown to be the better material. The strength to weight ratio of isotropic graphite/epoxy is about twice that of magnesium and about half that of aluminum. Typically, antenna structures are stiffness, not strength

TABLE B-1. MATERIAL COMPARISON

Material	$\rho \frac{\text{lbs}}{\text{in}^3}$	$E \frac{\text{lbs}}{\text{in}^2} \times 10^6$	$F_{tu} \frac{\text{lbs}}{\text{in}^2} \times 10^3$	$\alpha \frac{\text{in}}{\text{in}^\circ \text{F}} \times 10^{-6}$
G/E (UNI)	.064	40.0	80	-.51
G/E (ISO)	.064	15.0	28	-.03
Magnesium	.064	6.5	15	14.00
Beryllium	.066	43.5	69	6.00
Boron Al.	.096	18.0	76	3.20
Aluminum	.100	10.0	77	13.00
Titanium	.160	16.0	134	5.30
Cres. Steel	.286	29.0	30	8.80
Invar	.295	21.0	32	.70



ORIGINAL PAGE IS  
OF POOR QUALITY

Figure B-2. Merit function comparison.

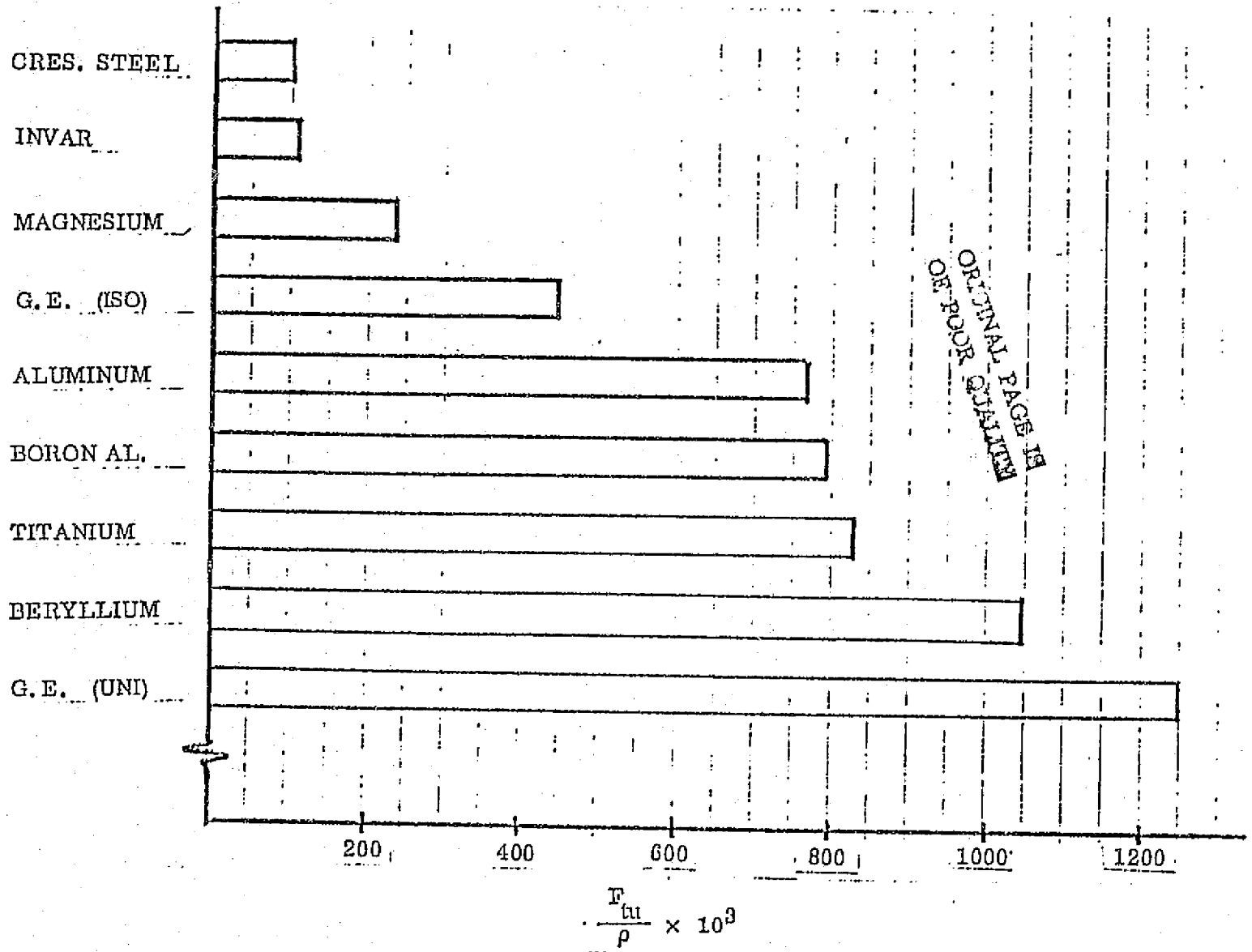


Figure B-3. Strength to weight comparison.

critical. In those areas where high loading is encountered, such as support points and subreflector struts, adequate strength may be achieved by adding unidirectional material as required.

The performance characteristics of the reflectors under consideration in this study are such that the use of graphite/epoxy composite materials is essential. The above merit function comparisons, shown in Figures B-2 and B-3, substantiate its selection over conventional aerospace materials.

From the available graphite/epoxy systems, Convair has selected Fiberite's GY-70/X-30 as the primary composite system for structural applications in this study. GY-70/X-30 provides extremely high stiffness properties and exhibits excellent thermal dimensional stability when arranged in a cross-plyed laminate. A merit function comparison of candidate fiber systems is shown in Figure B-4 that substantiates the selection of GY-70 over the other fiber materials. The following section discusses in detail the characteristics of GY-70/X-30 and provides supporting data to justify its selection.

#### GY-70/X-30 PHYSICAL, ENVIRONMENTAL AND MECHANICAL CHARACTERISTICS -

Convair has selected GY-70/X-30 graphite/epoxy composite as the basic material for the proposed antenna structure. The Celion GY-70 graphite fiber is a product of Celanese Corporation, and the X-30 resin is an epoxy formulation produced by Fiberite Corporation. The basic material is obtained as a prepreg from Fiberite per the requirements of Convair Specification SD 73-62050.

GY-70 graphite fibers are supplied by Celanese as a continuous collimated multifilament yarn having an average modulus of  $77 \pm 4$  msi and a minimum tensile strength of 220 ksi when tested in accordance with Celanese Specifications SUM-S-108G and SUM-S-130.

The X-30 resin as formulated by Fiberite can be cured over a temperature range of 250F to 350F. The cure cycle developed at Convair has a maximum cure temperature of 275F and optimizes the desired minimum outgassing, resistance to microcracking, precision yield characteristics, and other material parameters vital to space systems.

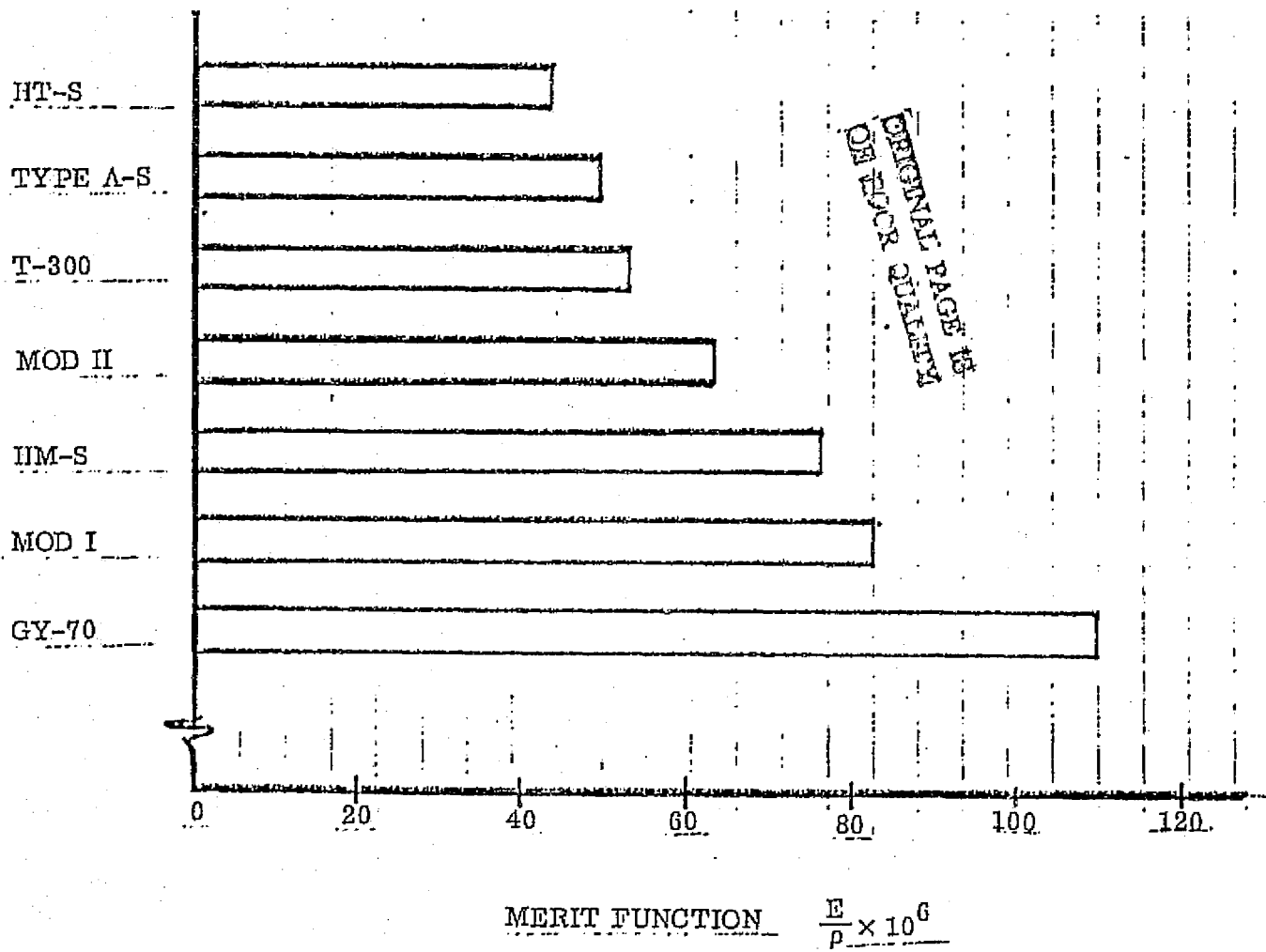


Figure B-4. Fiber system merit function.

The X-30 resin has been used by Convair extensively with GY-70, Modmor I, and HM-S graphite fiber reinforcements. Parts fabricated from these systems include large parabolic antennas, mirror support structures and a half-scale version of the large space telescope. The latter structure, known as the GEMS, has been extensively tested structurally and by thermal/vacuum exposure.

Over twenty batches of GY-70/X-30 prepreg have been received from Fiberite in the last year and have been utilized in support of hardware systems. Table B-2 summarizes Quality Control tests on production batches and includes prepreg data, basic fiber data, and composite test results. Twelve batches have been subjected to more extensive testing, including tensile strength and modulus testing of both unidirectional and ((0/45/90/135) composites as well as thermal expansion testing of the pseudoisotropic material. Table B-3 summarizes the tensile data.

Additional mechanical and physical properties of GY-70/X-30 are summarized in Table B-4. Thermal coefficient of expansion ( $\alpha$ ) data for unidirectional GY-70/X-30 in both the 0- and 90-degree directions as a function of test temperature are plotted in Figures B-5 and B-6. Figure B-7 shows the  $\alpha$  data as a function of temperature for ((0/45/90/135)<sub>s</sub>)<sub>2</sub> pseudoisotropic laminates. The data represents seven batches of prepreg. Thermal conductivity as a function of temperature for GY-70 reinforced epoxy is plotted in Figures B-8 and B-9. Thermo-optical data for GY-70 reinforced epoxy is shown in Figure B-10.

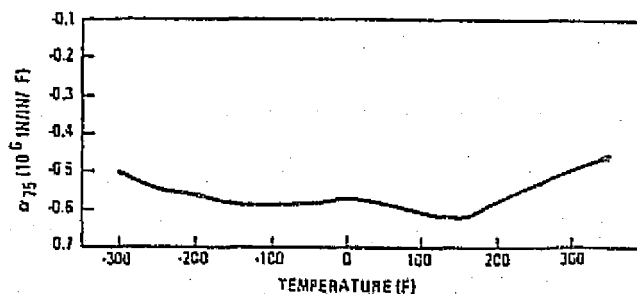


Figure B-5. Design coefficient of thermal expansion as a function of temperature for GY-70/X-30, unidirectional laminate tested at 0 degree.



TABLE B-2. QUALITY CONTROL TESTS ON PRODUCTION BATCHES OF GY-70/X-30

Prepreg Properties						Fiber Properties			Composite Properties	
Lot No.	Resin Solids (%)	Volatiles (%)	Flow % at 100	Tack	Drape	Tensile Strength (ksi)	Tensile Modulus (msi)	Density gm/cc	Horizontal Beam Shear (ksi)	Flexure Strength (ksi)
4A-15	41.8	4.6	26.4	Pass	Pass	228/227	73/76	1.92		138.3
4A-37	41.0	5.0	26.9	Pass	Pass	228/227	73/76	1.92	9.9	137.5
4A-40	39.5	5.0	24.4	Pass	Pass	230/244/239	76/74/73	1.94	9.0	121.4
4A-61	40.2	4.0	22.9	Pass	Pass	229/246/223	74/79/77	1.94	8.9	132.4
4A-56	44.0	4.3	28.3	Pass	Pass	230/244/236	74/73/76	1.94	8.7	143.5
4A-64	40.9	4.9	25.8	Pass	Pass	228	77	1.94	10.0	146.4
4A-65	42.1	4.7	25.5	Pass	Pass	234/229	73/74	1.94	9.6	112.0
4A-68	41.6	4.9	25.2	Pass	Pass	234/228	73/77	1.94	9.9	146.6
4A-71	40.7	5.0	22.4	Pass	Pass	236/236/228	74/76/77	1.94	9.7	114.0
4A-75	41.9	4.7	24.2	Pass	Pass	236/278/228	74/77/77	1.94	9.1	144.9
4A-82	40.7	4.8	24.1	Pass	Pass	247/230/236/ 234/278	76/77/78/ 77/77	1.94	8.6	112.9
4A-83	42.0	5.0	24.9	Pass	Pass	247/230/228	76/77/79	1.94	9.5	122.4
4A-86	39.5	4.8	23.6	Pass	Pass	247/230/266/ 249/262	76/77/78.2/ 76.9/76.1	1.94	9.9	117.0
4A-87	41.8	4.9	22.4	Pass	Pass	262/246/258	79/76.1/78.7	1.94	10.6	114.5
4A-90	44.4	5.0	25.9	Pass	Pass	257/279/254	75/76/79	1.93/ 1.96/ 1.94	10.7	151.7
4A-99	39.1	4.7	25.2	Pass	Pass	249/246/261/ 254/256	81/78.7/79/ 79/76	1.93/ 1.94	9.5	130.2
4B-98A	43.1	2.7	23.2	Pass	Pass	278/278/264	76/76/76	1.94 1.94		
4B-93B	43.2	3.6	25.0	Pass	Pass	254/260/278/ 264	77/76/76/76	1.96/ 1.95/ 1.94		
4B-98C	45.0	1.4	24.8	Pass	Pass	254/260/278/ 264	77/76/76/76	1.96/ 1.95/ 1.94		
4B-98D	42.3	1.7	23.0	Pass	Pass	243/262/269/ 254/260/264/ 264		1.92/ 1.94/ 1.96		

ORIGINAL PAGE IS OF POOR QUALITY

TABLE B-3. QUALITY CONTROL TENSILE DATA

Laminate	No. of Lots	Total No. of Specimens	$\bar{X}$	S
{0} <sub>T</sub> Laminate Tested at 0 Deg				
RT Tensile Strength (ksi)	11	33	110.5	21.0
RT Tensile Modulus (msi)	11	33	47.1	1.81
{0/45/90/135} <sub>2</sub> Laminate tested at 0 Deg				
RT Tensile Strength (ksi)	12	24	37.66	6.46
RT Tensile Modulus (msi)	12	24	15.38	1.15

TABLE B-4. MECHANICAL AND PHYSICAL PROPERTIES OF GY-70/X-30

Unidirectional Laminate	
RT transverse tensile strength (ksi)	3.76
RT transverse tensile modulus (msi)	0.93
RT shear modulus (msi)	0.59
RT in-plane shear strength (ksi)	3.90
RT Poisson's ratio	0.26
{0/45/90/135} <sub>2</sub> Laminate	
RT 0 deg compression strength (ksi)	19.8
RT 0 deg compression modulus (msi)	14.98
RT in-plane shear strength (ksi)	15.0
RT shear modulus (msi)	5.67
RT Poisson's ratio	0.319
Density (lb/cu in.)	0.0635

ORIGINAL PAGE IS  
OF POOR QUALITY

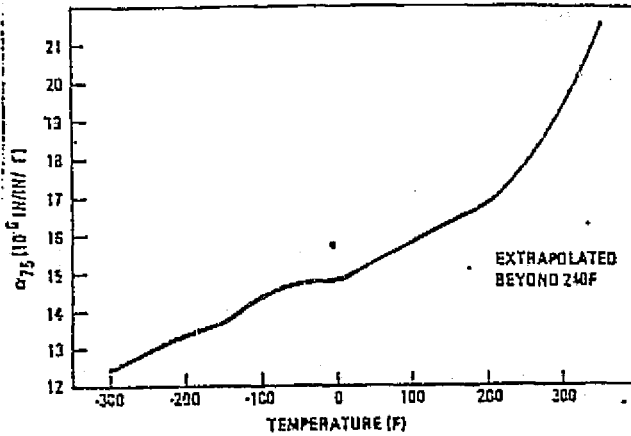


Figure B-6. Design coefficient of thermal expansion as a function of temperature for GY-70/X-30, uni-directional laminate tested at 90 degrees.

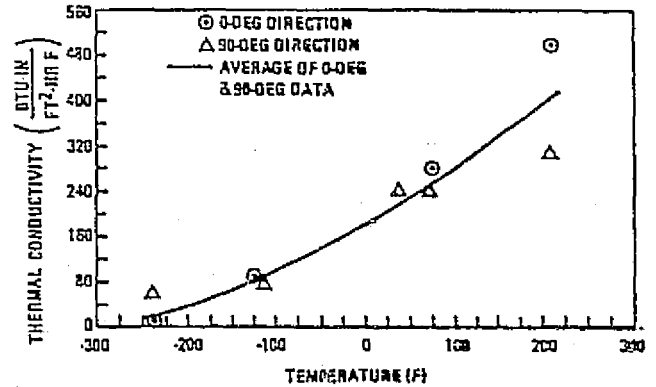


Figure B-8. Thermal conductivity as a function of temperature for  $(0/\pm 30/\pm 60/90)_s$  GY-70/X-30 epoxy tested in 0- and 90-degree directions.

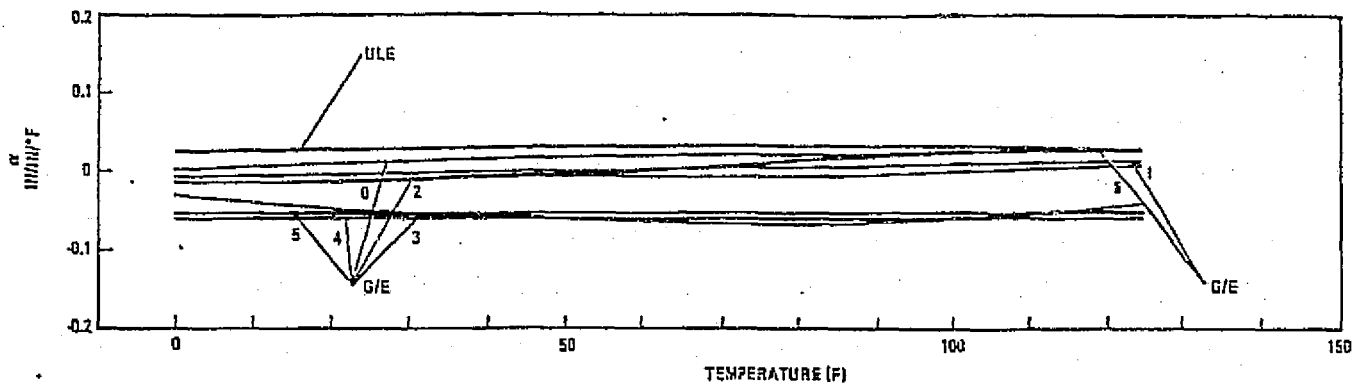


Figure B-7. Coefficient of thermal expansion  $((0/45/90/135)_s)_2$  GY-70/X-30 as a function of temperature (seven production batches).

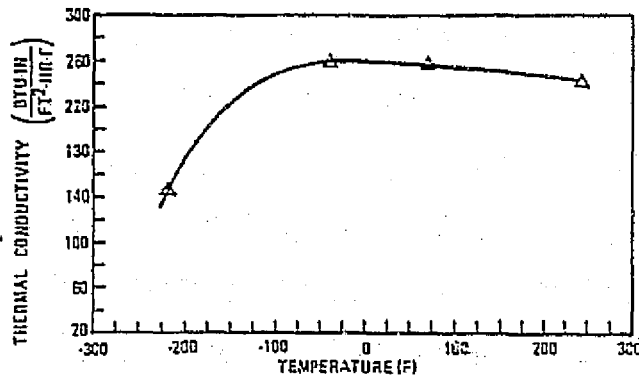


Figure B-9. Thermal conductivity as a function of temperature for  $((0/\pm 60)_s)_2$  GY-70 epoxy tested in 0-degree direction.

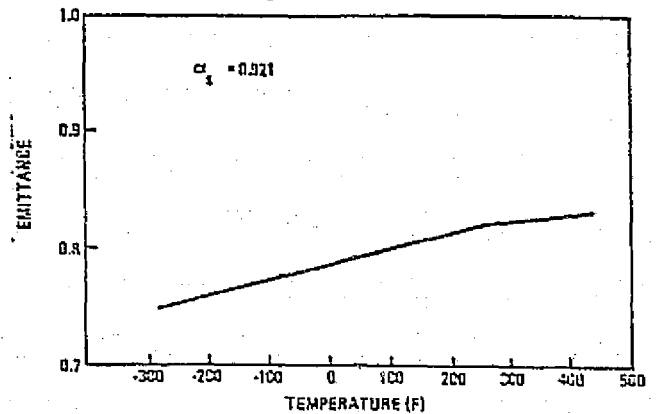


Figure B-10. Thermo-optical data for GY-70/epoxy.

For the thermal environment predicted for MASR antenna of  $-300^{\circ}\text{F}$  to  $+100^{\circ}\text{F}$  a phenomenon called microcracking may occur which will change the thermal distortion characteristic of the material and subsequently the antenna.

Microcracking, sometimes known as translaminar stress relief cracking, occurs with many graphite/epoxy composites. The primary cause is the difference in the elastic and thermal properties of the graphite reinforcement and the epoxy resin matrix. Specifically, one of the primary factors is the mismatch in thermal expansion of adjacent layers in a crossply laminate where the transverse coefficient of expansion of a unidirectional ply is highly positive (approximately  $16 \times 10^{-6}$  in./in./ $^{\circ}\text{F}$ ) and that of an adjacent crossply close to zero. In many cases, microcracking can be analytically predicted.

Composites containing higher modulus fibers are more likely to encounter microcracking because of more negative thermal expansion coefficients and because they are generally more difficult to wet, resulting in poor adhesion at the fiber-to-resin interface and therefore lower shear strengths. Therefore, one would expect GY-70 laminates to be more prone to cracking than H.M-S, Modmor I, and VSA-11 laminates which in turn would be more likely to crack than A-S, T-300, and Celion 6000 laminates. Layup orientations also affect the occurrence of microcracking. Generally, in crossplied layups it is desirable to minimize large number of plies in one direction sandwiched between angle plies. A number of other factors influencing the amount of microcracking encountered in graphite reinforced resin matrix composites which minimize microcracking include:

- Minimum resin shrinkage after gellation.
- Resins having high strength and high strain.
- Low cure temperature to minimize thermal stresses.
- Resins having low coefficients of expansion.
- Composites having high shear strengths.
- Fibers with uniform bean-shaped or circular cross-sections rather than irregular cross-sectional fibers.
- Yarns or tows with minimal fiber twist and good collimation.

From the above, it is obvious that the selection of resin is of extreme importance. It is desirable to have a tough resin with a high modulus, high strain capacity, which cures at a relatively low temperature, and has a low thermal coefficient of expansion. For satellite applications, low temperature cure must be tempered by how it affects the resulting high-temperature resistance and outgassing characteristics of the resulting composites.

It has also been found that high void content laminates suffer more microcracks than low void content laminates. Thicker laminates are more prone to thermal shock on rapid cooling to  $-300^{\circ}\text{F}$ , and therefore microcracking is more likely to occur in thick laminates.

Microcracking is not a concern from a structural standpoint, at least with respect to low-cycle fatigue criteria. Testing of microcracked laminates by General Dynamics under Air Force Contract F33615-70-C-1442 showed no adverse effects as a result of low-cycle fatigue.

With the goal of zero CTE in mind, the graphite/epoxy system of GY-70/X-30 was selected as the system most likely to achieve the zero CTE, high stiffness, and low weight with a minimum of microcracking. The room temperature CTE for pseudoisotropic GY-70/X-30 approaches  $0 \pm 0.5 \mu\text{in. / in. /}^{\circ}\text{F}$  whereas other graphite/epoxy systems like T300/934 are around  $+0.70 \mu\text{in. / in. /}^{\circ}\text{F}$  with a much lower stiffness. Further, General Dynamics has shown that GY-70/X-90 4 pseudoisotropic laminates almost always crack in cool-down to room temperature after curing at  $375^{\circ}\text{F}$ . Cracks generally parallel the fibers in each lamina. In some cases where the panels at room temperature have not microcracked, subsequent cooling to  $-320^{\circ}\text{F}$  causes cracking. By going to the Fiberite X-30 resin that can be cured at 250 to  $275^{\circ}\text{F}$ , isotropic GY-70 laminates have been prepared which survive cycling to  $-320^{\circ}\text{F}$  without cracking. Using the most sensitive thermal expansion measuring equipment available (laser precision dilatometer), the temperature at which microcracking occurs can be accurately pinpointed. The highest temperature at which any microcracking has been detected with GY-70/X-30 composites is  $-150^{\circ}\text{F}$ .

When microcracking occurs there is a lowering in the thermal coefficient of expansion ( $\alpha$ ). This change in  $\alpha$  due to microcracking may be the result of deterioration of the highly positive  $\alpha$  of the resin matrix while the negative  $\alpha$  fibers are still intact. General Dynamics believes that the lowering of  $\alpha$  as a result of microcracking is due to decoupling of the plies so that the only plies influencing the measurement are those where the fibers are parallel to the measurement direction. For (0/45/90/135)<sub>ns</sub> GY-70/epoxy laminates which normally have a  $0 \pm 0.05 \mu\text{in. /in. /}^\circ\text{F}$  thermal coefficient of expansion, the  $\alpha$  after microcracking approaches  $-0.5 \mu\text{in. /in. /}^\circ\text{F}$  which is the coefficient of expansion for unidirectional GY-70/epoxy. For these reasons GY-70/X-30 is the logical material choice for this application. GY-70/X-30 exhibits the high stiffness, low density, and the greatest potential to achieve the near zero coefficients of thermal expansion in light of the microcracking problem of the graphite/epoxy material available. If the microcracking problem cannot be successfully solved, an alternate material concept can be tried. Since the microcracking causes a deterioration of the highly positive  $\alpha$  of the resin or causes decoupling of the plies, it is theoretically possible to maintain the positive  $\alpha$  in the laminate with the addition of glass fibers. This can be accomplished with either adding glass plies directly or using a new prepreg configuration which weaves a cloth. The weave can be made to almost any combination of glass and graphites to meet specified properties. Again an extensive test program would be necessary to prove this concept and determine the correct makeup of laminas.